Andrin Stump

Polymer Based Technology Development for Integrated Optics

From the waveguide design to the fiber-pigtailed chip

Polymer Based Technology Development for Integrated Optics

From the waveguide design to the fiber-pigtailed chip

Thèse présentée à la faculté des sciences
Institut de microtechnique
Université de Neuchâtel

Pour l'obtention du grade de docteur ès sciences

par

Andrin Stump

Acceptée sur proposition du jury :
MM. H.-P. Herzig (directeur de thèse)
R. Dändliker
Christian Bosshard (CSEM-Alpnach)
G. Guekos (ETH Zürich)
et Daniel Erni (ETH Zürich)

Soutenue le 21 Juin 2005

Université de Neuchâtel
2005

Université de Neuchâtel unine

IMPRIMATUR POUR LA THESE

Polymer based technology for integrated optics: from the fiber-pigtailed chip

Andrin STUMP

UNIVERSITE DE NEUCHATEL

FACULTE DES SCIENCES

La Faculté des sciences de l'Université de Neuchâtel,
sur le rapport des membres du jury

MM. H.-P. Herzig (directeur de thèse),
R. Dändliker, C. Bosshard (CSEM-Alpnach),
G. Guekos (ETH Zürich)
et D. Erni (ETH Zürich)

autorise l'impression de la présente thèse.

Neuchâtel, le 18 octobre 2005

Le doyen :

J.-P. Derendinger

Faculté des Sciences
■ Rue Emile-Argand 11 ■ CP 2 ■ CH-2007 Neuchâtel
■ Téléphone : +41 32 718 21 00 ■ Fax : +41 32 718 21 03 ■ E-mail : secretariat.sciences@unine.ch ■ www.unine.ch

Table of content

Abstract 11

1. Introduction 13
1.1. Aim of this work 13
1.2. State of the art in integrated optics for telecom applications 13
1.3. Integrated optics with polymer materials 16
1.4. Fiber-pigtailing of optical chips 19
1.5. What is new in this work 20

2. Optical waveguide theory 23
2.1. Waveguide modes 24
2.1.1. Wave equation 24
2.1.2. Characteristic equation for slab waveguides 26
2.2. Optical loss 28
2.2.1. Absorption loss 28
2.2.2. Scattering loss 29
2.2.3. Bending loss 29
2.3. Mode coupling 31
2.3.1. Coupling efficiency at waveguide transitions and interfaces 32
2.3.2. Directional coupling between waveguides 35
2.3.3. Asymmetric coupling 37

3. Simulation of optical waveguide structures 39
3.1. The beam propagation method (BPM) 39
3.1.1. Wide-angle BPM 40
3.1.2. Finite difference formulation 41
3.2. The finite difference time domain (FDTD) method 43
3.3. The finite element method (FEM) 43
3.4. Comparison of simulation methods 45

4. Polymer optical waveguides 47
4.1. Polymer materials for integrated optics 47
4.2. Thermo-optic effect in polymers 50
4.3. Material characterization 50
4.3.1. Refractive index measurement 52
4.3.2. Measurement of thermal conductivity 57

4.4. Waveguide design 63
4.5. Waveguide fabrication 64
4.5.1. Reactive ion etching 65
4.5.2. Direct UV printing 66
4.5.3. Cleaving of waveguide chips 70
4.6. Optical characterization of polymer waveguides 71
4.6.1. Waveguide mode 71
4.6.2. Propagation loss 71
4.6.3. Bend loss 73

5. Integrated optical devices based on polymer waveguides 75
5.1. Passive devices 75
5.1.1. Power splitters / combiners 75
5.1.2. Multimode interferometers 78
5.1.3. Conclusion on passive devices 80
5.2. Thermo-optic devices: switch 81
5.2.1. Digital and interferometric switches 81
5.2.2. Thermo-optic simulations 83
5.2.3. Design of wide-angle digital optical switch 83
5.2.4. Fabrication of electrodes 87
5.2.5. Characterization of thermo-optic switch 87
5.3. Thermo-optic devices: variable optical attenuator (VOA) 92
5.3.1. Design 92
5.3.2. Characterization of VOA structures 93

6. Fiber pigtailing of waveguide chips 95
6.1. Coupling efficiencies and alignment tolerances 95
6.2. Active fiber alignment 97
6.3. Passive fiber alignment 101

7. Environmental tests 105
7.1. Telcordia specifications 105
7.2. Environmental tests with waveguide chip 106
7.3. Environmental tests with fiber-pigtailed chip 107

8. Additional technology and device studies for planar lightwave circuits 111
8.1. Waveguide fabrication with liquid crystal polymers 112
8.1.1. Refractive index measurement 113
8.1.2. Waveguide characterization 115
8.2. Microring structure for wavelength filtering 117
8.2.1. Motivation 117
8.2.2. Fabrication tolerant design of a micro ring structure 118

9. Conclusion and outlook **125**
9.1. Conclusions 125
9.2. Outlook 126
10. References **129**
List of abbreviations and variables 135
Publications and conference contributions 136
Acknowledgements 137
Curriculum vitae 138

Abstract

Polymer materials have shown to be good candidates for future planar lightwave circuits. They have a low optical loss at telecom wavelength. Additionally, with the appropriate chemical knowledge the material properties can be tuned and functional molecules for electro-optic response or amplification can be added.
Another important advantage of these materials is the possibility of using fast fabrication processes that provide a low cost mass production of optical devices, i.e. replication or UV-writing. However, for a consequent low-cost production of integrated optical components these efficient fabrication technologies have to be combined with an inexpensive approach for the packaging of the waveguide chip.

In the present work several polymer materials were evaluated for waveguide production with the focus on a reliable processing, a reduction of optical loss and an improvement of the material stability. Additionally, the thermo-optic coefficient and thermal conductivity were measured.
As an efficient fabrication technology for optical waveguides direct UV-printing was chosen, where the waveguides are formed in one photolithographical step.
The developed waveguides provide a solid basis for integrated devices. Therefore, first optical components were designed and tested. Polymer waveguides are potentially used for passive devices like power splitters and combiners as well as thermo-optic devices like optical switches or variable optical attenuators. These devices were characterized on their insertion loss and power consumption with results close to the standard specifications given for the according device.
For the fiber assembly two approaches were investigated in this work:

- Active alignment with fiber arrays
- Passive alignment with a fixing of the waveguide chip and the fibers on a common substrate

The development of these assembly processes was initialized and first results were achieved. Both processes showed to be valuable approaches, although further development and optimization is still needed.

In addition to the above described work a fabrication process for optical waveguides was developed using photo-aligning polymers and liquid crystal polymers. A proof of principle could be achieved with waveguides of 10µm width.
Furthermore a theoretical study on a micro-ring structure for wavelength filtering was carried out. The analyzed structure lowers the required fabrication tolerances, which are often limiting the performance of micro-ring devices.

1. Introduction

1.1. Aim of this work

Integrated optics based on polymer materials has been studied for more than two decades [1][2]. The potentially low material costs and the flexible control over certain material parameters are obvious advantages to other material system. But the relatively high optical loss and the insufficient environmental stability of the available polymers have been a limitation for a long time.
The main goals of this thesis are resumed in the following points:

- Evaluation of different polymer materials for optical waveguides using reactive ion etching (RIE) and direct UV-printing for the waveguide fabrication
- Development of a fast and reliable fabrication process using photopolymerizable materials
- Design, fabrication and characterization of integrated optical devices based on polymer waveguides, i.e. power splitters and thermo-optic switches
- Evaluation of active and passive alignment procedures for fiber-pigtailing waveguide chips
- Environmental tests with waveguide chips as well as with fiber-pigtailed waveguide chips.

1.2. State-of-the-art in integrated optics for telecom applications

In contrast to the electronic integration with silicon as dominating material technology, the preferred material technology for integrated optics always depends on the final application of the optical device [3]. For light emission semiconductor devices are favored [4]. Light amplification is efficient in semiconductor as well as in erbium doped silica waveguides or

fibers [5][6]. Silica waveguides are used when waveguides with low optical loss are needed [7][8]. A lot of work has also been carried out for integrating optical functions directly into optical fibers [9][10]. The only material that is currently claimed to potentially become an overall optical material is again silicon [11][12][13].
In the last years sophisticated micro-optical and integrated devices based on semi-conductor and silica technology have been developed (i.e. time/wavelength multiplexer and demultiplexer, amplifier, dispersion compensator, variable optical attenuator, modulator). These devices made the installation of today's high-speed transmission lines in telecom networks possible (see Fig. 1-1).
However, further integration of several optical components in one integrated photonic circuit is still a long-standing goal. As a mid-term concept hybrid integration is proposed. This includes two different technologies:

- Different materials can be used on the same chip. This allows placing structures with different optical functions on the same chip. E.g. an active semiconductor structure can be placed on the same chip with low index contrast polymer waveguides.
- Multiple planar lightwave circuits (PLC) are directly connected without any fibers in between (Fig. 1-2) [14]. As the single PLCs are fabricated separately the yield for the total system is higher. Additionally, each component can consist of different materials.

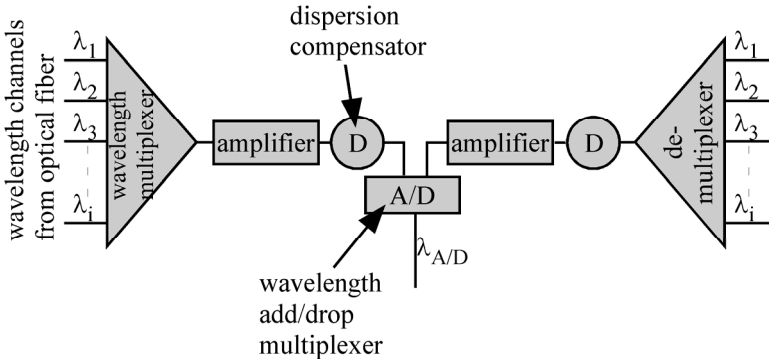

Fig. 1-1: Network node of a wavelength division multiplexed (WDM) transmission system.

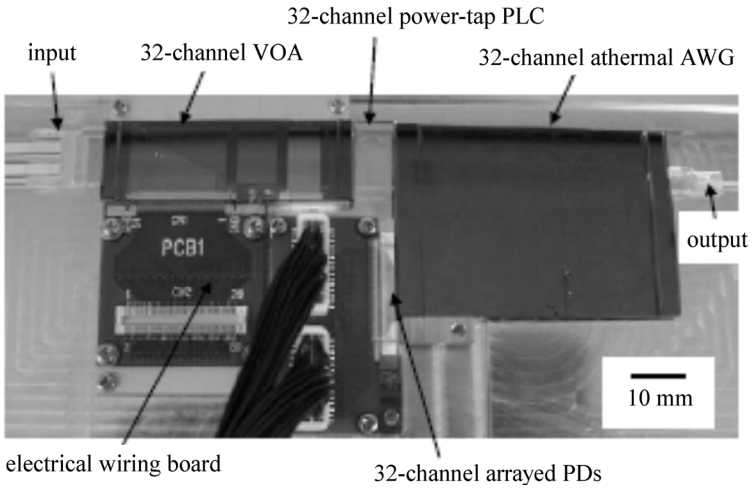

Fig. 1-2: Hybrid integration of multiple planar lightwave circuits as shown by NTT.

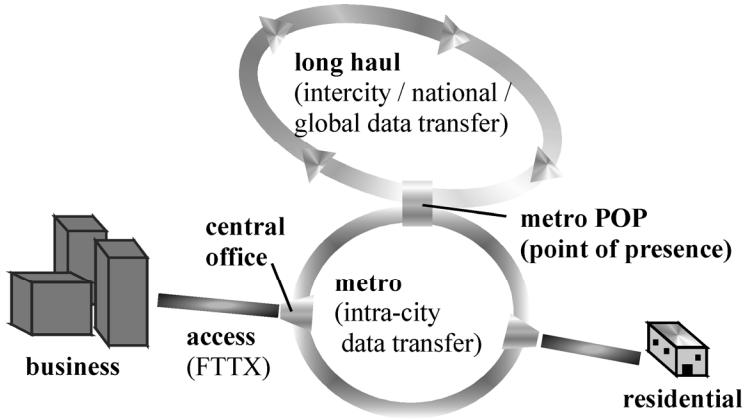

Fig. 1-3: Network landscape: The development of last years optical components increased the transmission speed of optical data in long haul networks dramatically. In optical access networks (FTTX: fiber-to-the-home / -costumer / -business) optical data are transferred to the end user.

The driving force in device development for the last years was often the desire to make low loss waveguide and fast devices for higher bit-rates in transmission systems. Today, two new trends have become important:

- For optical components as building blocks of high performance networks a denser integration of optical structures is needed. Therefore, waveguide structures with a high refractive index contrast have to be built. Silicon or indium phosphide wires have been used to realize optical components of very small size [15][16]. In photonic crystals low loss waveguide with 90° corners have been shown [17].
- Instead of improving the performance of optical devices, inexpensive and reliable technologies are demanded for the fabrication of devices. Here, polymer materials with their various methods for structuring waveguides have gained more and more interest [18][19]. Inexpensive technologies for the fabrication of optical devices lower the cost for the installation of optical networks bringing the optical fiber closer or even down to the end user (Fig. 1-3).

1.3. Integrated optics with polymer materials

As mentioned above, polymer materials always had the drawback of an insufficient environmental stability and a relatively high absorption at the usual telecom wavelengths in the C-band (1525nm-1565nm) and in the L-band (1565nm-1625nm). Nowadays specifically developed polymers with good cross-linking between the polymer-chains can withstand the required environmental tests (usually Telcordia tests). Polymer waveguides have been fabricated with a propagation loss below 0.1 dB/cm (Fig. 4-1), which is comparable to the loss in silica waveguides [20][21]. The polymers mainly used in this work are commercially available from ChemOptics (formerly ZenPhotonics). As it will be shown later, this material provides a good stability and waveguides with a propagation loss of 0.4 dB/cm were produced.
There are various techniques for structuring polymer layers. The most common approach is reactive ion etching (RIE) with an O_2-plasma. This fabrication method is applicable to almost any polymer material and enables an exact definition of the waveguide structures (Fig. 1-4).

company/group	material [trade name]	fabrication technique	optical loss @ 1,55µm
Asahi Glass	[Cytop™]		0.1 dB/cm
Corning	acrylate / halogenated acrylate	wet etch, RIE, laser ablation	0.8 dB/cm / 0.2 dB/cm
ChemOptics (formerly ZenPhotonics)	fluorinated acrylate	RIE	0.3-0.5 dB/cm
Dow Corning	Siloxane	RIE, UV-patterning	0.4 dB/cm
DuPont Photonics (Telephotonics)	[OASIC™]	wet etch, RIE, laser ablation	0.1 dB/cm
Gemfire	polysiloxane [Gemfire]	wet etch	1.0 dB/cm
JDS Uniphase (formerly Akzo Nobel)	polycarbonate [BeamBox™]	RIE	0.6 dB/cm
NTT	halogenated acrylate	RIE	1.7 dB/cm
	deuterated polysiloxane	RIE	0.43 dB/cm
Optical Crosslinks (formerly Dupont, Polymer Photonics)	acrylate [Polyguide™]	diffusion	0.6 dB/cm
Photon-X		RIE	0.05 dB/cm
RPO Ltd	polysiloxane	UV-patterning	0.7 dB/cm
Tetramer (polymer developed by Dow Chemical)	benzocyclobutene [Cyclotene™]	RIE	1.5 dB/cm
	perfluorocyclobutene	wet etch	0.25 dB/cm

Table 1-1: Overview on companies in optical waveguide fabrication with polymer materials [22].

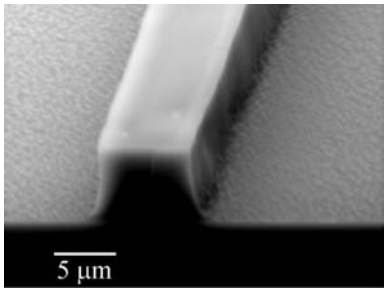

Fig. 1-4: Polyacrylate waveguide structured with reactive ion etching. The dimensions of the waveguides are 5µm x 5µm.

The drawback of RIE is that the process contains a lot of steps (see chapter 4.5.1). Therefore faster techniques have been developed such as:

- Replication:
  - UV-embossing
  - hot-embossing
  - …
- UV-printing
  - laser writing
  - photo-printing through a mask
  - …

Replication or photo-printing through a mask offer a fast fabrication for mass production, whereas laser writing guarantees a high flexibility for prototyping. The quality of the resulting waveguide structures is strongly depending on the polymer properties. In this work, results on waveguides structured with RIE and UV-printing will be presented. RIE was used as a first standard approach giving an idea about the achievable waveguide quality. Later on, a process using direct UV-printing was established for an efficient waveguide production. The results achieved with this fabrication technique are comparable to other groups (Table 1-1). For an extensive comparison not only the propagation loss, but also the fabrication yield and reliability has to be considered.
A further advantage of polymer materials is the intrinsically high thermo-optic coefficient. This coefficient is roughly one order of magnitude larger than in silica, which provides the possibility of making low power thermo-optic devices. Furthermore, with the adequate chemical knowledge other

functions such as light amplification or electro-optical modulation can be implemented in polymer materials [22]-[24].

1.4. Fiber pig-tailing of optical chips

In microelectronics, packaging is usually referred to the encapsulation of a chip into a form that provides an easy connection to a circuit board. For optical devices the packaging includes not only the mechanical stabilization, thermal management and electrical connection but also optical connections.
The packaging of waveguide chips takes up to 80% of the fabrication costs. Therefore the fast fabrication methods for polymer waveguides are only a real advantage if they are combined with a relatively low-cost packaging. The encapsulation of a device can be simplified if the waveguide chip itself is environmentally stable and no hermetic package is needed. For the fiber pig-tailing, alignment tolerances in the micrometer range must be reached and maintained after the fixing. Processes that can not guarantee this precision reduce the performance of the device dramatically.
Two approaches that provide an efficient alignment of the input and output fibers will be evaluated in chapter 6 of this thesis:

- Active alignment of fiber arrays:
  Fiber arrays with a standardized pitch of 250µm from one fiber to the next fiber are used to allow a simultaneous alignment of fibers for multiple inputs or outputs.
- Passive alignment:
  The alignment between chip and fiber can also be guided by alignment structures on a common substrate. With this technique the critical steps are shifted from the fiber alignment to the exact fabrication of the substrate and the precise placement of the waveguide chip onto the substrate. However, there is no need of a fiber alignment procedure once the waveguide chip is positioned on the substrate.

In both techniques different parts must be bonded together. The bonds must guarantee that the device performance is within the specifications during environmental tests. UV-curable adhesives offer an easy and flexible way to bond parts together. Although the reliability of adhesives has often been questioned, they are increasingly used in optical packaging due

to further material development and new releases of adhesives [25]. The environmental tests carried out with our developed fiber pig-tailed waveguides show the stability and performance of some commercially available adhesives.

1.5. What is new in this work

Previous work with polymer materials in integrated optics focused on the improvement of the optical performance of the optical waveguides and claimed the low costs of polymer materials as an advantage to other materials used in integrated optics. However, these low loss polymer materials often have an insufficient environmental stability and the material costs only contribute a relatively small part to the total fabrication costs of a device.
The results of this work show a consequent cost reduction in the whole fabrication process of an optical device including the fiber pigtailing. With a direct UV-patterning process a very efficient technology for the waveguide fabrication could be developed with processing times below one hour. For the fiber assembly the development of a passive alignment process has been initialized. This process provides an easy alignment of several fibers to a waveguide chip without long alignment procedures.
The packaging of a fiber pigtailed device adds an important part to the final device cost. Therefore, special attention has also been paid to the environmental stability of the waveguide chip and the adhesives used for the fiber pigtailing. With a stable polymer material it is possible to simplify the encapsulation of the device and therefore to save costs in the packaging.
Based on the fabrication process described above devices have been fabricated. Among others, a digital optical switch based on a Y-splitter with an extremely large opening angle has been designed and fabricated. The special design of the Y-junctions provides a very low driving power of only 40mW.
Another novel waveguide fabrication technique has been developed based on liquid crystal polymers. These materials are known to be very stable. As the polymer chains in these materials can be oriented with an exposure to polarized UV-light, regions with different polymer orientation and therefore different refractive index can be defined. The waveguide fabrication process based on this principle is also very fast. It has been shown

that infrared light at telecom wavelengths can be guided through a 10μm wide waveguide.
A theoretical study on the design of devices based on microring resonators has been carried out. The design focuses on a relaxation of the precision requirements in a fabrication process. Such a design could allow the fabrication of such devices with low cost technologies suitable for mass production.

2. Optical Waveguide Theory

Optical waveguides are defined by a waveguide core and a surrounding waveguide cladding. The light guiding property is ensured by total internal reflection as the refractive index of the core material is higher than the one of the cladding material. In slab waveguides the refractive index is constant within a layer and the light is only confined in one dimension, whereas a confinement in two dimensions is present in channel waveguides (Fig. 2-1).
The refractive index contrast

$$\frac{n_{co} - n_{cl}}{n_{co}} \qquad (2\text{-}1)$$

of the core and cladding refractive index (n_{co} and n_{cl}) can vary from 0.3% (optical fiber) to up to more than 50% for semiconductor waveguides. A waveguide with a refractive index contrast not exceeding a few percent is called weakly guiding. Channel waveguides of this type will be considered in this thesis.

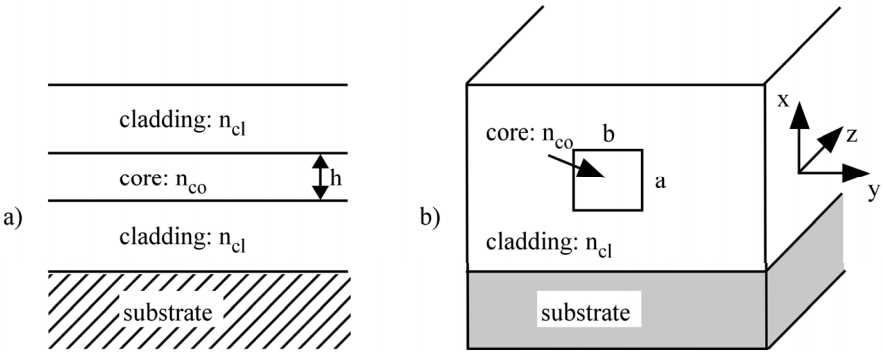

Fig. 2-1: Refractive index distribution for a) a slab waveguide and b) a rectangular channel waveguide with $n_{co} > n_{cl}$.

2.1. Waveguide modes

The intensity distribution of the guided light in a waveguide is expressed by the guided modes. The number of guided modes depends on the size and the refractive index contrast of the waveguides. Each mode is defined by the distribution field amplitude (Fig. 2-2) and it's the propagation constant β, where the propagation constant is defined by [26]

$$\beta = k_0 n_{eff} \quad \text{with} \qquad (2\text{-}2)$$

$$k_0 = 2\pi / \lambda \quad . \qquad (2\text{-}3)$$

λ is the wavelength and n_{eff} is the effective index associated to a guided mode.
The first guided mode has the largest effective index. For higher order modes the effective index decreases. If the effective index approaches the refractive index of the cladding material n_{cl}, cutoff is reached, where the corresponding mode is not guided anymore. In integrated optical devices, single mode waveguides are favored. Modal dispersion (different propagation constants for each mode) in multimode waveguides limits the bandwidth of optical transmission systems. Additionally, the coupling between the different modes leads to undefined intensity distribution in the waveguide.

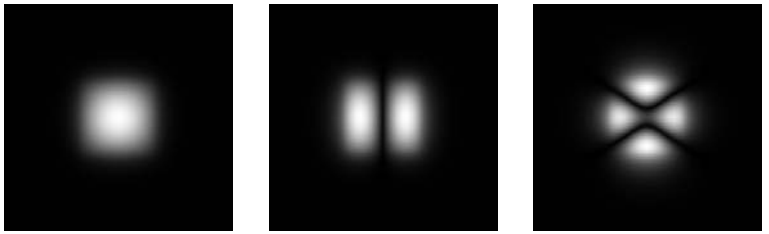

Fig. 2-2: Mode fields (field amplitude |E|) of the first three modes (TE-polarization) in a multimode channel waveguide. The core dimensions are 10µm x 10µm. The refractive indices are $n_{co} = 1.46$ and $n_{cl} = 1.45$.

2.1.1. Wave equation

For the waveguide geometry shown in Fig. 2-1, both the electric field vector ***E*** and the magnetic field vector ***H*** are orthogonal to each other as well as to the propagation vector ***k***. There are two possible polarizations

with $H_z = 0$ and $E_z = 0$, respectively. The former polarization is called the transverse magnetic (TM) and the latter is called the transverse electric (TE) polarization.
The electric and magnetic fields obey the wave equations:

$$\nabla^2 \boldsymbol{E} - \mu\varepsilon \frac{\partial^2 \boldsymbol{E}}{\partial t^2} = 0$$
$$\nabla^2 \boldsymbol{H} - \mu\varepsilon \frac{\partial^2 \boldsymbol{H}}{\partial t^2} = 0 \qquad (2\text{-}4)$$

These wave equations are valid for homogenous or nearly homogenous materials with $\nabla\varepsilon \approx 0$. The dielectric permittivity ε and the magnetic permeability μ are generally frequency dependent. This frequency dependence is called the material dispersion. For non-magnetic and transparent materials, as considered in this thesis, the two material parameters can be written as

$$\varepsilon(\omega) = \varepsilon_0 \varepsilon_r(\omega) = \varepsilon_0 n^2(\omega)$$
$$\mu(\omega) = \mu_0 \mu_r(\omega) = \mu_0 \qquad (2\text{-}5)$$

with

ε_0 = 8.8542 x 10^{-12} $AsV^{-1}m^{-1}$ (permittivity of free space)
μ_0 = 1.2566 x 10^{-6} $VsA^{-1}m^{-1}$ (permeability of free space)
$\varepsilon_r(\omega)$ = relative permittivity
$\mu_r(\omega)$ = 1 = relative permeability
$n(\omega)$ = refractive index
ω = $2\pi\nu$ = angular frequency
ν = c/λ = frequency of light
c = speed of light

For the description of a guided wave we assume that the electro-magnetic wave has a single frequency and that the dependence in the longitudinal direction is described by $\exp(i\beta z)$. Then the electro-magnetic wave are given by

$$E(x, y, z) = E(x, y)\, e^{i(\beta z - \omega t)}$$
$$H(x, y, z) = H(x, y)\, e^{i(\beta z - \omega t)} \qquad (2\text{-}6)$$

and the wave equation can be rewritten as

$$\frac{\partial^2 E(x,y)}{\partial x^2} + \frac{\partial^2 E(x,y)}{\partial y^2} + \left[k_0^2 n_i^2 - \beta^2\right] E(x,y) = 0$$
$$\frac{\partial^2 H(x,y)}{\partial x^2} + \frac{\partial^2 H(x,y)}{\partial y^2} + \left[k_0^2 n_i^2 - \beta^2\right] H(x,y) = 0 \qquad (2\text{-}7)$$

where n_i stands for the refractive index in the core and the cladding region, respectively.
There are several methods for solving the wave equation and analyzing rectangular channel waveguides [26]. Marcatili has developed a method [27] giving an approximate analytical solution based on the assumption that the modes are far from cutoff or the refractive index contrast between the core and the cladding material is small. A more general and widely used method is the effective index method, developed by Hocker and Burns [28]. The effective index converts the problem of a channel waveguide into two orthogonally oriented slab waveguides. Software packages with mode solver often use the finite difference or the finite element method (see chapters 3.2 and 3.3). These methods are more time consuming, but also more precise and applicable to all possible waveguide shapes.

2.1.2. Characteristic equation for slab waveguide

For simplicity the characteristic equations describing the guided modes in a slab waveguide are given here. Via the effective index method it is straightforward to calculate also the mode profiles for channel waveguides. Due to the independence of a slab waveguide on the lateral y-direction the wave equation (2.8) for the electrical field is simplified to

$$\frac{\partial^2 E(x,y)}{\partial x^2} + (k_0^2 n_i^2 - \beta^2) = 0 \ . \qquad (2\text{-}8)$$

An oscillating field in the core region is only possible for $\beta < n_{co} k_0$. On the other hand, it was mentioned above that the mode is only guided above cutoff for $\beta > n_{cl} k_0$. Therefore, the guided mode condition

$$n_{cl} k_0 < \beta < n_{co} k_0 \qquad (2\text{-}9)$$

has to be fulfilled. The solution of the wave equation then is oscillatory in the core region and exponentially decaying in the cladding region. Therefore the field amplitude of a TE-wave is described by

$$E(x) = A\cos(\kappa x - \phi) \quad \text{for the core}: 0 < x < h \qquad (2\text{-}10)$$

$$E(x) = Be^{\gamma x} \quad \text{for the cladding}: x < 0 \qquad (2\text{-}11)$$

$$E(x) = Ce^{-\gamma(x-h)} \quad \text{for the cladding}: x > h \qquad (2\text{-}12)$$

A, B and C are amplitude coefficients and γ and κ are defined as

$$\gamma = \left[\beta^2 - k_0^2 n_{cl}^2\right]^{1/2}$$
$$\kappa = \left[k_0^2 n_{co}^2 - \beta^2\right]^{1/2} . \qquad (2\text{-}13)$$

Applying the boundary conditions for the tangential field component across each interface, the characteristic eigenvalue equation giving the propagation constant β for the TE modes becomes:

$$\tan\left(\frac{\kappa h}{2}\right) = \frac{\gamma}{\kappa} \quad \text{for even modes} \qquad (2\text{-}14)$$

$$\tan\left(\frac{\kappa h}{2}\right) = -\frac{\kappa}{\gamma} \quad \text{for odd modes} . \qquad (2\text{-}15)$$

Similarly the characteristic equations for the TM modes are given by

$$\tan\left(\frac{\kappa h}{2}\right) = \left(\frac{n_{co}}{n_{cl}}\right)^2 \frac{\gamma}{\kappa} \quad \text{for even modes} \qquad (2\text{-}16)$$

$$\tan\left(\frac{\kappa h}{2}\right) = -\left(\frac{n_{co}}{n_{cl}}\right)^2 \frac{\kappa}{\gamma} \quad \text{for odd modes} . \qquad (2\text{-}17)$$

When the left and the right side of the characteristic equation are plotted as a function of the effective index *neff*, each intersection point represents a guided mode (Fig. 2-3). Herewith the number of guided modes and their effective index can be deduced.

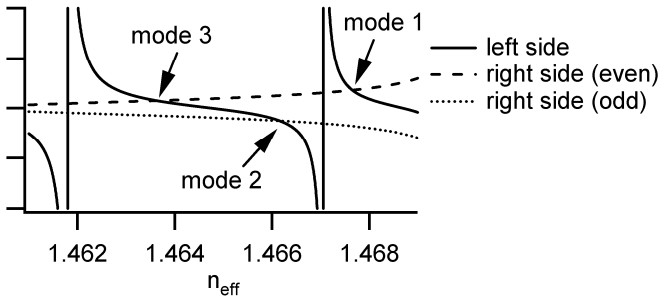

Fig. 2-3: The left and the right side of the characteristic mode equation (2-16) and (2-17) for TE modes are plotted as a function of the effective index *neff*. Each intersection point represents a guided mode. The following parameters are assumed: n_{co} = 1.47, n_{cl} = 1.46, h = 25µm, λ = 1.55µm.

2.2. Optical loss

When propagating through a lossy optical waveguide, the guided waves show an exponential attenuation:

$$I(z) = I_0 e^{-\alpha z} \qquad (2\text{-}18)$$

This attenuation is often given as

$$\alpha_{dB} = 10 \times \frac{1}{z}\log\left(\frac{I(z)}{I_0}\right) \qquad (2\text{-}19)$$

with α in dB/cm.
Basically, there are three fundamental types of loss: absorption loss, scattering loss and radiation loss due to mode mismatch or bends. Optical waveguides for integrated optics should have a total propagation loss of less than 1 dB/cm. For low loss optical waveguides the attenuation has to be less than 0.1dB/cm.

2.2.1. Absorption loss

Absorption loss occurs due to atomic or molecular absorption or band-to-band electronic absorption of electro-magnetic energy. The refractive

index of a material is generally given by $n = n' + in''$. The real part represents the refractive index of a fully transparent material. The imaginary part of the refractive index is related to the attenuation coefficient

$$\alpha_{absorption} = 2k_0 n'' \,. \qquad (2\text{-}20)$$

2.2.2. Scattering loss

There are three dominant mechanisms that lead to scattering loss:

- Fluctuations in the refractive index of the waveguide material
- Roughness at interfaces between core and cladding of the waveguide
- Bulk scattering from dust or other impurities

For most of the optical waveguides in integrated optics the used materials have a good homogeneity ($\Delta n < 0.008\%$). Consequently, the major scattering mechanism is based on surface roughness and particles (e.g. dust, crystallized polymer) in the waveguide core. The surface scattering can be reduced by the choice of small refractive index contrasts between core and cladding material. The scattering loss increases approximately with the difference of the squares of the effective index and the refractive index in the cladding $(n_{eff}^2 - n_{cl}^2)$ [29][30]. This relation implies that surface scattering is important for high index waveguides like silicon on insulator (n_{co} = 3.47, n_{cl} = 1.45). In polymer waveguides with a small refractive index difference of $\Delta n \cong 0.01$ scattering loss is less critical.
An approximation for the scattering loss is given in [34]:

$$\alpha_{scat} \cong \sigma^2 \left(n_{eff}^2 - n_{cl}^2\right) k_0^2 \frac{\kappa}{\beta} \left(E_1^2 + E_2^2\right) \qquad (2\text{-}21)$$

E_1 and E_2 are the values of the normalized modal fields at the inner and outer interface of the waveguide, κ is the transverse component of the propagation constant as defined in equation 2-13 and σ^2 is the mean square of the surface roughness.

2.2.3. Bending loss

The trend in integrated optical devices aims to minimize the device size in order to increase the number of chips per wafer and to reduce the propagation distance and therefore the total propagation loss. To achieve this goal a minimal bend radius has to be evaluated that still ensures a low propagation loss. For weakly guided modes in polymer waveguides, this minimal bend radius is several millimeters.
The radius of curvature influences the mode profile of the guided wave. The center of the mode is slightly moved to the outer core-cladding interface. Therefore, a transition loss occurs when the radius of curvature changes. Additionally, as the mode profile is not centered in the waveguide core, the light intensity at the core-cladding interface is larger than in straight waveguides. Therefore the wave is more sensitive to surface roughness and the scattering loss increases.
Pure bending loss can be described as radiation loss [1] and can be described with the following model. The phase front of a guided wave remains planar around a bend. Consequently the phase velocity increases with increasing distance from the center of the curvature. At a certain point on the outer side of the bent waveguide the phase velocity would exceed the speed of light. Therefore, the outer tail of the mode radiates outside the guiding structure (Fig. 2-4).

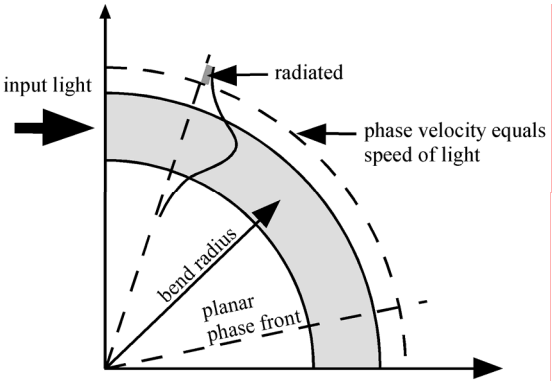

Fig. 2-4: Schematic view for the description of pure bending loss.

The calculation of the bending loss is a difficult task. The final bending loss depends sensitively on the parameters of the fabricated waveguide, such as the surface roughness or the shape of the waveguide core. For a pure bending loss in slab waveguides a quantitative expression was derived by Marcuse [31]. The approximation for the attenuation coefficient describing the exponential wave attenuation is given by

$$\alpha = \frac{\gamma\kappa^2 e^{h\gamma} e^{-U}}{(n_{co}^2 - n_{cl}^2)k_0^2\beta(h/2 + \gamma^{-1})} \qquad (2\text{-}22)$$

where

$$U = \left[\frac{\beta}{\gamma}\ln\left(\frac{1+\gamma\beta^{-1}}{1-\gamma\beta^{-1}}\right) - 2\right]\gamma R \approx \frac{2\gamma^3 R}{3\beta^2} \; . \qquad (2\text{-}23)$$

γ and κ are defined in chapter 2.1.2, R is the bend radius and h is the height of the slab waveguide. The approximation is valid for

$$n_{cl}k_0\left(1+\frac{h}{2R}\right) < \beta < n_{co}k_0\left(1-\frac{h}{2R}\right) \; . \qquad (2\text{-}24)$$

For channel waveguides the bend loss can be approximated by using the Marcuse approximation in combination with the effective index method or they can be computed numerically e.g. using Wenzel-Kramers-Brillouin (WKB) techniques [32][33] or the finite difference method (see chapter 3.1.2).

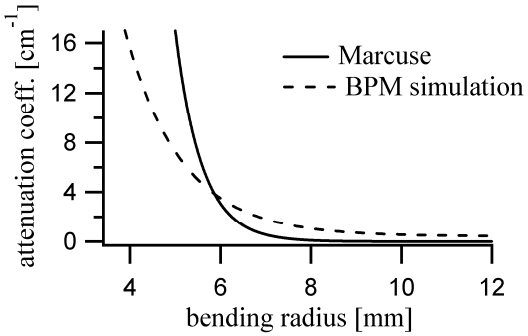

Fig. 2-5: Attenuation coefficient corresponding to pure bending loss as a function of the bending radius for a square channel waveguide with n_{co}=1.47 and n_{cl}=1.46 and a core dimension of 5µm x 5µm. The full line represents the Marcuse approximation and the dashed line shows a simulation based on a BPM simulation using the Apollo Photonics Solution Suite software.

Generally, the attenuation coefficient α increases exponentially as the bending radius decreases. Consequently, at a certain radius the bending

loss increases dramatically when the radius is further reduced. The above approximations give only rough estimations on the bending loss as a function of the radius, but they help to find the critical radius where the bend loss starts to become important. Fig. 2-5 shows the attenuation coefficient corresponding to pure bonding loss for a square channel waveguide with a core dimension of 5µm x 5µm, n_{co}=1.47 and n_{cl}=1.46. The full line is calculated using the Marcuse approximation combined with the effective index method. The dashed line shows the result of a simulation with the Apollo Photonics Solution Suite software. The simulation is based on the beam propagation method (see chapter 3.1). Although the two calculations of the attenuation coefficient clearly differ from each other, they both show that the bending loss starts to increase for a bending radius below 9mm. This result is also comparable to glass fibers, where bending radii below 6mm are usually avoided.

2.3. Mode Coupling

Coupling between different guided modes in waveguide structures is generally present in two situations:

- Transitions from one waveguide type to another (e.g. transition from a straight to a bent waveguide or from a fiber to a waveguide) lead to a coupling loss.
- When waveguides are close together the modes of the waveguides overlap and coupling from one waveguide into the other takes place.

Coupling loss can be minimized by designing (nearly) mode matched structures and by varying waveguide parameters adiabatically. The coupling between adjacent waveguides is used in directional couplers which are present in devices such as power splitters or microring filters.

2.3.1. Coupling efficiency at waveguide transitions and interfaces

At transitions between two different waveguides 1 and 2, the coupling efficiency is defined by the ratio of the light power in the first waveguide versus the light power that couples into the second waveguide. Let E_1 and E_2 be the normalized field of the fundamental mode in waveguide 1 and 2, respectively. The coupling efficiency is then given by the overlap integral

$$\eta = \iint_{xy} E_1^*(x,y)\, E_2(x,y) dxdy \quad . \tag{2-25}$$

An analytic expression can be derived [35] for the coupling efficiency when a Gaussian field distribution is assumed. The Gaussian field distribution is quite similar to the real cosine shape of the guide mode. Additionally it allows calculating the field propagation in free space, which is needed when gaps are between two waveguide structures. With the Gaussian approximation for the two involved mode profiles the coupling efficiency as a function of the lateral, the longitudinal and the angular misalignment is then given by

$$\eta_{gauss} = a \cdot \exp\left(-a \left\{ x_0^2 \frac{\left(w_1^{-2} + w_2^{-2}\right)}{2} + \theta^2 \frac{\left(w_1^2(z) + w_2^2\right)\pi^2}{2\lambda^2} - x_0 \theta z \frac{1}{w_1^2} \right\} \right) \tag{2-26}$$

where

$$a = \frac{4 w_1^2 w_2^2}{(w_1^2 + w_2^2)^2 + z^2 \dfrac{\lambda^2}{\pi^2 n_{gap}^2}} \tag{2-27}$$

$$w_1^2(z) = w_1^2 \cdot \left[1 + \left(\frac{\lambda z}{\pi w_1^2} \right)^2 \right] \quad .$$

w_1 and w_2 are the beam waists of the Gaussian field in waveguide 1 and 2, respectively. The misalignment is described by the parameters x_0, z and θ as shown in Fig. 2-6. The refractive index of the medium between the waveguide is given by n_{gap}.

For a perfect lateral and angular alignment ($x_0 = 0$, $\theta = 0$) of two identical waveguides ($w_1 = w_2$) a simplified expression is obtained describing the dependence of the coupling efficiency on the z-alignment:

$$\eta_{gauss}(z) = \left[1 + \left(\frac{z\lambda}{2 w_1^2 n_{gap} \pi} \right)^2 \right]^{-1} \tag{2-28}$$

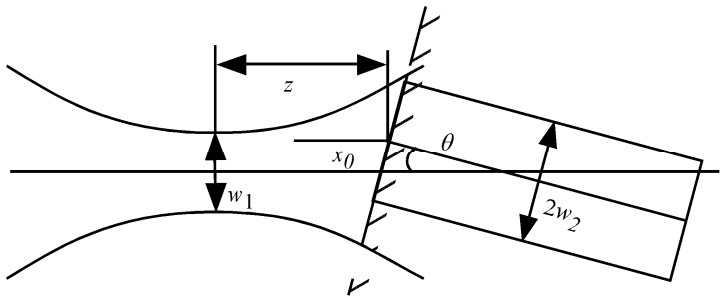

Fig. 2-6: Geometry for coupling between an incoming beam (e.g. from an optical fiber) and a waveguide. The mode shapes are assumed to be Gaussian.

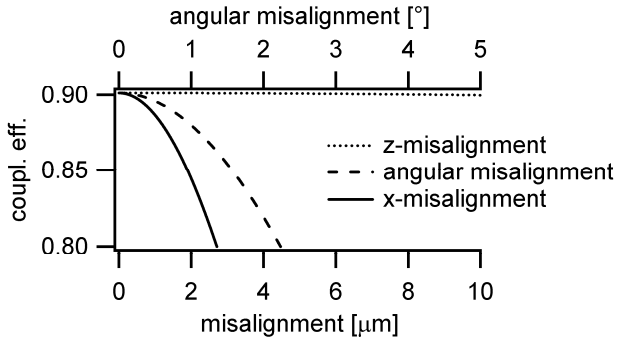

Fig. 2-7: Coupling efficiency between a polymer waveguide and an optical fiber with a pure lateral, angular or longitudinal misalignment, respectively. The coupling efficiencies are deduced from equation (2-28).

The influence of the lateral and the angular alignment with the two waveguides in contact ($z = 0$) is expressed in the following equation:

$$\eta_{gauss}(x_0, \theta) = a \cdot \exp\left[-\left(\frac{x_0}{w_1} \right)^2 - \left(\frac{\theta}{\lambda / w_1 \pi} \right)^2 \right] \tag{2-29}$$

The two equations above show, that for coupling light from one waveguide to the other the lateral and angular alignments are most critical because of the exponential decay. Fig. 2-7 shows the coupling efficiency between a polymer waveguide and an optical fiber calculated with equation (2-28). Especially in the lateral direction alignment tolerances of less than 1μm are often required.

An additional loss source is the Fresnel reflection at the interfaces. At an air-fiber or air-polymer interface ($n_{air} = 1$, $n_{co} \approx 1.45$) Fresnel reflection causes an additional loss of approximately 4%. This loss is minimized by bringing the waveguides into contact or filling the gap between the waveguides with an index matched medium.

2.3.2. Directional coupling between waveguides

Guided modes have an evanescent field outside the core region of the waveguide. If two waveguides are close enough to each other that their evanescent fields overlap (approximately the width of the waveguide core), light is coupled from one waveguide to the other. The performance of such a directional coupler is described in the coupled mode theory.
In the slowly varying amplitude approximation, where the coupling between the waveguide modes is weak, the total electric field of the waveguides 1 and 2 can be written as

$$E(x,y,z) = C_1(z)E_1(x,y)e^{-i\beta_1 z} + C_2(z)E_2(x,y)e^{-i\beta_2 z} \quad . \qquad (2\text{-}30)$$

$C_1(z)$ and $C_2(z)$ are the amplitudes of the modes in waveguide 1 and 2, respectively. By inserting this field into the wave equation the following expression is obtained:

$$\left[\frac{d^2C_1}{dz^2} - 2i\beta_1\frac{dC_1}{dz} + k_0^2\left(n_{cl}^2 - n_{co1}^2\right)C_1\right]E_1e^{-i\beta_1 z} + \left[\frac{d^2C_2}{dz^2} - 2i\beta_2\frac{dC_2}{dz} + k_0^2\left(n_{cl}^2 - n_{co2}^2\right)C_2\right]E_2e^{-i\beta_2 z} = 0 \qquad (2\text{-}31)$$

For weak coupling, where the waveguide cores are not too close to each other (not less than half of the width of the waveguide core), the following approximations are generally taken in account [26]:

- The power transfer from one waveguide to the other is slow. Consequently the second order derivative terms can be neglected.
- The presence of the adjacent waveguide does not influence the field distribution of the guided mode in a waveguide.
- The spatial overlap of the guided modes is small.

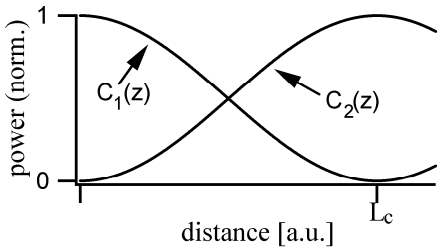

Fig. 2-8: Power transfer between to adjacent identical waveguides following the coupled mode equation based on weak coupling approximations.

Considering these approximations and by multiplying the coupled mode equations with E_1^* and integrating over the whole coupling cross section one gets the simplified expressions

$$\frac{dC_1}{dz} + i\kappa_{12}C_2e^{-i\Delta\beta z} = 0$$
$$\frac{dC_2}{dz} + i\kappa_{21}C_1e^{+i\Delta\beta z} = 0 \qquad (2\text{-}32)$$

with

$$\Delta\beta = \beta_2 - \beta_1$$
$$\kappa_{12} = \frac{k_0^2}{2\beta_1}\int_{xy}\left(n_{cl}^2 - n_{co2}^2\right)E_2E_1^*dxdy \;/\; \int_{xy}E_1\cdot E_1^*dxdy \qquad (2\text{-}33)$$
$$\kappa_{21} = \frac{k_0^2}{2\beta_2}\int_{xy}\left(n_{cl}^2 - n_{co1}^2\right)E_1E_2^*dxdy \;/\; \int_{xy}E_2\cdot E_2^*dxdy \;.$$

κ_{12} and κ_{21} are known as the coupling coefficients from waveguide 2 to waveguide 1 and vice versa. For identical waveguides ($\Delta\beta = 0$ and $\kappa_{12} = \kappa_{21} = \kappa$) the solutions to the coupled mode equations are given by

$$C_1(z) = \cos(\kappa z)$$
$$C_2(z) = -j\sin(\kappa z) \;. \qquad (2\text{-}34)$$

Consequently, the powers in waveguide 1 and waveguide 2 are

$$P_1(z) = |C_1(z)| = \cos^2(\kappa z)$$
$$P_2(z) = |C_1(z)| = \sin^2(\kappa z)\ . \qquad \text{(2-35)}$$

Complete coupling or switching is achieved after a coupling length of $L_c = \pi / (2\kappa)$ (Fig. 2-8).

2.3.3. Asymmetric coupling

As described in the previous chapter, the coupled mode theory is an approximation for weak coupling between waveguides with a gap at least as large as half of the waveguide size. Also, the theory is not applicable for the coupling between two different waveguides, because in this theory energy is only conserved if the coupling from waveguide 1 to waveguide 2 is equal to the coupling from 2 to 1. Therefore an adapted and more general coupled mode theory has been proposed in [36] by Chuang. Here, the coupling coefficients κ_{12} and κ_{21} are derived from a reciprocity relation. Other proposed theories like the Hardy-Streifer-Theory [37] or the theory of Haus et al. [38] are also applicable to asymmetric coupling structures and give identical results.
According to the reciprocity theorem the input and output wave must be identical, when the wave has propagated along an optical device, then has been reflected by a phase conjugating mirror and finally has propagated back through the same structure. The general reciprocity theorem derived from the Maxwell's equations is given by

$$\nabla \cdot \left(\boldsymbol{E}_1 \times \boldsymbol{H}_2 - \boldsymbol{E}_2 \times \boldsymbol{H}_1\right) = i\omega\left(\varepsilon_2(x,y) - \varepsilon_1(x,y)\right)\boldsymbol{E}_1 \cdot \boldsymbol{E}_2 \quad \text{(2-36)}$$

where the indices 1 and 2 still depict the two involved waveguides and ε_i is the dielectric constant of waveguide i in absence of the second waveguide.
By inserting the appropriate field expressions into the above equation the coupled mode equation can be derived as

$$\frac{d}{dz}\begin{bmatrix} C_1(z) \\ C_2(z) \end{bmatrix} = iK^{-1}S\begin{bmatrix} C_1(z) \\ C_2(z) \end{bmatrix}\ . \qquad \text{(2-37)}$$

K^{-1} and S are two 2 x 2 matrices with coefficients based on overlap integrals of the present fields as defined in [36]. Considering two identical waveguides, the product of the matrices is symmetric. For non-identical

waveguides the resulting matrix is asymmetric. Therefore the power fraction that is coupled from waveguide 1 to 2 within a certain distance is not the same as the power fraction coupled from 2 to 1. Nevertheless, the coupled equation system does not violate the reciprocity theorem and the power conservation.

3. Simulation of optical waveguide structures

For the design of PLCs suitable simulation tools are necessary. If there are no analytical solutions of a problem, numeric simulations have to be carried out solving the wave equation or the Maxwell's equation for a given input field and refractive index distribution. Depending on the specific structure to be designed more efficient or more rigorous simulation methods are appropriate. For the designs used in this work the software APSS (Apollo Photonics Solutions Suite) of Apollo Photonics and Femlab were mainly used. However, as each program for integrated optic design has its own advantages and disadvantages self-written programs in Matlab or Igor based on analytic approximations or based on the beam propagation method (BPM) are useful to check the reliability of the obtained results.
In simulations with APSS there is the choice of using BPM or the finite difference time domain (FDTD) method. Femlab is based on the finite element method (FEM).
All three methods are hardly applicable to three dimensional problems, unless computing power of several computers can be combined. Therefore, APSS uses an equivalent index for transforming three dimensional problems into two dimensions. The equivalent index is calculated in a mode solver when the guided mode is simulated in a cross-section of the waveguide. It is then used as the refractive index of the waveguide core in the two dimensional problem when the propagation of the field in a waveguide structure is simulated with BPM or FDTD. So the information on the third dimension of the waveguide structure is comprised in the equivalent index of the waveguide core. The structure is assumed to be uniform in this third dimension.

3.1. The beam propagation method

The beam propagation method is the fastest method to calculate the propagation of a guided mode along a waveguide structure. The efficiency

of this method is based on the fact that not the Maxwell's equation itself but directly the wave equation is solved [39]. Consequently only a slowly changing amplitude (varying in space) of the guided mode is considered and not the temporally fast oscillating optical field.
In contrast to the wave equation from chapter 2.1.1 the electric field amplitude *E(x,y,z)* depends now also on *z* as the waveguide structure has not necessarily to be uniform in this direction. Consequently the electrical field and the considered wave equation are now given by

$$E = E(x, y, z) \cdot e^{i(\beta z - \omega t)}$$

$$2i\beta \frac{\partial E}{\partial z} - \frac{\partial^2 E}{\partial z^2} = \frac{\partial^2 E}{\partial x^2} + \frac{\partial^2 E}{\partial y^2} + \left(k_0^2 n^2 - \beta^2\right) E \ . \qquad (3\text{-}1)$$

Generally, algorithms for the BPM do not solve this wave equation. If one assumes that the waveguide structure only changes slowly in the *z*-direction, the second order derivative with respect to z is neglected:

$$\frac{\partial^2 E}{\partial z^2} = 0 \qquad (3\text{-}2)$$

With this Fresnel approximation the governing wave equation for the BPM becomes

$$2i\beta \frac{\partial E}{\partial z} = \frac{\partial^2 E}{\partial x^2} + \frac{\partial^2 E}{\partial y^2} + \left(k_0^2 n^2 - \beta^2\right) E \ . \qquad (3\text{-}3)$$

However, this approximation limits the BPM to problems, where waveguide structures do only change moderately in the *z*-direction.
The simulation of a waveguide structure starts at $z = 0$ with a given input field. Then the evolution of the optical field along the *z*-direction is calculated in small steps Δz. With this procedure no feedback loops are considered as it appears in resonators. There is also no time dependence in the simulation.

3.1.1. Wide-angle BPM

For bends or Y-splitters with large opening angles the change in the z-direction cannot be neglected any longer and the Fresnel approximation is no longer suitable. In this case, the second order derivative with respect to *z* has to be taken into account, what is done in the Padé approximation

(or wide-angle BPM). Solving the wave equation formally without the Fresnel approximation, one gets

$$\frac{\partial}{\partial z}\left(1+\frac{i}{2\beta}\frac{\partial}{\partial z}\right)E=-\frac{i}{2\beta}PE \qquad (3\text{-}4)$$

with

$$P=\frac{\partial^2}{\partial x^2}+\frac{\partial^2}{\partial y^2}+\left(k_0^2n^2-\beta^2\right). \qquad (3\text{-}5)$$

With some simple transformation one gets

$$\frac{\partial E}{\partial z}=\frac{-iP/2\beta}{1+(i/2\beta)(\partial/\partial z)}E \qquad (3\text{-}6)$$

and the recurrence formula

$$\left.\frac{\partial}{\partial z}\right|_m=\left.\frac{-iP/2\beta}{1+(i/2\beta)(\partial/\partial z)}\right|_{m-1} \qquad (3\text{-}7)$$

can be defined. With the further definition

$$\left.\frac{\partial}{\partial z}\right|_{-1}=0 \qquad (3\text{-}8)$$

the Fresnel approximation is obtained for $m = 0$. With $n > 0$ the equation for the m^{th} wide angle order can be deduced.

3.1.2. Finite difference formulation

There are various kinds of BPM's, where the most frequently used is the finite difference (FD-) BPM. In this method the space coordinates are discretized. In a two dimensional example, the *z*- and *x*-coordinates are written as

$$\begin{aligned} z &= l\cdot\Delta z \\ x &= p\cdot\Delta x \end{aligned} \qquad (3\text{-}9)$$

where l and p are integers. The discretization of the space coordinates leads to a mesh with points (l,p) where the amplitude of the field is defined as $E(l,p)$ (Fig. 3-1).

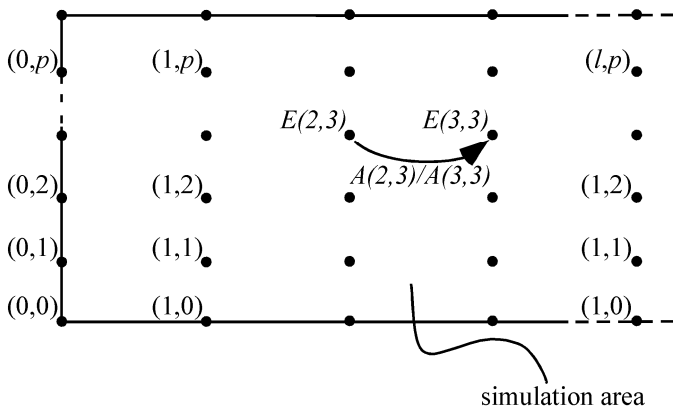

Fig. 3-1: Discretisation of the simulation area: p is the index of the mesh point in the lateral direction. With a given field distribution $E(0,p)$ at the left boundary the field propagation is calculated from the left to the right using the operator A which is defined by the waveguide structure.

As only the slowly varying amplitude is considered the discretization step Δz can be chosen to be relatively large, that is in the order of the wavelength. The discretization of the solved wave equation gives the dependence of $E(l,p)$ on the adjacent mesh points. The final discretised problem can schematically by written as

$$A(l+1)E(l+1)=A(l)E(l) \qquad (3\text{-}10)$$

where the operator A is given by the considered structure and the discretization steps. Therefore, with a given field amplitude E at $z = 0$ the evolution of the field amplitude in the z-direction can be calculated.
As these simulations always consider a certain simulation window artificial boundary conditions must be defined. These conditions must efficiently suppress reflections at the boundary. Frequently used is the transparent boundary condition (TBC) as developed by Hadley [41].

3.2. The finite difference time domain (FDTD) method

When simulating waveguide structures with rapidly changing geometries along the direction of propagation or with feedback loops like a resonator, reflections and information on the phase of the propagating field become important. Therefore a method is needed, where the Maxwell's equation is solved with a fast oscillating optical field and where the time dependence of the propagating field is included. Such an approach is provided by the finite difference time domain (FDTD) method, which was developed by Yee [42]. A detailed overview on the important equation and their discretisation is given in [39].
In this method the derivative with respect to the time ($\partial/\partial t$) is not replaced by the expression $i\omega$. In other words, the fast oscillating field is considered in the simulation with the consequence, that a denser mesh has to be chosen in the discretization. The space between two mesh points should not be larger then $\lambda/(10n)$, where λ is the wavelength and n is the refractive index.
The dense mesh leads to a relatively large memory demand and a slow time evolution in the simulation. Consequently, for large waveguide structures the simulation time increases to several hours or even days. Three dimensional problems can only be solved for very small structures.
An FDTD-simulation starts with a given field distribution in the simulation area at the time t = 0. Then the evolution of the field distribution with the time is calculated in time steps Δt. This procedures allows simulating structures with feedback, where the time information in the optical field is important.

3.3. The finite element method (FEM)

Femlab is quite a powerful computer program that allows solving almost any partial differential equation (PDE). The simulations are carried out using the finite element method (FEM). The FEM can be used for the simulation of any waveguide structure. However, a limitation is generally given by the access memory of the used computer or at some point even by the program itself. If the fast oscillating field is considered in the simulation (equivalent to the FDTD-method), only very small structures can be simulated. For longer waveguide structures (some millimeters) the slowly

varying amplitude approximation must be used as in the BPM. Nevertheless the FEM is still suitable for the simulation of bends or Y-splitter with large opening angles. The direction of light propagation does not necessarily be paraxial as with the BPM. The only limitation arising from the slowly varying amplitude approximation is present at abrupt changes of the waveguide structures which is generally avoided anyway in the designs.
In the finite element method the wave equation is transformed into a the functional

$$I = \frac{1}{2}\iint_{\Omega}\left\{\left(\frac{\partial E}{\partial x}\right)^2 + \left(\frac{\partial E}{\partial y}\right)^2 + \left(k_0^2 n^2 - \beta^2\right)E\right\}dxdy - \int_{\Gamma} E\frac{\partial E}{\partial s}d\Gamma \qquad (3\text{-}11)$$

where Ω is the simulation area, Γ the boundary of this area and $\partial/\partial s$ is the derivative with respect to the normal vector **s**.
Solving the wave equation is equivalent to solving the variational problem

$$\delta I = 0\,. \qquad (3\text{-}12)$$

Using the FEM, the simulation area is divided into numerous segments, generally triangles. The variational problem is now solved for each segment based on the relation

$$\delta I = \sum_e \delta I_e \quad (e\text{: number of segment}). \qquad (3\text{-}13)$$

In a segment the optical field E_e is expanded as

$$E_e = \sum_i N_i E_{ei} \quad (i\text{: number of function}) \qquad (3\text{-}14)$$

N_i represents a set of basis function that approximates the real optical field. E_{ei} are the expansion coefficients in segment e. Inserting this expansion into the functional I a eigenvalue problem represented by

$$\begin{aligned}\left(A - \lambda^2 B\right)E &= 0\\ \lambda^2 &= k_0^2 n^2 - \beta^2\end{aligned} \qquad (3\text{-}15)$$

is obtained and can be solved [40].

Using Femlab for integrated optic simulations the choice of the PDE and its coefficient is very important. Solving the Maxwell's equation needs a very fine segmentation. The thereof demanded memory is immense. Therefore, for larger waveguide structures it is more efficient to use the slowly varying amplitude approximation as used in the BPM.

3.4. Comparison of simulation methods

Categorizing the three methods with respect to the need of computing power, BPM is the fastest, FDTD the slowest and FEM the most memory demanding method. APSS providing BPM and FDTD simulations is much more user friendly than Femlab. However, Femlab has the almost unique property of providing the combination of the simulation of different physical models. Therefore Femlab is a good tool for simulating thermo-optic devices, where the optical field propagation depends on the temperature distribution caused by a heater (see chapter 5.2.2).
Table 3-1 gives an overview of the advantages, disadvantages and application fields of the here discussed simulation methods.

	advantages	**disadvantages**	**applications**
BPM	short simulation times	only for paraxial problems, no reflections/feedbacks considered	Y-splitter, S-bend, adiabatic taper
FDTD	time dependence: reflections/feedbacks considered	time consuming simulations	bends, fast altering structures, resonators
FEM (with Femlab)	versatile usage: problem specific definition of PDE to be solved, combination with thermal simulation	needs large random access memory for simulations	thermo-optic devices

Table 3-1: Comparison of the simulation methods BPM, FDTD and FEM.

4. Polymer optical waveguides

4.1. Polymer materials for integrated optics

As previously mentioned polymer materials build a promising platform for the fabrication of integrated optical devices. Development in optical polymer waveguide materials over the last years has been focused on reducing absorption loss in the C-band (1525-1565nm) and the L-band (1565-1625nm). Fig. 4-1 shows the reduction of the propagation loss in single-mode waveguides achieved with different materials. In addition to the optical loss reduction the environmental stability of the polymer materials was improved in the last years.

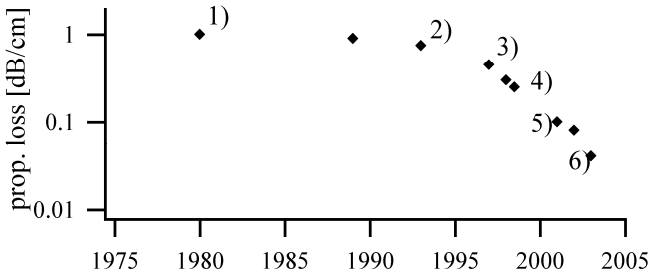

Fig. 4-1: Reduction of propagation loss at 1550nm in single-mode waveguides over the last 30 years [43]. The corresponding materials are: 1) acrylates, 2) fluorinated polycarbonate, 3) fluorinated polyimides, 4) perfluorocyclobutene, 5) fluorinated acrylates, 6) perfluoropolymers.

The most important development for the reduction of optical loss in waveguides is the fluorination of the polymer materials. Non fluorinated polymers have many C-H and O-H bonds. The excitation of vibrational overtones of these bonds causes a dominant part of the material absorption for the usual telecom wavelengths around 1550nm and 1300nm. By replacing the light hydrogen atoms by fluorine, the reduced mass increases and the vibrational resonance is shifted to longer wavelengths in the infrared. As listed in Table 4-1, there are also undesired overtones of C-F

bonds near the used wavelengths, but the resulting absorption is very small.

Fig. 4-2 shows the transmission spectrum of a 10µm thick layer consisting of a fluorinated acrylate provided by ZenPhotonics. The transmission spectrum was measured with Perkin Elmer Lambda 19 spectrometer. The strong absorption below 450nm is due to electronic excitations and is typical for polymer materials. Obviously, small absorption bands in the infrared cannot be detected in a transmission measurement through a 10µm thick layer. The absorption coefficient needs to be at least 20dB/cm for a clear detection. For a more detailed analysis in the C-band and L-band the loss in a waveguide was measured for different wavelengths (Fig. 4-3). The loss increases for wavelengths above 1600nm. This can be explained by the absorption of the 6th vibrational overtone of the C-F bond at 1626nm.

bond	**overtone order**	**resonant wavelength [nm]**	**absorption relative to 1st order of C-H bond**
C-H	1	3390	1
C-H	2	1729	$7.2 \cdot 10^{-2}$
C-H	3	1176	$6.8 \cdot 10^{-3}$
C-D	3	1541	$1.6 \cdot 10^{-3}$
C-D	4	1174	$1.3 \cdot 10^{-4}$
C-F	5	1626	$6.4 \cdot 10^{-6}$
C-F	6	1361	$1.9 \cdot 10^{-7}$
C-F	7	1171	$6.4 \cdot 10^{-9}$
C=O	3	1836	$1.2 \cdot 10^{-2}$
C=O	4	1382	$4.3 \cdot 10^{-4}$
C=O	5	1113	$1.8 \cdot 10^{-5}$
O-H	2	1438	$7.2 \cdot 10^{-2}$

Table 4-1: Wavelength of resonant absorption for different bonds due to their vibrational overtones [44].

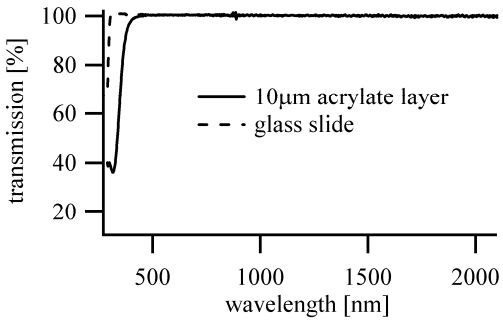

Fig. 4-2: Transmission spectrum of a layer with fluorinated acrylate of ZenPhotonics with a thickness of 10µm. The noise around the wavelength of 860nm is due to a detector change in the spectrometer.

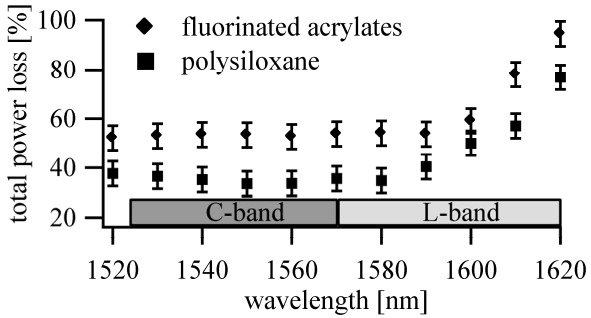

Fig. 4-3: Optical loss in a single-mode waveguide (5µm x 5µm) as a function of the wavelength. For the transmission measurement aspheric lenses were used to couple light into the waveguide and collimate light after the waveguide. The two material samples are of different length and the cannot be compared regarding the total power loss.

The choice of the polymer used in the fabrication of PLCs is crucial for the achievable results in later devices. In this work the following commercially available polymers were initially evaluated:

- Fluorinated acrylates distributed by ZenPhotonics (today ChemOptics)
- Polysiloxane distributed by RPO PTY Ltd
- Perfluorocyclobutene (PFCB) distributed by Tetramer Technologies
- Fluorinated acrylates distributed by Terahertz (THz) Photonics

For a successful fabrication of optical waveguides the material loss is not the only important parameter. The processibility and stability of the material are also significant characteristics. Table 4-2 shows an overview of the material evaluation.
First experiences with the Tetramer and THz materials showed that the effort for developing a reliable fabrication process would be large. Therefore, a specific process development (chapter 4.5) and a more detailed characterization (chapter 4.6) were only done for the RPO and the ZenPhotonics materials. Finally, due to the lower loss and particularly the better environmental stability, the fluorinated acrylates of ZenPhotonics were chosen for the fabrication of planar lightwave circuits.

	ZenPhotonics	**RPO**	**Tetramer**	**THz**
curing process	UV	UV	thermal	UV
adhesion on Si or polymer	+	+	+	-
layer quality	+	+	-	+
effort for 1st waveguide	small	small	large	large
optical loss in waveguide	0.4 dB/cm	0.7 dB/cm	not measured	0.7 dB/cm
environmental stability	+	~	not measured	not measured

Table 4-2: Evaluation of different polymers for the fabrication of optical waveguides.

4.2. Thermo-optic effect in polymers

The thermo-optic (TO) effect describes the change of the refractive index with temperature. The TO coefficient *dn/dT* of polymers is very large. It is one order of magnitude larger than in silica which is in general in competition with polymers for the use in TO devices.
In polymers the refractive index change due to a temperature change is mainly due to a change in the density ρ of the material. Therefore the TO coefficient *dn/dT* can be written as [45]

$$\frac{dn}{dT} = \left(\frac{\delta n}{\delta \rho}\right)_T \left(\frac{\delta \rho}{\delta T}\right) + \left(\frac{\delta n}{\delta T}\right)_\rho = -\left(\frac{\rho \delta n}{\delta \rho}\right)_T \gamma + \left(\frac{\delta n}{\delta T}\right)_\rho \qquad (4\text{-}1)$$
$$\gamma = \frac{1}{\rho}\left(\frac{\delta \rho}{\delta T}\right) .$$

where γ is the coefficient of volume expansion. For most polymers the following assumption gives a good approximation:

$$\gamma \approx -10^{-4}\ \mathrm{K}^{-1}$$
$$\left(\frac{\rho \delta n}{\delta \rho}\right)_T \approx 0.5 \qquad (4\text{-}2)$$

The thermal change of the refractive index at constant density is small with typical values of 10^{-6}-10^{-5} [45]. Hence, the TO coefficient is predominantly based on the density change and consequently negative:

$$\frac{dn}{dT} \approx -\left(\frac{\rho \delta n}{\delta \rho}\right)_T \gamma \approx -10^{-4}\ \mathrm{K}^{-1} \qquad (4\text{-}3)$$

In the temperature range, where TO device are operated in, the TO coefficient is constant. The estimation for the TO coefficient in equation (4-3) is close to the measured value for the ZenPhotonics polymer of dn/dT = -2.5 x 10^{-4} (see chapter 4.3.1) and is approximately one order of magnitude larger than the TO coefficient in silica (dn/dT = 10^{-5}).

4.3. Material characterization

For the design of planar lightwave circuits it is important to know certain characteristics of the used material. In passive devices a precise knowledge about the refractive index is fundamental, whereas in thermo-optic devices also the thermo-optic coefficient *dn/dT*, the thermal conductivity, the heat capacity and the relative density are important quantities.
The heat capacity of most polymers can be estimated as 1200 $\mathrm{Jkg^{-1}K^{-1}}$ and the density as 1200$\mathrm{kg/m^3}$ [45]. However, the refractive index, its temperature dependence (thermo-optic coefficient) and the thermal conductivity

depend on the chosen material. For the simulation of optical devices, particularly the knowledge about the refractive index and its temperature dependence is important. The other parameters mentioned above mainly influence the time evolution of the temperature change as well as the exact needed heating power to achieve the needed steady-state temperature distribution. These characteristics however have no direct impact on the light propagation in the thermo-optic device.

4.3.1. Refractive index measurement

There are various techniques for measuring the refractive index of a material in thin layers, such as a resonance measurement in a cavity or a measurement of the coupling angle into a planar waveguide structure. The index difference between core and cladding of polymer channel waveguides is usually around 0.01. Therefore, to clearly distinguish between the two involved materials the accuracy of the index measurement should at least be in the third digit of the refractive index. Here, an index measurement is discussed which is based on grating assisted coupling into a planar waveguide and which yields the required resolution.

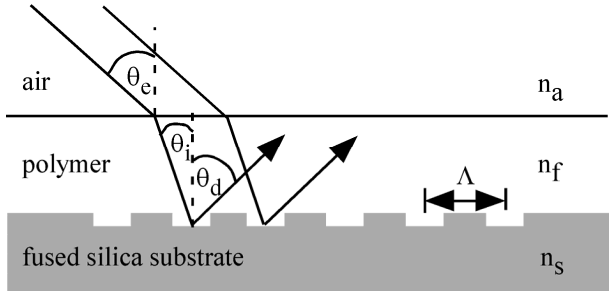

Fig. 4-4: Planar polymer waveguide with a grating in the substrate. The coupling angle θ_e depends on the refractive indices of the structure and the period of the grating. The given parameters are: n_a = 1, n_s = 1.444 (@ 1550nm), Λ = 2μm.

Measurement principle

The measurement is based on a structure as depicted in Fig. 4-4. A planar waveguide is formed with a polymer layer spin-coated on a fused silica substrate. A grating with period Λ = 2μm and a depth of 0.5μm is previously etched into the substrate.

Light couples into the planar waveguide if the following relation is fulfilled:

$$\Lambda\left(\sin(\theta_d)-\sin(\theta_i)\right)=m\frac{\lambda}{n_f} \qquad m=\pm1,\pm2,... \qquad (4\text{-}4)$$

m is the diffraction order of the grating and n_f the refractive index of the investigated polymer film. For a negative m the light is coupled backward into the waveguide, for a positive m light is coupled forward (as shown in Fig. 4-4). θ_i and θ_e are connected to each other via the Snell's law. With n_{eff} being the effective index of the guided mode in the waveguide, the above equation can be written as

$$n_f\left(\sin(\theta_d)-\sin(\theta_i)\right)=n_{eff}-n_f\sin(\theta_e)=\frac{\lambda}{\Lambda}m \qquad m=\pm1,... \quad (4\text{-}5)$$

The effective index in a slab waveguide is given by

$$2k_0d\sqrt{n_f^{\,2}-n_{eff}^{\,2}}-\varphi_{fs}-\varphi_{fc}=2\pi m' \qquad m'=0,1,... \qquad (4\text{-}6)$$

where m' stands for the number of the mode. φ_{fs} and φ_{fc} take account of the phase shift at the top and bottom interface of the waveguide.
In the experiment the sample with the grating couple is rotated on a high precision rotation motor with an angle resolution of 0.001° (Fig. 4-5). When the incident angle of the laser beam corresponds to the coupling angel of the grating coupler a signal is detected on the photodiode at the edge of the waveguide. The photodiode is placed at the output side of the planar waveguide to provide a measurement compared to a zero signal. This enables a measurement of the coupling angle also for small coupling efficiencies. The measurement is done with TE and TM polarization.
The refractive index of the film can then be deduced using the measured coupling angle θ_e and the equations above. When the temperature of the measured sample is changed for a subsequent measurement the coupling angle is shifted and a different refractive index is deduced. By repeating the measurement at multiple temperatures the thermo-optic coefficient *dn/dT* can be deduced.
The coupling efficiency depends on the exact geometry (depth, shape, aspect ratio: line width to grating period) of the grating [47]. The measurements showed that with our geometry the coupling efficiency is larger for higher order modes (Fig. 4-6). This may be explained by the fact that

higher order modes have larger field intensity at the polymer to substrate interfaces. Therefore the grating has a higher influence on these modes.

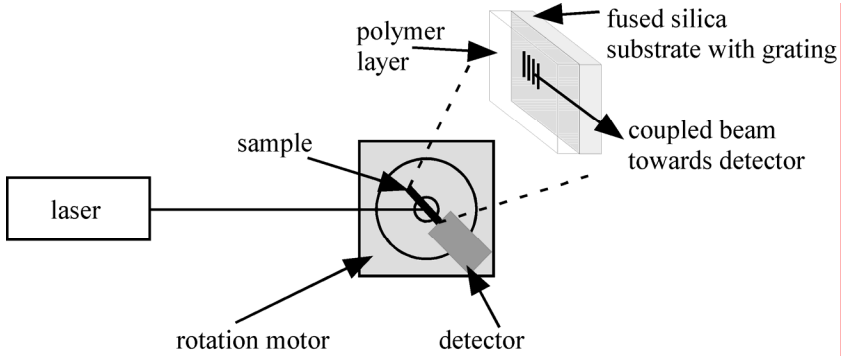

Fig. 4-5: Setup for the refractive index measurement. The sample is placed on a rotation motor and a signal is detected when the incident angle of the laser beam corresponds to the coupling angle of the grating coupler.

For the measurement of the coupling angle, the sample is placed on a rotation motor. The resolution of the rotation motor is 0.001° and the resulting error of the deduced refractive index is 0.002. Other sources of measurement errors, like the thermal expansion of the substrate and the polymer film or the inaccuracy of the grating period (~ 5nm) are smaller and can be neglected.

Results

The measurements were carried out with the fluorinated acrylates of ZenPhotonics as well as with the polysiloxane of RPO. The material set of ZenPhotonics consists of three materials Zen450, Zen460 and Zen470, where Zen460 is a mixture of the other two polymers. RPO has two polymers for the core and the cladding of the waveguide, respectively. It was found for all polymers that the birefringence was smaller than the accuracy of the measurement.
From measurement curves as the one shown in Fig. 4-6 the refractive indices listed in Table 4-3 were deduced. A repetition of the measurement at different temperatures was then carried out. As explained in chapter 4.2 the refractive index decreases linearly with the temperature (Fig. 4-7 and Fig. 4-8). At a certain temperature the refractive index of the polymer is lower than the refractive index of the fused silica substrate. At this point no mode is guided and accordingly no coupling is observed. This effect

limits the number of data points particularly for the lower index polymers Zen450 and RPO clad.

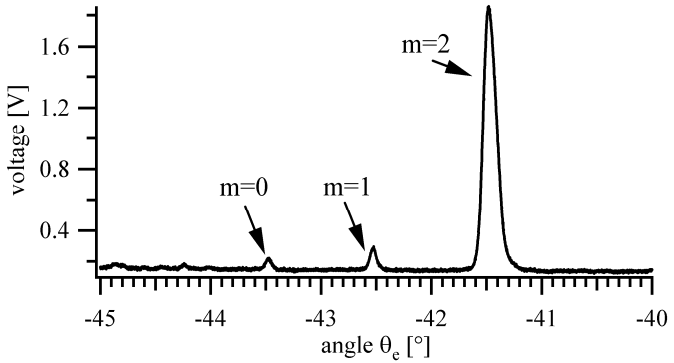

Fig. 4-6: Output intensity measured with a photodiode at the output of the planar waveguide during the rotation of the sample. We see that the higher order modes have a larger coupling efficiency.

	refractive index @ 1550nm and 20°C	**thermo-optic coefficient [10^{-4}]**
Zen450	1.452 ±0.002	TE: -2.82 ±0.05 TM: -2.35 ±0.05
Zen460	1.460 ±0.002	TE: -2.52 ±0.05 TM: -2.13 ±0.05
Zen470	1.470 ±0.002	TE: -2.48 ±0.05 TM: -2.07 ±0.05
RPO core	1.503 ±0.002	TE: -2.95 ±0.03 TM: -3.06 ±0.03
RPO clad	1.491 ±0.002	TE: -3.03 ±0.03 TM: -3.06 ±0.03

Table 4-3: Refractive index and thermo-optic coefficient of the evaluated polymers.

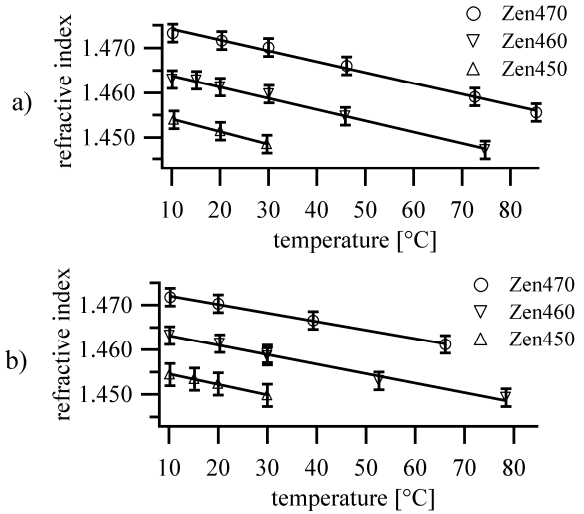

Fig. 4-7: Temperature dependence of the refractive index of the Zen-Photonics polymers. a) TE polarization, b) TM polarization

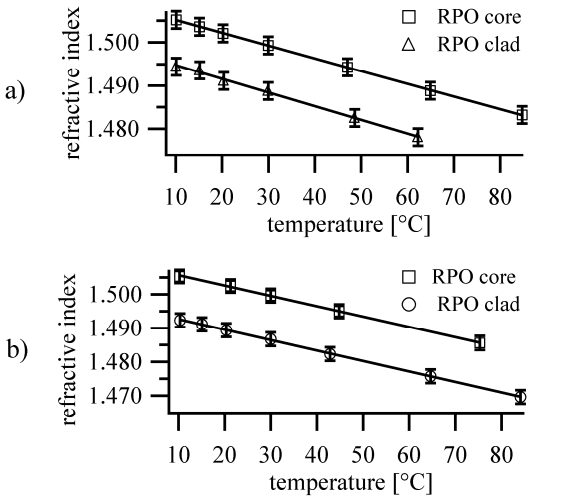

Fig. 4-8 Temperature dependence of the refractive index of the RPO polymers. a) TE polarization, b) TM polarization

Fitting a line through the measured data points the thermo-optic coefficient *dn/dT* can be deduced. The obtained values are also listed in Table 4-3. As a comparison, the thermo-optic coefficient of silica is around 10^{-5} and therefore more than one order of magnitude smaller than the thermo-optic coefficient of the evaluated polymers.
A large thermo-optic coefficient is obviously not always desired. The performance of passive devices, for instance, should not change with temperature. But as the refractive indices of the core and the cladding material shift in parallel, the impact of a homogeneous temperature change on a passive device is also small with polymer materials. In thermo-optic devices, however, the large thermo-optic coefficient reduces the consumed electrical power by at least one order of magnitude to some tens of mW (see chapter 5.2).

4.3.2. Measurement of thermal conductivity

The thermal conductivity λ influences the dynamics and the needed heating power of a thermo-optical device:

- The response time of a thermo-optic device is faster for a larger thermal conductivity: $\tau \propto 1/\lambda$
- The heating power needed to induce a certain temperature rise ΔT is smaller for a smaller thermal conductivity: $\Delta T \propto 1/\lambda$

Both criteria, a fast response as well as a low heating power, are favorable for a thermo-optic device. But the criteria have a contrary trend for an increasing thermal conductivity. Therefore a compromise must be found. The response dynamics only have to satisfy the specifications for a certain application. As an example, the thermal conductivity of silica is almost one order of magnitude larger than the thermal conductivity of polymers (λ_{silica} = 1.38W/mK). However, sufficiently short response times for routing applications (some ms) can also be achieved with polymers (see chapter 5.2). In this case, the specifications can be fulfilled and the advantage of a lower heating power is more important than the drawback of a slower response. This discussion shows that the thermal conductivity is an interesting parameter.

Measurement setup

Most techniques to measure the thermal conductivity rely on bulk samples and are not applicable to thin films. The physical properties of a thin film

should be measured as processed, because the extrapolation from a bulk measurement to the film can be misleading. A bulk sample of a polymer can differ significantly from a thin film obtained for example by spin-coating.
Fig. 4-9 shows the experimental setup for the thin film measurement. The polymer was spin-coated on a silicon wafer and placed on a copper plate that was kept at a constant temperature T_{base}. A copper coil was slightly pressed onto the polymer layer with heat conducting paste in between. The coil was heated with a tightly winded electrical wire. The whole setup was place inside a plastic hood in order to minimize influences from the environment.

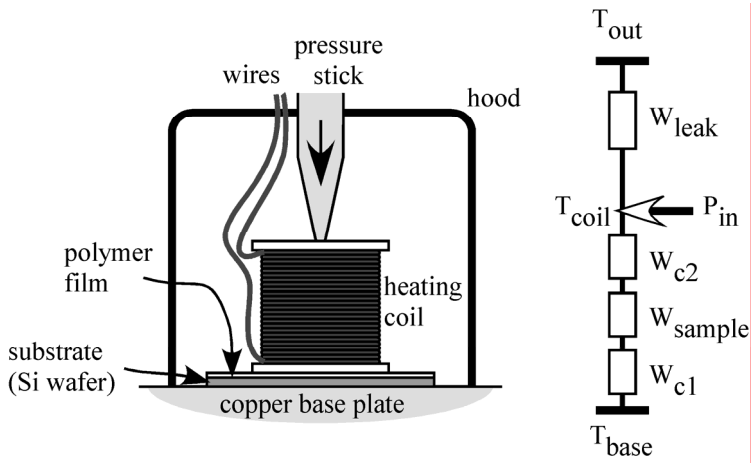

Fig. 4-9: Experimental setup for thin film measurement of the thermal conductivity.

Measurement principle

On the right hand side of Fig. 4-9 the basic idea of the measurement is depicted. W_{c1} is the thermal resistance from the polymer layer down to the copper base plate. W_{c2} is the thermal resistance of the contact between the coil and the polymer layer. W_{sample} stands for the thermal resistance of the measured sample and W_{leak} summarizes the influence of the environment, e.g. the pressure stick, the electric wires and the surrounding hood. In the measurement setup it can be assumed that

$$W_{leak} >> W_s = W_{c1} + W_{sample} + W_{c2} \qquad (4\text{-}7)$$

where W_s is the total thermal resistance between the heating coil and the base plate.
T_{coil} is the measured temperature inside the coil and T_{out} refers to the temperature of the environment of the setup. Knowing the electrical resistivity of the winded wire, the heating power P_{in} can be deduced by measuring the electrical resistance R and the electrical current I:

$$P_{in} = I \cdot R^2 \tag{4-8}$$

For the measurement of the thermal conductivity, the base plate is first brought to a stabilized temperature T_{base} without applying a heating power P_{in}. Consequently a constant heating power P_{base} is flowing through the whole system that can be considered as a serial assembly of thermal resistances. The following relation is valid:

$$P_{base} = \frac{T_{coil}^{(0)} - T_{base}}{W_s} = \frac{T_{out} - T_{base}}{W_s + W_{leak}} \tag{4-9}$$

The superscript $^{(0)}$ refers to the zero heating power $P_{in} = 0$.
If a heating power $P_{in} \neq 0$ is applied, the power flow is described by

$$\begin{aligned} P_{in} &= P_{upwards} + P_{downwards} \\ &= \frac{T_{coil} - T_{out}}{W_{leak}} + \frac{T_{coil} - T_{base}}{W_s} \end{aligned} \tag{4-10}$$

which is similar to a parallel assembly of thermal resistances. The subscripts *upwards* and *downwards* are in relation with Fig. 4-9.
Apart from the actual variable W_s that includes the wanted thermal conductivity of the sample, there are the two unknown parameters W_{leak} and T_{out}. When $T_{coil}^{(0)}$ was measured, W_{leak} could be determined with equation (4-9). But, as it is difficult to determine the temperature of the plastic hood, it is better to make use of the approximation (4-7). Solving equation (4-9) for T_{out} and inserting the expression in (4-10), one gets

$$P_{in} = \left(T_{coil} - T_{coil}^{(0)}\right) \frac{W_{leak} + W_s}{W_{leak} W_s}. \tag{4-11}$$

Using the approximation (4-7), the expression is simplified to

$$P_{in} \cong \frac{T_{coil} - T_{coil}^{(0)}}{W_s} \tag{4-12}$$

which results in

$$W_s \cong \frac{T_{coil} - T_{coil}^{(0)}}{P_{in}}. \tag{4-13}$$

The thermal resistance W_s can also be written as

$$W_s = \left(W_{c1} + W_{c2}\right) + W_{sample} = W_c + \frac{d}{F\lambda} \tag{4-14}$$

where d is the thickness of the sample and F is the cross-section of the heat flow. If multiple samples of the same material but different thickness d are measured, the thermal resistance W_s can be plotted as a function of the thickness d. The slope of this plot is given by $1/F\lambda$, from which λ can finally be deduced.
Fig. 4-10 summarizes the procedure of the measurement. If this procedure is repeated for different base temperatures, the temperature dependence of the thermal conductivity can also be deduced.
The statistical error from the evaluation of the thermal resistance versus thickness is relatively small. But there are larger systematic errors in the measurement. After changing a sample in order to vary the thickness of the sample, the thermal contacts in the setups can change. Additionally it is assumed that T_{out} remains constant during the measurement, which is not necessarily true. Overall, we expect a total error of the measurement of 5 to 10%.

Results

To assess the validity of the technique, test measurements were carried out on thin glass samples with known thermal conductivity. As these samples should be as thin as possible Schott D263 glass for flat panel display with thickness 150 µm, 220 µm, 305 µm, and 405 µm were selected. For all samples the base temperature was stepped from 15 °C to 60 °C with an increment of 5 °C. The obtained data series were analyzed as described above and lead to the thermal conductivities shown in Fig. 4-11. The dashed line in Fig. 4-11 indicates the literature value which differs about 5% from our experiment and lies clearly in our expected error band.

The slope of the measured thermal conductivity versus temperature is $1.84 \cdot 10^{-3}$ W/mK^2 comparing fairly well with the $1.7 \cdot 10^{-3}$ W/mK^2 from literature. The statistical error $\pm 0.05 \cdot 10^{-3}$ W/mK^2 from the data analysis is too small. An error estimation including systematical errors is giving the right range of accuracy.

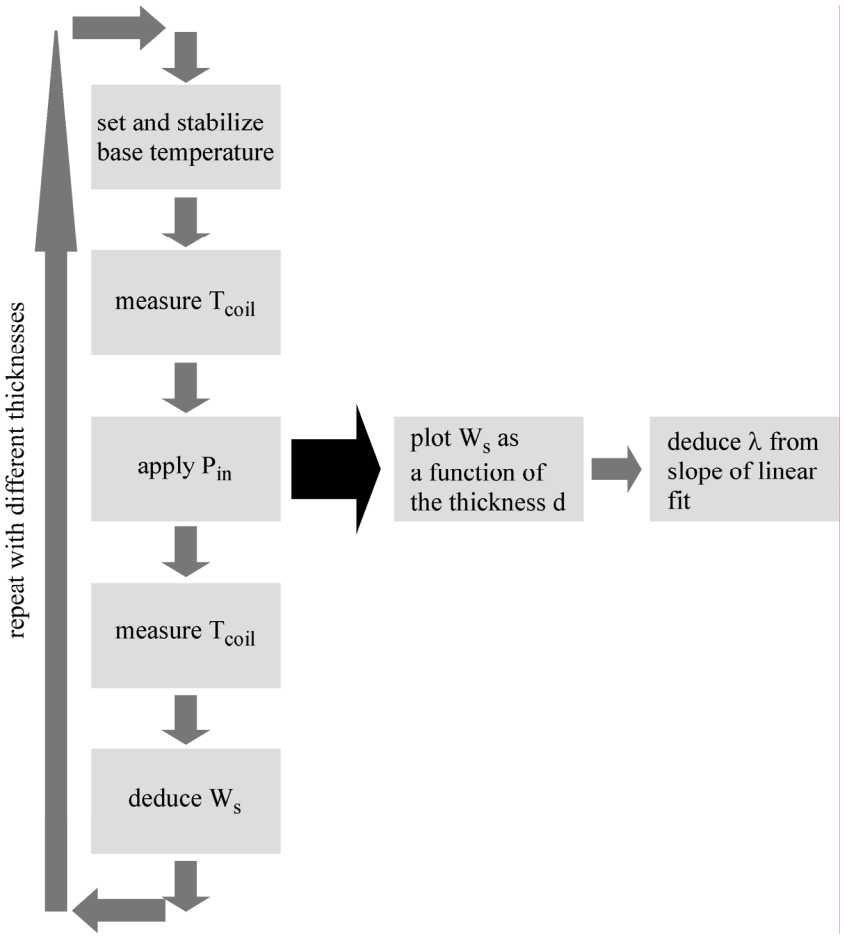

Fig. 4-10: Procedure for the measurement of the thermal conductivity in a thin film.

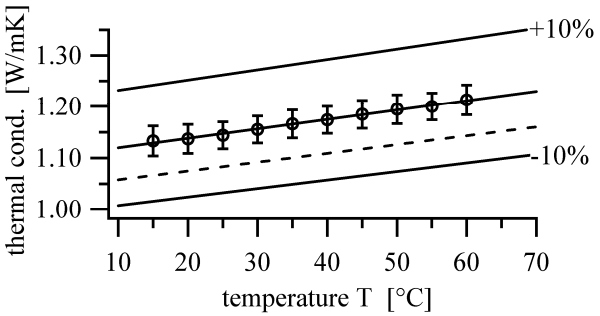

Fig. 4-11: Test measurement with thin glass plates: The dashed line represents values from literature. The error bars are statistical errors from the evaluation of the thermal resistance versus sample thickness. The lines ±10% indicate the estimated error band from the measured values.

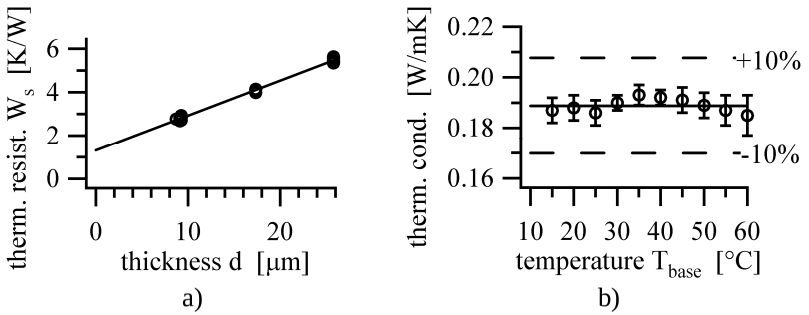

Fig. 4-12: a) Total thermal resistance W_s as a function of the polymer layer thickness. The values correspond to a temperature base temperature of 30°C. The deduced parameters are: slope = 0.161±0.003 K/µmW, λ = 0.199±0.004 W/mK, W_c = 1.32±0.05 K/W. b) Measured thermal conductivity versus base temperature for the ZenPhotonics polymer. The polymer has a constant thermal conductivity over the whole measured temperature interval. The average value is λ = 0.19±0.02 W/mK.

For the measurement on polymer samples we used the ZenPhotonics polymer Zen450. Polymer layers from 8µm to 26µm were investigated. The thermal conductivity experiment is again carried out between 15°C and 60°C in 5°C steps. Fig. 4-12a) shows the data evaluation at 30°C.
The resulting values for the thermal conductivity of the polymer films at different base temperature are shown in Fig. 4-12b). No significant de-

pendence of the thermal conductivity on temperature can be observed. The average value of λ = 0.19±0.02 W/mK, with an error bar of 10% assumed, is comparable to other polymers of similar structure.

4.4. Waveguide design

In a first step we structured straight waveguides with our polymer materials. Based on these waveguide structures PLCs were designed and fabricated at a later stage. A cross-section of such a channel waveguide is shown in Fig. 4-13. With the chosen refractive index contrast of 0.01 the single-mode condition for a quadratic channel waveguide of dimension *h x h* is given by

$$V = k_0 \frac{h}{2}\sqrt{n_{co}^2 - n_{cl}^2} = 2.136 \qquad (4\text{-}15)$$

and leads to a maximum value of $h < 6.15\mu m$. Waveguide dimensions of 5µm x 5µm were used for this work. With these dimensions the guided mode is relatively well matched with the mode of single-mode fibers. The quadratic shape of the waveguides guarantees the desired polarization independence.

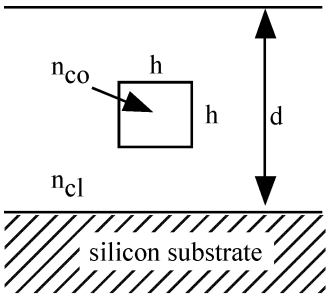

Fig. 4-13: Design of an embedded channel waveguide. The refractive index contrast is n_{co} - n_{cl} = 0.01. The geometrical dimensions are h = 5µm and $d \approx 25\mu m$.

The cladding layer between the core and the substrate needs to be sufficiently thick to prevent the light from coupling down into the substrate. In the here considered designs this thickness is chosen to be 10µm.

4.5. Waveguide fabrication

There are various techniques for the fabrication of waveguide structures in polymers. The most standard technology uses reactive ion etching. However, an important advantage of polymer materials is that there are faster techniques that allow an efficient and cheap production of PLCs as previously mentioned. As one of these techniques, direct UV-printing (or sometimes also called direct lithography) was established in this work.

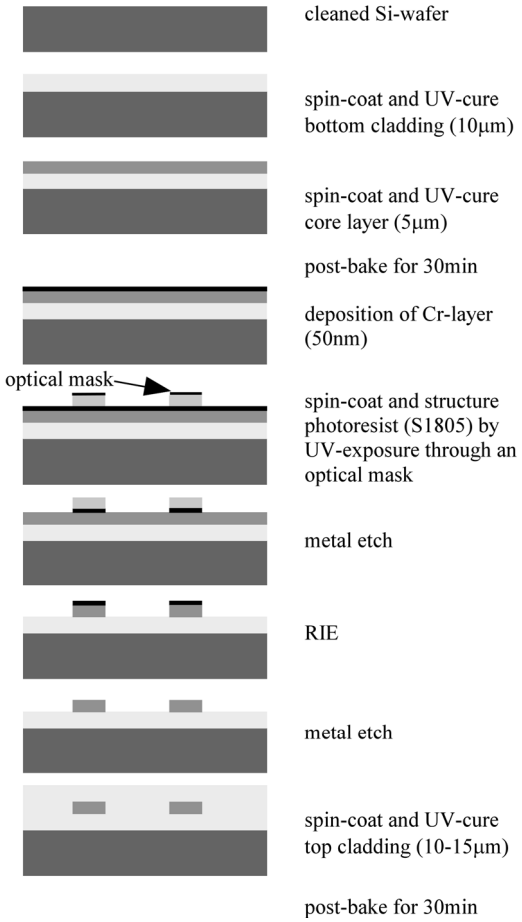

Fig. 4-14: Process steps for waveguide fabrication with RIE: The process is relatively long. It takes approximately one working day to go through all these steps.

4.5.1. Reactive ion etching

The advantage of reactive ion etching (RIE) is that the process can be used with almost any polymer material. Once polymer layers of good quality are achieved with a material, waveguide structures with good optical quality can be etched.

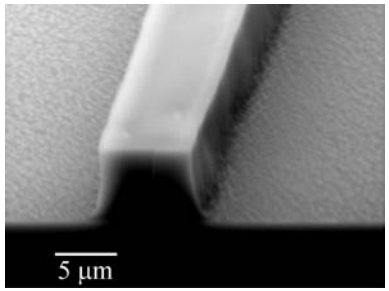

Fig. 4-15: Scanning electron microscope picture of a 5µm x 5µm waveguide fabricated with RIE (without top cladding). A desired quadratic waveguide shape is obtained, but there is also a clearly visible sidewall roughness.

The critical parameters in the etch process are the pressure in the etching chamber, the gas flow of the etching gas and the radio frequency (RF) power of the plasma etching machine.
O_2 is generally used as etching gas and different metal layers like chromium, aluminum or gold can serve as etch mask. The etch parameters influence the etching rate and the smoothness of the etched sidewalls. Higher RF power results in a higher etch rate. With constant oxygen flow rate and RF power, there is a peak on the etch rate to pressure. The pressure value corresponding to the peak of the etch rate shifts to a higher pressure at higher power. The roughness of the etched sidewalls is improved with higher pressure and lower RF power. However, with higher pressure the anisotropy is inferior due to stronger chemical etching.
In this work RIE was used in order to get a first reference on the quality of the polymer waveguide consisting of the fluorinated acrylates. The process is shown in the diagram of Fig. 4-14. The etching parameters were chosen to be 100sccm (standard cubic centimeter per minute (at 1 atmosphere pressure and 0°C)) for the gas flow, 150W for the RF power and 50mtorr for the pressure. The etching rate is then approximately 1µm/min. The relative etch rate of polymer to chromium is approximately 100:1.

The process is relatively long, but the individual steps are well known and the results of reproducible quality. An advantage of this technology is the ability to fabricate waveguide structures with vertical sidewalls (Fig. 4-15). The influence of the visible sidewall roughness is reduced by the fact, that the refractive index contrast of the embedded channel waveguide is small and therefore the scattering losses are diminished.

4.5.2. Direct UV-printing

For an efficient waveguide fabrication other techniques than the RIE process are favorable. In direct UV-printing the polymer in the core layer is patterned with a UV illumination through a mask similar to a photoresist (Fig. 4-16). The number of steps is reduced to a minimum in this fabrication process and the processing time from the bare wafer to the final waveguide structures is below one hour. Obviously, a UV-curable polymer is needed for the core layer. In this work, this process was used for the waveguide fabrication with ZenPhotonics polymers as well as with RPO polymers.
The critical step is the structuring of the waveguide cores with dimensions of 5µm x 5µm. The spin-coated polymer solution contains polymer chains which crosslink during the UV-exposure. Some polymer solutions also consist of monomers, which polymerize when exposed to UV light. For structuring waveguides in such a polymer layer a mask is needed. The incident UV-light only passes the mask at the regions where the waveguide cores need to be formed. Beside the waveguide cores the transmission of the UV-light has to be inhibited. Therefore a negative mask is used.
As the presence of oxygen suppresses the cross-linking, a nitrogen atmosphere has to be introduced between the wafer and the mask. Finally, unlike well known photoresists, the polymers used for the waveguide fabrication can not be dried with a soft-bake previous to the UV-exposure. Therefore, the polymer layer and the mask should not be brought into contact in the mask aligner as the wet polymer would stick to the mask. To avoid sticking, a minimum gap of 10-15µm should be maintained during the illumination.
Respecting these parameters, waveguides of the desired dimensions can be structured. But the fact that the mask and the wafer are not in contact has its influence on the waveguide shape. The small gap between the mask and the polymer film causes diffraction of the UV-light. Fig. 4-17 shows the distribution of the UV intensity on the wafer for a gap of 10µm

and a monochromatic light source. In the simulation the Fourier transformation is of the light pattern at the mask is propagated through free space. An inverse Fourier transformation then gives the intensity profile on the polymer layer. This intensity profile caused by the UV-lamp of a mask-aligner would certainly be smoother. As the final waveguide shape roughly corresponds to the intensity distribution of the incident UV-light, it is clear, that with this procedure rectangular waveguides are difficult to be obtained. Depending on the sensitivity of the photo-initiator that induces the cross-linking in the polymer, the obtained waveguides are of a more or less broad tunnel-like shape corresponding to the intensity distribution of the incident UV-light.
The polysiloxane of RPO were initially designed for the use with direct UV-printing, whereas the fluorinated acrylates of ZenPhotonics were not developed for this process. Both polymers are very sensitive to UV-light and the cross-linking is induced with a relatively small dose of 250mJ/cm^2. The obtained waveguide shape is more tunnel-like than rectangular (Fig. 4-18). The depicted waveguides should have a cross-section of 5µm x 5µm. The height of the waveguide has the desired dimension, but the widths are clearly enlarged.

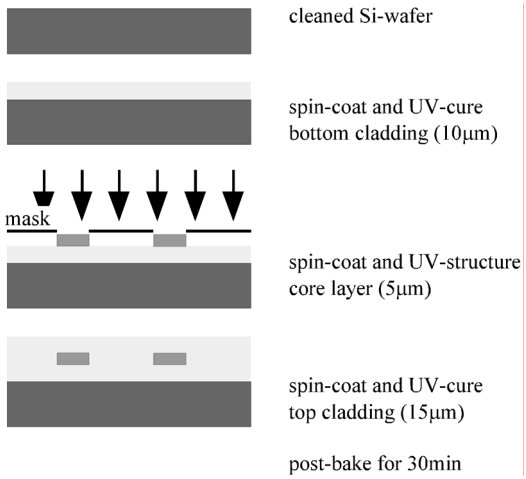

Fig. 4-16: Process steps for waveguide fabrication using direct UV-printing: The number of steps is significantly reduced and the processing time is only 1 hour.

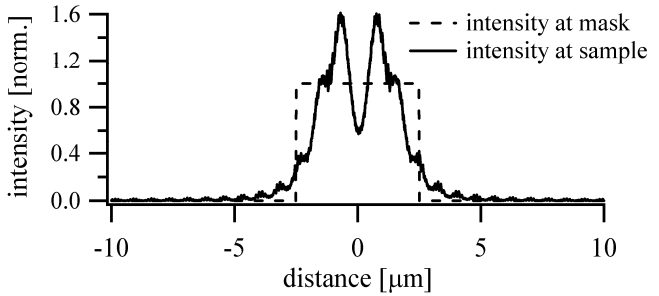

Fig. 4-17: Intensity distribution of the UV-light (monochromatic: λ = 365nm) with a gap of 10µm between mask and wafer. The illuminated structure corresponding to the waveguide core has a width of 5µm. The dashed line shows the normalized intensity distribution right after the mask.

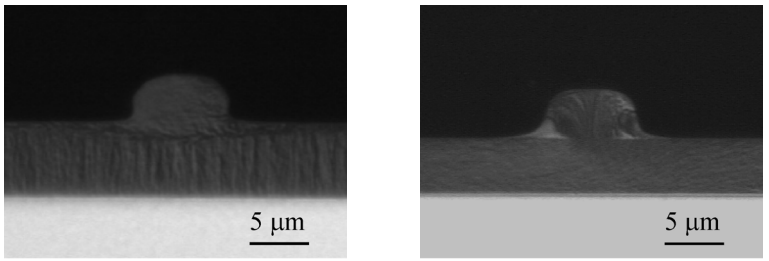

Fig. 4-18: Waveguide shape obtained with direct UV-printing (without top cladding). a) RPO waveguide, b) ZenPhotonics waveguide.

Obviously, a UV-exposure with a gap between the wafer and the mask is not optimal for defining small structures such as single-mode waveguides. It is essential that the structures on the mask are perfectly transformed into the polymer layer. An undesired deviation from the rectangular waveguide shape does not affect the propagation loss in the waveguide, but the waveguide structure becomes polarization sensitive. Additionally, the performance of waveguide structures like bends, splitters or couplers would be negatively affected.
The ability to contact the wafer with the mask during the UV-exposure would ensure an optimized intensity distribution in the polymer layer. Therefore, the surface properties of the mask and the polymer layer were modified. On the mask a layer of Teflon lowers the surface energy and therefore lowers the risk of sticking to the wafer. Additionally, the poly-

mer layer can be pretreated with a soft-bake. Although this soft-bake does not lead to a dry polymer layer, the surface properties slightly change. Including these steps in the process, the wafer was brought into contact with the mask in the mask-aligner and the wafer could be released after the exposure. Unfortunately, this process is not very reproducible. It depends on parameters like the age of the polymer or the environment in the clean-room. Therefore, it was not possible to establish a reproducible process. Nevertheless, the quality of the waveguide shape could be improved and quadratic waveguide cores of the desired dimensions were achieved (Fig. 4-19).
Obviously, it is desirable to have a polymer material that has the same processing properties like a photoresist and can be dried properly with a soft-bake. First experiments with a polymer based on methacrylate, that has not been optimized for low propagation loss yet showed, that with such a material almost rectangular waveguides with a high aspect ratio can be structured with a high reproducibility (Fig. 4-20).

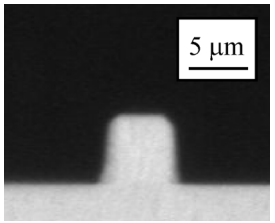

Fig. 4-19: Cross-section of single-mode waveguide (cross-section: 5µm x 5µm, without top cladding) consisting of ZenPhotonics polymers without gap between wafer and mask during the UV-exposure.

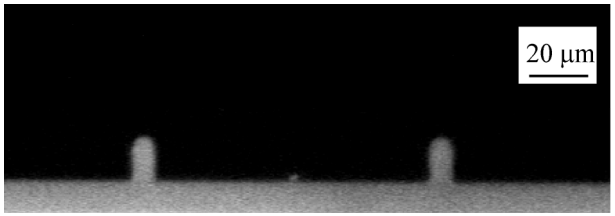

Fig. 4-20: Cross-section of waveguide core structured in a methacrylate layer (without top cladding). The core dimensions are 6µm x 8µm.

4.5.3. Cleaving of waveguide chips

The optical characterization of waveguides is mainly done by measuring the propagation loss in the waveguide and analyzing the mode profile of the guided mode. Therefore, light has to be coupled into the waveguide. For an efficient coupling it is important to guarantee nice end facets after the sample preparation.

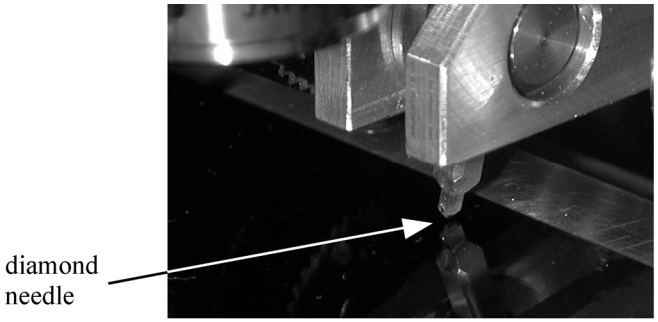

Fig. 4-21: Diamond needle of scriber that is used to induce a micro crack along a crystal plane.

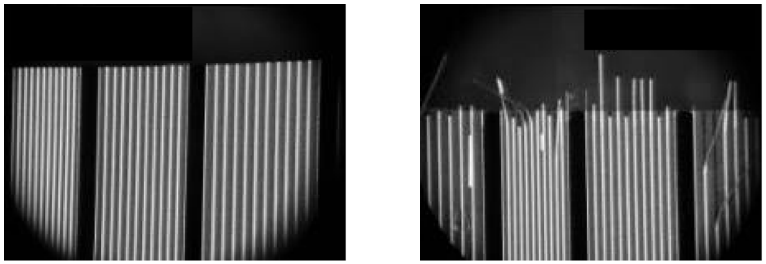

Fig. 4-22: The pictures a) and b) show three or four groups of waveguide arrays, respectively: a) Nice waveguide facets with acrylate polymer waveguides obtained with the scriber technique. b) Polycarbonate waveguides are distorted and peeled off when the wafer is cleaved.

Polymer waveguides fabricated on silicon wafers provide a very simple method for the sample preparation by cleaving the silicon wafer. With a small scratch at the edge of a piece of silicon generated with a diamond needle of a scriber, a micro crack along a crystal plane is induced. Applying a small force the wafer breaks along this predefined crystal plane. If the polymer is glassy enough, the polymer layer breaks nicely with the

substrate along the same edge. For polymers with a more rubber-like constitution, waveguide structures are distorted and the samples are not usable for coupling light into the waveguides. For samples with RPO and ZenPhotonics waveguides, however, the described technique was applicable and lead to smooth facets (Fig. 4-22).

4.6. Optical characterization of polymer waveguides

4.6.1. Waveguide mode

First of all it is important to know which modes are guided in the waveguide. The waveguides are designed to be single-mode. In multimode waveguides the light intensity couples between the different guided modes. This altered intensity distribution strongly influences the performance of a device, e.g. in bends or in coupling regions. The profile of the guided mode was measured with a beam profiler at the output of a 3cm long waveguide. Fig. 4-23 shows the good agreement with the simulated mode profile.

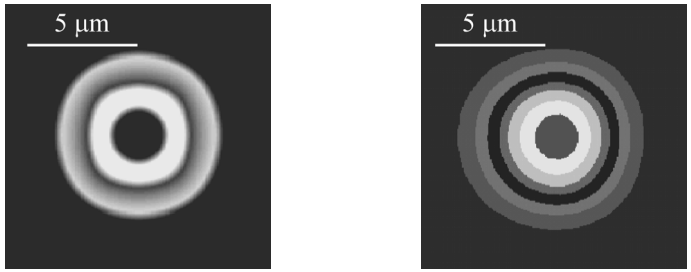

a) b)

Fig. 4-23: Mode profile of a single-mode waveguide with core dimensions of 5µm x 5µm. a) Simulated profile (field amplitude) b) Measured profile (intensity)

4.6.2. Propagation loss

As described in chapter 2.2 the optical loss of a guided mode is due to absorption, radiation and scattering. In straight waveguides the absorption and the scattering are dominant. Where the absorption is given by the material itself, the scattering loss is influenced by the quality of the fabrication process.

The total propagation loss in straight waveguides was measured with the cut-back method. With this method, the insertion loss (propagation loss + coupling loss) is measured for waveguides of different length. Assuming a constant coupling loss in the subsequent measurements with waveguides of different lengths the insertion loss, given in dB, decreases linearly with the length of the waveguide (see Fig. 4-24).

For coupling light into the waveguides, aspheric lenses were used that lead to a minimum beam diameter ($1/e^2$) of 4µm in the focus. By optimizing the position of the waveguide, the beam size is adjusted to the mode size of the waveguide and usually a coupling loss of 0.5 – 0.8 dB is achieved. The exact value depends also on the quality of the waveguide facet.

If the coupling loss is constant for the subsequent measurements, the insertion loss, given in dB, decreases linearly with the length of the waveguide. Fig. 4-24 shows an example of such a measurement with an acrylate waveguide fabricated with RIE. The data are fitted to a linear function, where the slope represents the propagation loss in dB/cm and the abscissa gives the coupling loss. In Table 4-4 the obtained propagation loss is listed for the different waveguides that were fabricated during this work.

The accuracy of the cut-back measurement depends on the number of lengths that are used for evaluating the insertion loss and the reproducibility of the coupling efficiency. In the example shown in Fig. 4-24 the accuracy of the propagation loss is 0.1dB/cm. The polarization dependence of the propagation loss is smaller than 0.1dB/cm and therefore smaller than accuracy of the measurement.

The reduced propagation loss of the UV-patterned ZenPhotonics waveguides with respect to the RIE fabricated waveguide can be explained by a reduced sidewall roughness. Additionally, the UV-patterned waveguides may have a slightly enlarged core cross-section. Consequently, the mode is better confined and the intensity at the sidewalls is smaller. This reduces the scattering loss at the surface of the waveguide core.

For the fabrication of competitive PLCs, waveguides with a propagation loss of 0.4dB/cm can be sufficient. In terms of optical loss, these waveguides can still not compete with silica waveguides (<0.1dB/cm). But in relatively short devices (~ 1 cm) the higher propagation loss is acceptable.

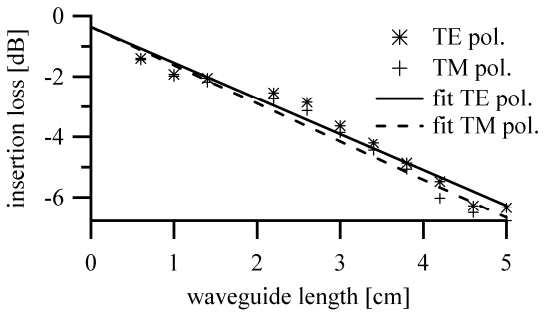

Fig. 4-24: Cut-back measurement with an acrylate waveguide fabricated with RIE. The waveguide has a core dimension of 5µm x 5µm. The insertion loss was measured for TE and TM polarization at each length.

waveguide	**propagation loss [dB/cm]**
ZenPhotonics (RIE)	0.7 ± 0.1
ZenPhotonics (UV-patterned)	0.4 ± 0.1
RPO (UV-patterned)	0.7 ± 0.1

Table 4-4: Propagation loss of evaluated waveguides.

4.6.3. Bend loss

In chapter 2.2.3 the problem of calculating bend loss has been discussed. With different approximation it was shown that bend loss starts to increase for bending radii of less than 9mm for the considered waveguide structure. On a mask with various test structures, bends with a radius of 10mm, 7.5mm and 5mm were designed.
These bend structures were again fabricated with ZenPhotonics polymers using UV-printing. As shown in Fig. 4-25, even with a bending radius of 10mm the light does hardly go around the 90°-bend and almost the whole intensity is lost.
The reason for this large bend loss can be manifold. As already mentioned in chapter 2.2.3, the bend loss is difficult to simulate for real structures with surface roughness and imperfect waveguide shapes. Therefore, a certain deviation between simulation and measurement can be expected.
However, the large bend loss also has to be brought in correlation to the waveguide quality. As the propagation loss in straight waveguides is relatively low, the surface roughness should be low and not dramatically contribute to bend loss. A more critical parameter is certainly the waveguide shape. As the UV-written waveguides are slightly larger than desired, a second mode could be excited in the region of the bend. This second mode has an effective index that is much closer to the cladding index than the effective index of the first mode. Therefore, the light in the second mode would have a much larger bend loss. An improved waveguide shape should consequently lower the bend loss.

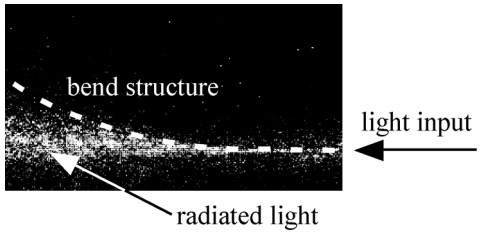

Fig. 4-25: Top-view of the waveguide chip taken with an infrared-camera: The dashed line corresponds to the course of the waveguide structure.

5. Integrated optical devices based on polymer waveguides

Based on the polymer waveguides described so far PLCs were designed and fabricated. Relying on the experience and results presented in chapter 4 with the different polymers and fabrication processes, the fluorinated acrylates of ZenPhotonics were used and the waveguides were structured with direct UV-printing.

5.1. Passive devices

As a next step, after the evaluation of straight waveguides, simple passive devices were investigated. The motivation for this investigation was based on the following points:

- The devices help to get experiences on the correlation between simulations and fabricated structures.
- The performance of a device is more sensitive to fabrication quality than a straight waveguide. Hence, a more stringent examination of the fabrication process is possible.
- The achieved results give a first comparison to generally required specifications.
- Passive power splitters and combiners are used in passive optical networks (PON). As PON's are a growing market, low cost power splitters based on polymers are potential products.

5.1.1. Power splitters / combiners

Y-splitters are the most common type of power splitters or combiners. They generally have one input and up to 16 outputs. The pitch between the outputs is standardized to either 127µm or 250µm.
The designs need to be optimized for a small insertion loss and low polarization dependence. A large opening angle in the Y-junction leads to a fast separation of the branches. Consequently shorter devices are obtained with a shorter propagation distance. On the other hand, a larger opening

angle increases the radiation loss at the junction. The trade-off consists of finding the optimal solution regarding these two effects.
In the present design, this trade off was handled by using sine-shaped S-bends to define the branches of the Y-splitter. The sine-shape allows a gentle separation of the branches at the junction. Once the modes of the two branches are separated the radius of curvature decreases and the desired pitch is achieved relatively quickly.
As already discussed in chapter 2.2.3 it is difficult to simulate bends. As the simulation results for bends were much lower than measured in real waveguides, the final insertion loss in Y-splitter is expected to be larger than obtained in simulations. Therefore, the radius of curvature or the device length, respectively, was not minimized based on simulation results. Three layouts for a 1x2 Y-splitter with different bends were chosen instead. The minimal bend radii in the three designs were 7.2mm, 16.2mm and 28.8mm, respectively. Based on these bend radii power splitters with 4, 8 and 16 outputs were designed and fabricated (Fig. 5-1).

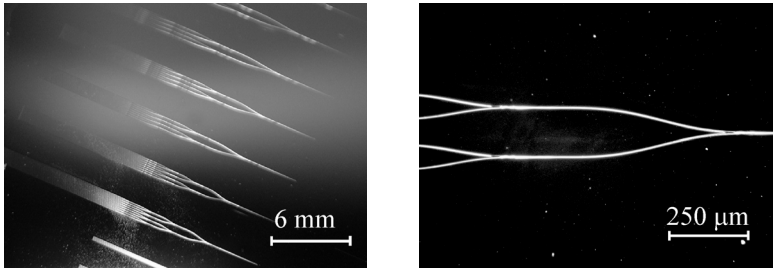

a) b)

Fig. 5-1: a) 1x16 power splitters with different bend radii. b) 1x4 power splitter.

A general specification for 1xN splitters regarding the insertion loss of these devices is given by [48]

$$IL = 0.8 + 3.4 \log_2 N \quad [\mathrm{dB}]. \tag{5-1}$$

The uniformity (maximum variation of insertion loss between input port and any two output ports) should be smaller than

$$\Delta IL \leq 0.6 \log_2 N \quad [\mathrm{dB}]. \tag{5-2}$$

The characterization of the splitters shows that the shortest devices with the tightest bends had the lowest insertion loss. This indicates that the size

of the splitters is not minimized yet and a smaller insertion loss could be achieved. Table 5-1 lists the specification deduced from the equations above and the measured insertion loss for the short splitters (R = 7.2 mm). The uniformity of the fabricated devices is clearly below 1dB and hence fulfills the specifications. As an example the intensity at the outputs of a 1x4 splitter are shown in Fig. 5-2.

splitter	**1x4**	**1x8**	**1x16**
length [mm]	10	13.5	18.5
IL [dB] (specification)	7.6	11	14.4
uniformity [dB] (specification)	1.2	1.8	2.4
IL [dB] (measured)	8.9	12.8	16
uniformity [dB] (measured)	0.2	0.4	0.7
IL of Y-splitters based on silica waveguides [dB]	< 7	< 10	< 13.5

Table 5-1: Specification of insertion loss (IL) and uniformity as well as the measured insertion loss of power splitters. The pitch between the outputs is 127µm.

The insertion loss is above the given specification. If the 3dB loss due to the splitting function at each junction of the device is subtracted from the specified insertion loss, an excess loss of 1.6dB (1x4 splitter) to 2.4dB (1x16 splitter) is acceptable. In our Y-splitters the excess loss is 2.9dB for the 1x4 splitter and 4dB for the 1x16 splitter which is around 1.5dB too high. Power splitters based on silica waveguides achieve the demanded specifications. Therefore, all of the commercial available power splitters are based on this technology.
The waveguides of the Y-splitters are fabricated with UV-printing and have by itself a relatively low loss. Considering the length of the splitters, the propagation loss takes up 0.5-1dB of the accepted excess loss. Approximately 1dB is also lost due to coupling loss at the input and the output interface. An optimization of the waveguide cross-section at the input and outputs could reduce the coupling loss by ~0.5dB. As mentioned above, a further optimization on length of the devices could also lead to a slight reduction of the propagation loss without a dramatic increase in the bend loss. Conclusively, taking these actions the desired specification could nearly be fulfilled for power splitters based on the here fabricated polymer waveguides. A longer optimization process would show whether it would possible to gain the last tenths of dB to achieve results within the specification for commercial products.

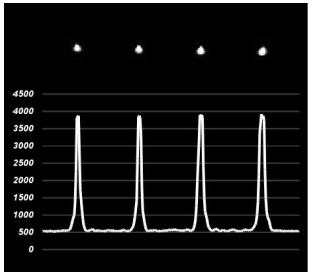

Fig. 5-2: Intensity at the outputs of a 1x4 splitter: At the top the detected image on an infrared camera is shown with the corresponding intensity of the spots below.

5.1.2. Multimode interferometers

Multimode interferometers (MMI's) are an alternative to Y-splitters. MMI's consist of one or several input and multiple output waveguides with a multimode waveguide section in between. The inputs excite multiple modes in the multimode section. Based on the self-imaging property, images of the input field are reproduced at periodic intervals [49]. With the effective index method the description of the MMI can be reduced to a one dimensional problem. Then it can be shown, that a image of the input field is reproduced after the approximate distance [26]

$$L \approx \frac{4 n_{co} W^2}{3\lambda} \quad (n_{co}\text{: refractive index of core, } W\text{: width of MMI}) . \qquad (5\text{-}3)$$

Multiple images of the input are formed at intermediate lengths. At a distance of

$$L_N = \frac{L}{N} \qquad (5\text{-}4)$$

there are *N* self-images of the input field (Fig. 5-3).
MMI's are very compact devices. In this work, two different 1x2 MMI's were devised with dimensions of

- width = 50μm, length = 1400μm
- width = 80μm, length = 3400μm

These values were obtained from simulations with the APSS software and slightly differ from the theoretical value deduced from the above approximation (equation 5-3). Following this approximation the lengths of the two MMI structures should be 1580μm and 4050μm, respectively.

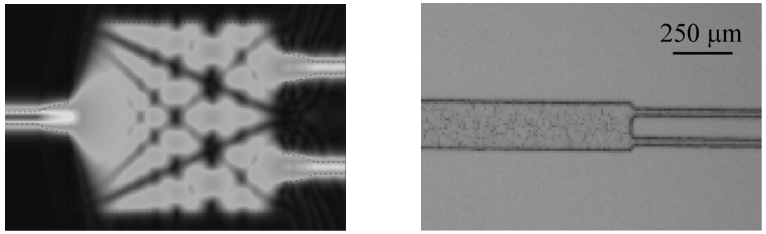

a) b)

Fig. 5-3: 1x2 MMI structure with width = 80μm and length = 3400μm. a) BPM simulation (x- and y-axis unequally scaled), b) Fabricated structure.

	long MMI	**short MMI**
Insertion loss (specification)	4.2 dB	4.2 dB
Uniformity (specification)	0.6 dB	0.6 dB
Insertion loss (measured)	6.0 dB	6.0 dB
Uniformity (measured)	<0.1 dB	<0.1 dB
Insertion loss of silica based MMIs	< 4 dB	

Table 5-2: Characterization of MMI's.

To improve the tolerance of the designed MMI's regarding their lengths, tapered output waveguides were implemented. In case that the fabricated structure does not perfectly behave as in the simulations, the light is gathered by the wide outputs and then slowly transferred to the output waveguides with single-mode width.
The specifications for these MMI's can again be deduced with the same equation as for the splitters. Table 5-2 compares the general specification with the achieved result for the two MMI layouts. The excess loss in these structures is relatively high, but the uniformity is again very good. In the inspection with a sensitive infrared-camera it is obvious that the intensity is lost at the end of the multimode section. This implies that the length of the multimode section is not optimal in the fabricated structure. BPM simulations showed that the measured excess loss is obtained, when the length of the MMI deviates 60μm from the optimized value. This corresponds to less than 3% of the length of the MMI structure. Such a small deviation between the simulation and the measurement is explainable, as the optimal length of the multimode section critically depends on the refractive index and the exact width of the fabricated structure.

5.1.3. Conclusion on passive device

At the beginning of chapter 5.1 the motivation for the design and fabrication of passive PLCs was given. Based on the results described so far, first conclusions can be drawn.

- Obviously, simulations carried out with the APSS software do not lead to optimized structures. It is hardly possible to use the simulations result for the design of bent structures and also the geometry of MMI's do not provide satisfying results.
- Considering the good uniformity of the fabricated structures and a clear allocation of the loss producing problems, the quality of the fabricated structures is good.
- At least for the Y-splitters it can be estimated that desired specification can be achieved with the used material and technology.
- For the usage of polymer based Y-splitters in PON's one has to compete with very low loss silica waveguides. The results show that more design work is needed to approach the desired specification. However, the achievement of the demanded insertion loss is possible.
- The competition of silica based power splitters is certainly strong due to the low optical losses. However, if the required specifications are

achieved with our polymer waveguides, there would be a clear advantage regarding the cost of the devices due to the fast manufacturing process.

5.2. Thermo-optic switch

5.2.1. Digital and interferometric switches

There are two basic principles used in thermo-optic switches. Interferometric switches are based on a Mach-Zehnder interferometer (MZI), where a first power splitter divides the propagating light in two branches. A phase shift in one branch and a subsequent interaction in an interference structure, i.e. a directional coupler, switch the light into one of the two possible outputs. In a digital optical switch (DOS) a gradient in the refractive index is induced in a Y-splitter. The induced index gradient guides the light into the branch with the higher refractive index.

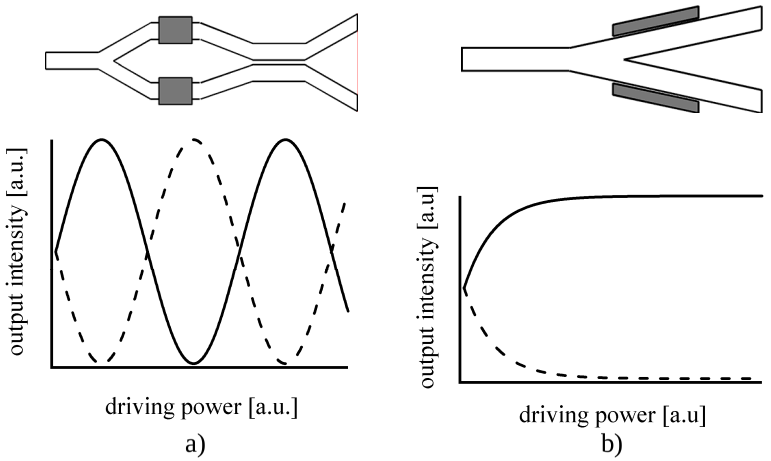

Fig. 5-4: Switch behavior as a function of the electrical driving power. a) Periodic function of an interferometric MZI switch with a voltage applied to one of the heaters. b) Digital switch function, when the applied voltage swaps from one heater to the other.

	interferometric switch	**digital switch**
length	~ cm	~ mm
needed index difference	lower	higher
power consumption	lower (10-50mW)	higher (20-200mW)
drive power	adjusted to optimum (periodic switch behavior)	insensitive to variations (digital switch behavior)
wavelength dispersion	critical	not critical
polarization	independent*	independent
switch speed	slightly faster (<5ms)	slightly slower (~5ms)

Table 5-3: Characteristics of interferometric and digital switches. In brackets some typical values for switches based on polymer materials are indicated.
* The directional coupler in the MZI structure can be designed polarization independent. However, a sensitivity to polarization is induced if the fabricated structure deviates from the design (e.g. different waveguide shape).

The characteristics of the two switch principles are listed in Table 5-3 and the typical switch behaviors are shown in Fig. 5-4.The most important difference between a digital and interferometric switch is obviously the switch behavior. In an interferometric switch the drive power has to be adjusted to ensure a phase shift of $\pi/2$ or $3\pi/2$. Additionally, the performance of an interferometric switch depends critically on the quality of the fabricated structure. With a DOS it is easier to find the needed drive power. The signal is switched to the desired output port as soon as the drive power reaches a certain level. For a higher drive power the signal remains constant at the output ports.
For the compatibility with optical fiber systems wavelength and polarization insensitivity is essential. Following the characteristics listed in Table 5-3, the DOS principle offers attractive features for applications in optical communication systems.
Similar to the passive PLCs, the polymer materials stand in competition with silica also for thermo-optic (TO) devices. Polymer materials have a clear advantage regarding the high TO coefficient. This characteristic is

required for providing low electrical power consumption. On the other hand, polymers have a lower thermal conductivity which limits the speed of a TO switch. However, silica based TO switches also have switch speeds in the order of a millisecond and are therefore only suitable for routing application, where whole bursts of data are switched to a specific channel. For this application, the switch speed of polymer based DOS is as well sufficient.

5.2.2. Thermo-optic simulations

In chapter 4.3 the measurement of the crucial parameters was described, needed to design a thermo-optic device. The values of the important parameters used in the simulations are listed here again:

- thermo-optic coefficient: $dn/dT = -2.5 \times 10^{-4}\ K^{-1}$
- thermal conductivity: $\lambda = 0.2$ W/mK
- heat capacity: $C = 1200\ Jkg^{-1}K^{-1}$
- density: $\rho = 1200 kg/m^3$

Commercially available software for integrated optics does typically not provide the combination of thermal and optical simulations. Currently, only the software packages of “R-Soft design group” and “Photonic Design” provide a thermo-optic module. But as mentioned earlier in this book, Femlab offers the possibility to solve almost any partial differential equation based on the finite element method (FEM). Therefore it is also a good tool for thermo-optic simulations. The following simulations were carried out using Femlab.
First the cross-section of the structure is considered (Fig. 5-5a). On top of the 20µm thick polymer layer a 8µm wide electrode is used as a resistive heater. The silicon wafer is used as a heat sink. The temperature at the bottom is assumed to be constant, what could be achieved with a temperature stabilized submount. The calculated temperature distribution in this model shows that the difference in temperature between the heating electrode and the bottom of the substrate decays entirely over the polymer layer (Fig. 5-5b). This is expected, as the thermal conductivity is significantly larger in silicon than in polymer (λ_{Si} = 130 W/mK, $\lambda_{polymer}$ = 0.2 W/mK). Consequently the substrate can be neglected for future simulations and the plane of constant temperature is shifted to the bottom of the polymer stack.
Results from this 2D simulation also show that the temperature decreases relatively fast below and besides the heater. Consequently the top cladding layer of a waveguide structure should be as thin as possible for influencing the structure with a low heating power. However, the top cladding has still to ensure that the guided mode is not influenced by the air or the electrode. A parameter which is influenced by a small cladding layer is the effective index of the waveguide. As long as the effective index is not influenced by a reduction of the thickness of the cladding layer, the guided mode does not see the air on top or the electrode. Considering the results shown in Fig. 5-6 a cladding thickness of 8µm is sufficient. The effective index starts to drop more clearly, if the cladding is thinner than 3µm. This correlates with the fact that the $1/e^2$-diameter of the mode is 10µm. For further simulations the cladding thickness will be fixed at 8µm. Being aware of the above consideration the temperature distribution in the polymer layer can now be simulated in 3D.

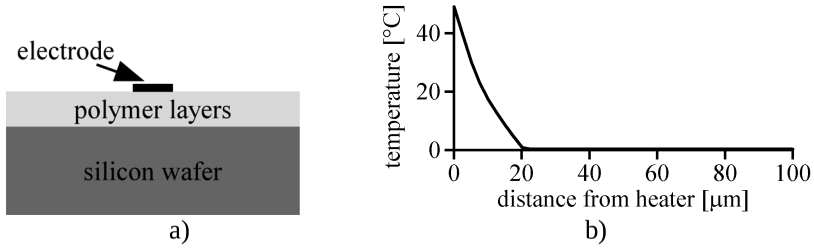

Fig. 5-5: a) Cross-section of a thermo-optic device with a heating electrode on top and a stack of polymer layers on a silicon substrate. b) Temperature decay from the heater through the polymer layer (20µm) to the silicon substrate.

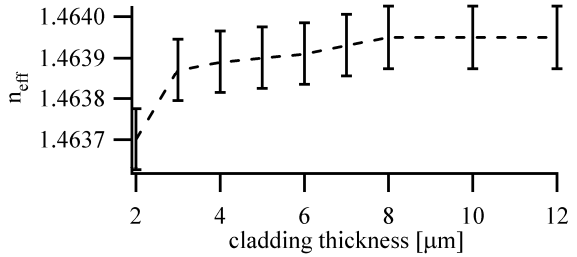

Fig. 5-6: Influence of thickness of top cladding layer on the effective index of the embedded waveguide. The effective index is simulated with FEM mode solver (APSS software).

As the optical simulation affords a very dense mesh, it is not possible to simulate the light propagation in 3D. Therefore, a slice of the 3D geometry is considered at the center of the waveguide core. From the calculated temperature distribution in this slice, the refractive index distribution can be deduced using the thermo-optic coefficient of the polymer material. Finally the optical simulation is carried out in this two dimensional slice.

5.2.3. Design of wide-angle digital optical switch

Based on the previous discussion a design of a DOS is shown here. The DOS consists of a Y-splitter and two heating electrodes. As discussed for the passive devices it is always favorable to have short devices. A short device has only a small propagation loss in the waveguide. Additionally, if the device is integrated on a chip with other waveguide structures fulfilling additional functions, the total chip size can be kept small.
For a Y-splitter it is difficult to reduce the device length, because the needed wide opening angle increases the radiation loss. However, this kind of optical switch is not used as passive device with half of the intensity at each output, but it is always switched to one output. Consequently, one is not interested in the insertion loss of the passive structure. Even though the radiation loss may be high for the passive device, with an optimized electrode geometry providing the appropriate refractive index distribution, it is possible to guide the light into one of the branches with a very low loss. Where usually opening angles of less than 0.5° are used for the basic Y-splitter, splitters with angles up to 3.5° are presented here. This wide opening angle allows the design of shorter switches with a length of only 4mm.
The structure of the digital optical switch can be divided into three parts:

(i) First we have a straight waveguide as an input. This section is hardly affected by the heating electrode.
(ii) The second part is the tapered region where the width of the waveguide increases. Normally the final width is double the width of the initial waveguide. As the opening angle of the Y-splitter is large in the present design, some additional space is needed. This enlarged tapered section gives the opportunity to “push” the light by the thermo-optically induced refractive index gradient to one side of the structure. As a result, no light couples into the second branch anymore.
(iii) After the tapered section the waveguides start to separate. As long as they are not separated sufficiently, the heater has to guarantee that no light couples back into the second branch. As the width at the end of the tapered region is more than twice the width of the waveguides, the separated branches start also with a tapered section. This section also helps to trap the shifted guided mode in the waveguide of the branch.

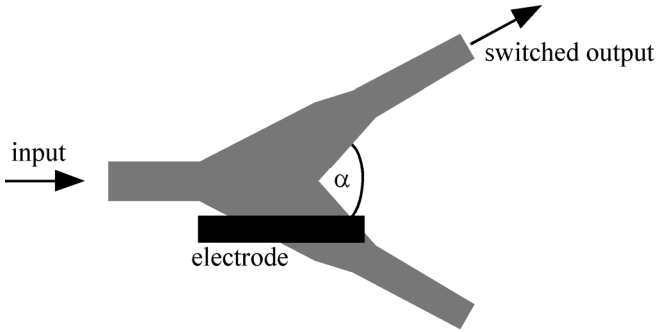

Fig. 5-7: Schematic view of the switch design. The special characteristics are the wide open angle of α = 3.5°, the large tapered section and the tapered branches.

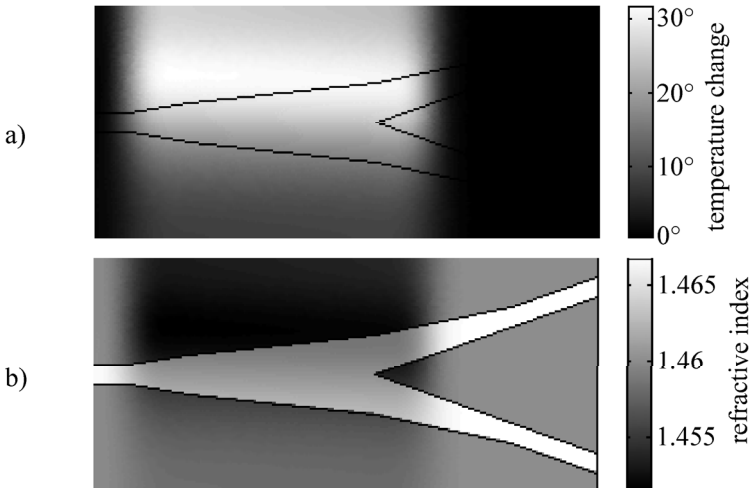

Fig. 5-8: a) Temperature distribution in the plane of the optical simulation at the core center. The driving power is 8mW. 0° corresponds to room temperature. b) Deduced distribution of the refractive index based on the refractive index of the material at room temperature and the thermo-optic effect.

Fig. 5-7 shows a schematic view of the switch design. The position of the electrode is parallel to the input waveguide. With this position the mode is initially pressed to the upper side of the waveguide structure and has then the possibility to go slowly back to the middle of the output waveguide.
As described in chapter 5.2.2 the thermo-optic simulation is done with a thermal 3D simulation and a consecutive optical 2D simulation. Fig. 5-8 shows the temperature and refractive index distribution that is used for the optical simulation. In Fig. 5-9 the results from the optical simulation are depicted for the off-state without an applied voltage and the on-state with the activated heater. It is obvious that in the off-state the Y-splitter has significant radiation loss at the junction, whereas the loss in the on-state is negligible. Table 5-4 lists the performance criteria of the simulated switch. Not included in the results obtained from the simulations is the propagation loss due to absorption and scattering in the waveguide.

a)

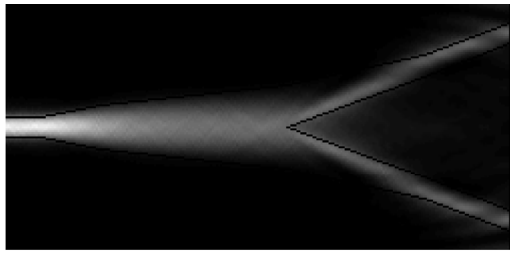

b)

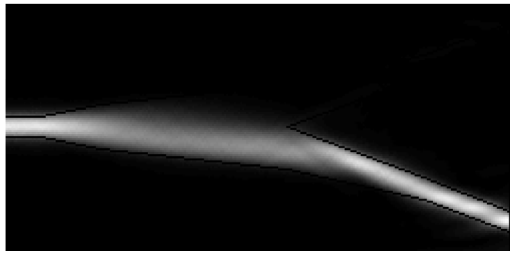

Fig. 5-9: Simulated optical field distribution in the Y-splitter: a) Off-state without any voltage applied. b) On-state with a voltage applied to the upper electrode.

5.2.4. Fabrication of thermo-optic devices

In addition to the normal waveguide structure a heating electrode needs to be fabricated. Metal layers of aluminum or chromium have a good adhesion on polymers and are quite easily etched with wet etchants.

The thickness of the metal layer is given by the desired electrical resistance of the electrode. The maximum heating power that is needed is below 100mW and should be provided with an applied voltage of less than 4V. Therefore, the electrical resistance should be in the range of 25-35Ω. The electrode also needs to be hard enough that the electrical contacts can be accomplished with a wire bonder. Both considerations lead to a thickness of the electrodes of at least 300nm. As chromium layers of this thickness tend to build cracks, the electrodes are fabricated with aluminum (Fig. 5-10). The structures are etched using a commonly used PAN-etch consisting of phosphoric, acetic and nitric acids.

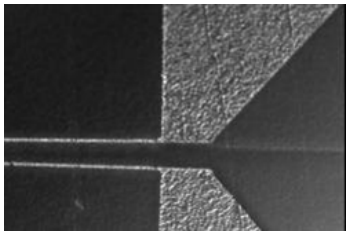

a)

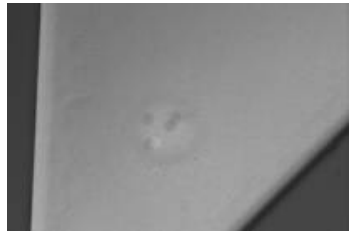

b)

Fig. 5-10: Electrodes based on a) chromium and b) aluminum. The aluminum electrodes have a good quality and provide the desired electrical resistance of ~ 35Ω.

5.2.5. Characterization of thermo-optic switch

A first criterion influencing the performance of the TO switch is the positioning precision of the electrodes with respect to the waveguide structures. Where the longitudinal position (in the direction of light propagation) is not very critical, the lateral position of the electrode is crucial for the device performance.
The alignment in the fabrication process is done with verniers patterns that provide a 0.5μm precision (compare Fig. 6-6). However, as the embedded waveguide structures have only a small refractive index contrast and as the UV-written waveguides do not have a perfect rectangular shape, the alignment process is difficult. Usually a lateral shift within 1-2 μm is achieved (Fig. 5-11). Even though the alignment of the electrodes is not perfect, the experiments showed that the switches are well symmetric. The same characteristics were measured for switching in output 1 or output 2.
The electrodes were contacted with small needles and the voltage was applied via a balanced electrical switch. The electrodes had an electrical

resistance of 35-43Ω. This is close to the targeted value of 25-35Ω and confirms the quality of the electrode fabrication.
The light was coupled into the waveguide by bonding a fiber to the input (see chapter 6.2). The light at the outputs was collimated with a lens and focused on a detector. Table 5-4 lists the measured performance criteria of the fabricated TO switch in comparison to the simulation and the targeted specifications. The targeted specifications are mainly based on the performance of commercially available devices.
The insertion loss in the off-state and in the on state corresponds well to the simulated value. It shows that the simulation with FEM and the combination of the 3D thermal and 2D optical simulation give a good representation of the real structure. Additionally, the principle that the heated structure has a lower excess loss than the passive structure is clearly demonstrated with this switch (Fig. 5-12).
The time to switch between the off-state and the on-state is less than 1ms following the simulation (Fig. 5-13). This value corresponds to the time, when the signal change is accomplished by 90%. In the experiment the switching speed is 2ms (Fig. 5-14), which is still clearly below the targeted specifications (Table 5-4). It has to be stated that the time to switch over from one output to the other is longer than the time needed to switch on from the off-state to the on-state. The time to switch over is approximately increased by a factor of two [45].

	targeted	**simulated**	**measured**
insertion loss (on-state):	2 dB	0.1 (1.1) dB	1.3 dB
cross-talk:	-25 dB	-33 dB	-23 dB
power consumption:	25mW	8 mW	40 mW
excess loss in off-state:	-	1.5 dB	1.5 dB
electrical resistance of electrodes:	25-40 Ω	40 Ω	35-43 Ω
switch speed:	< 5ms	1 ms	2 ms

Table 5-4: Targeted, simulated and measured performance criteria of the TO switch. The simulated insertion loss does not include propagation loss and coupling loss. The value in parenthesis is estimated for the total insertion loss assuming a propagation loss of 0.4dB/cm and 0.7dB coupling loss. The switching speed is defined as the time when the signal change is accomplished by 90%.

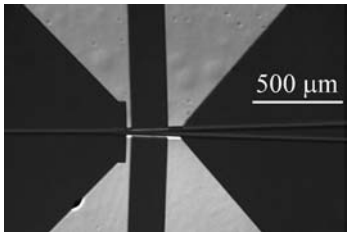

Fig. 5-11: Y-splitter with electrode on top. The large pads enable an easy electrical contact. The heating part of the electrode has a width of 8µm.

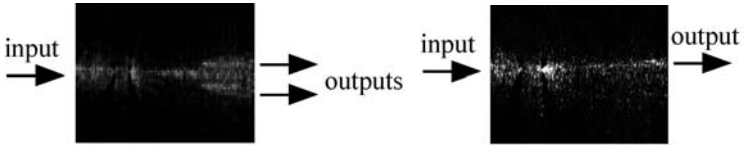

Fig. 5-12: Infrared image of the off- and on-state of the TO switch. Light is propagating from the left to the right. a) Off-state: In the off-state the light radiated into the region between the two branches is clearly seen. b) On-state: the light is guided to the upper output.

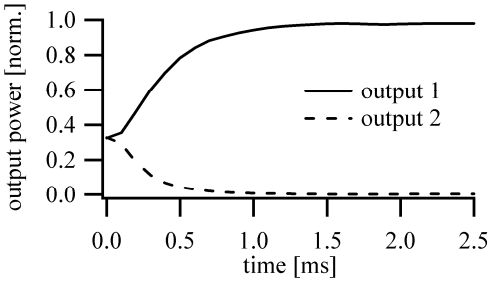

Fig. 5-13: Simulated switch dynamics after applying a voltage. The switching speed is 1ms.

As mentioned before, the switching time is relatively slow due to the low thermal conductivity. But it is still sufficient for routing applications. The deviation from the switch speed deduced from the simulations can be explained by the fabrication of the waveguide structure. First of all, the top cladding layer is slightly thicker than assumed in the simulations. Furthermore, the UV-written waveguides have a tunnel-like shape and are larger than desired. Therefore, the geometry below the electrodes is not

exactly the same as designed in the simulations. These differences between the simulated and the realized structures also explain the higher power consumption and the higher cross-talk.
Possibly better results could be achieved with the same mask layout if the waveguide shape in the fabricated structure would be more rectangular. However, already the achieved results show a satisfying low insertion loss. The power consumption of only 40mW is lower than in most of the presented TO switches. For silica based DOS the power consumption is usually close to 1W and also in presented polymer devices the power consumption is in the range of 50-200mW [45]-[51]. There are mainly two reasons for the low switching power achieved in the presented wide-angle switch:

- The broad tapered region gives more space to guide the mode towards one of the outputs. Therefore, a smaller refractive index change is needed.
- The electrodes were designed to be as short as possible. Longer electrodes would dissipate more power. However, they would possibly also provide a better extinction ratio.

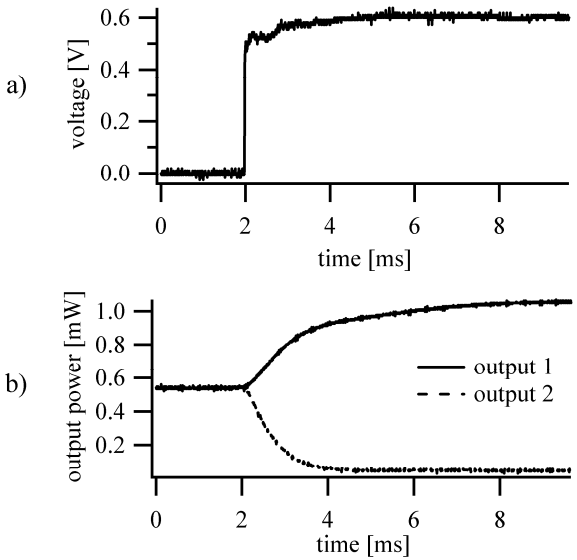

Fig. 5-14: Measured switch dynamics. a) The voltage is applied after 2ms. b) The switching time is 2ms.

Considering the achieved results, it should be possible to attain the targeted specifications as listed in Table 5-4. In order to get there, the most important step will be an improvement of the fabrication quality of the waveguide structure.

5.3. Variable optical attenuator

5.3.1. Design

Variable optical attenuators (VOA) are another typical application for polymer PLCs. One possible function is to homogenize signals of different channels that have been amplified individually. Another application is the attenuation of light before hitting a detector or another device that only withstands a certain intensity. Typically a VOA should tune the insertion loss between almost zero and 30dB.
Again, there are basically two principles present for VOA designs (Fig. 5-15). The MZI structure uses a phase-shift and interference for tuning the output signal. As for the thermo-optic switch, this design only needs a very small driving power. On the other hand, if the two branches of the MZI are not exactly of the same optical length, there is already a slight destructive interference without applying a voltage. Thus, for a minimal insertion loss the structure has to be tuned by heating one branch. Additionally, if the split ratio of the power splitter at the beginning of the MZI structure is not perfectly equalized, it will not be possible to extinct the signal by interference. It is therefore difficult to achieve the desired maximal attenuation.

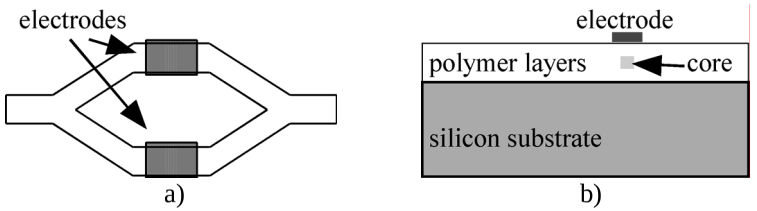

Fig. 5-15: Typical VOA designs: a) In the MZI structure the signal is attenuated by destructive interference. b) A heater on top of the waveguide pushes the mode towards the substrate. The light then starts to couple into the substrate due to its higher refractive index.

In the second design, the heater is simply positioned on top of a straight waveguide. The lowered refractive index that is induced by heating presses the mode down towards the substrate. The evanescent field of the guided mode starts to couple into the silicon substrate and is lost. When the applied voltage exceeds a certain magnitude, the mode is not guided any more and the attenuation is almost complete. Due to its simplicity this kind of VOA was investigated in this work.
The simulation of the considered VOA structure is difficult. The difficulty lies in the fact, that the light is guided in a structure of small refractive index contrast adjacent to a substrate with a much higher refractive index. In the previous structures the substrate was neglected because it did not influence the performance of the structure. In the VOA the light interacts with the silicon substrate. One part of the light is reflected from the surface and the other part couples down into the substrate. The APSS software as well as FEMLAB are not suitable for the simulation of such structures and the results are not reliable.
Fortunately, the design is simple enough to estimate how the geometry should look like without simulations. Principally there are two possibilities for the electrode design:

- Either the attenuation is done over a short distance with a high temperature increase,
- or a longer electrode with moderate temperature attenuates the signal.

In any case the thickness of the bottom cladding and the top cladding will dominate the performance of the VOA. Accordingly, electrodes of different length (0.5mm - 5mm) were chosen as heater on top of the straight waveguides. The width of the electrodes was 10µm.

5.3.2. Characterization of VOA structures

The targeted attenuation in a VOA is >20dB [52]. The typical heating power to achieve this attenuation is usually between 20 and 60mW for polymeric VOA's [52]-[54].
The best results were achieved with the shortest electrodes. All electrodes reach the same maximum attenuation. However, the longer the electrode is, the more power is needed for the same attenuation. This indicates that it is more efficient to introduce a higher attenuation over a small distance than to introduce a smaller attenuation over a longer distance. Fig. 5-16 shows the attenuation of a fabricated VOA structures with a 0.5mm long electrode as a function of the heating power. The maximum attenuation is

sufficient with 28.5dB. For achieving an attenuation of 20dB a heating power of 65mW is needed. For longer electrodes the heating power increases more or less linearly for the same attenuation.
As the VOA structures were fabricated on the same wafer as the DOS-structures, the thickness of the bottom cladding layer is not minimized (~10µm). The layer thickness could be reduced to ~7µm without causing any loss to the substrate. This reduction should lower the needed heating power, as the evanescent field is closer to the substrate and light couples down more easily. Consequently, the necessary heting power could be considerably reduced.
The same concept for a VOA is used by the company Gemfire. Gemfire was one of the first companies that had a commercially available product based on polymer waveguides that has passed the Telcordia environmental tests. The specifications of Gemfire's VOA devices are given in Table 5-5.

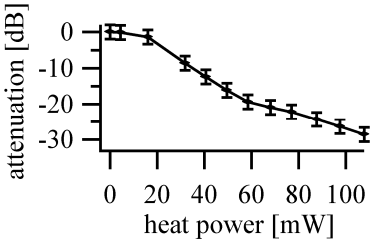

Fig. 5-16: Attenuation of a VOA structure as a function of the heating power. The electrodes dimensions are 0.5mm x 10µm x 0.3µm.

insertion loss	1.3 dB
dynamic range	up to 40 dB
power consumption at 20dB attenuation	20 mW

Table 5-5: Specification of the VOA devices provided by the company Gemfire.

6. Fiber pigtailing of waveguide chips

6.1. Coupling efficiencies and alignment tolerances

A short theoretical discussion about coupling loss between a waveguide and an optical fiber is already given in chapter 2.3.1. The approximation with Gaussian beams shows that the most critical parameters are the mode overlap of the waveguide mode and the fiber mode as well as the angular and lateral alignment precision. The longitudinal alignment along the propagation of the light is less critical. It is even more relaxed, when an index matching adhesive is used to fill the gap between the waveguide chip and the fiber.
Within a diploma thesis carried out in correlation to this work different coupling methods for coupling light into a 5µm x 5µm waveguide were theoretically analyzed [55]:

- Butt coupling: for butt coupling standard SMF-28 fibers are considered.
- Coupling with lensed fibers: The considered lensed fibers have a core diameter of 10µm, a lens curvature radius of 18µm and a core radius decreasing factor of 0.5. The gap between the fiber tip and the waveguide is 29.4µm. These values correspond to commercially available lensed fibers.
- Coupling using an additional lens: A commercially available Selfoc PHC lens with a radial index gradient was considered.

Table 6-1 compares the maximum coupling efficiency (CE) and the alignment tolerances of the different coupling techniques.
The best mode overlap is achieved with a lensed fiber. However, the Fresnel loss reduces the maximal coupling efficiency slightly. In a system with a lens even the Fresnel loss at the lens itself reduces the coupling efficiency. Here, the big advantage of butt coupling is obvious, as an index matching adhesive can eliminate the Fresnel loss.
The simulations also showed that with butt coupling the alignment tolerance is slightly less stringent. Table 6-2 compares the performance of the different coupling techniques if a certain misalignment is assumed. The

values show that for lensed fibers the optimal mode overlap does not compensate for the tighter alignment tolerances.
As the precise alignment and fixation of the fiber is a very difficult task, it is more reasonable to choose a process with the advantage of a less stringent alignment tolerance, although the maximum achievable coupling efficiency may be slightly smaller. Additionally, lensed fibers are much more expensive. Thus, based on the results shown in Table 6-1 and Table 6-2, butt coupling with cleaved single-mode fibers was used in this work. Fig. 6-1 shows the dependency of the coupling efficiency on the lateral and longitudinal misalignment for a butt-coupled SMF-28 fiber.

technique	**max. coupling eff.**	**lateral misalignment for 10% loss**	**angular misalignment for 10% loss**	**longitudinal misalignment for 10% loss**
butt coupling	91% (91%)	1.42 µm	2.21 °	40.8 µm
lensed fiber	100% (96%)	1.15 µm	-	18 µm
extra lens	94% (85%)	WG: 0.85 µm lens: 0.5 µm	fiber: 2.0° WG: 3.3° lens: 0.02°	fiber: 31 µm WG: 11 µm lens: 15 µm

Table 6-1: Coupling efficiency and alignment tolerances for different coupling techniques. The maximum coupling efficiency is given with (in brackets) and without considering Fresnel losses.

technique	**CE with 2µm lateral shift**	**CE with 2° angular misalignment**	**CE width 30µm longitudinal misalignment**
butt coupling	74%	83%	79%
lensed fiber	70%	-	51%
extra lens	WG:48% lens: 19%	fiber: 77% WG: 81% lens: 0%	fiber: 77% WG: 37% lens: 58%

Table 6-2: Coupling efficiencies for a given misalignment assuming that the other alignment parameters are optimized.

The coupling efficiency of 91% as well as the alignment tolerances could be slightly improved by tapering the waveguide at the input and output. As this tapering is only feasible in the lateral direction the improvement is only within 2-3%. A further improvement is achieved, when the size of the waveguide core is maximized, still fulfilling the singlemode condition.

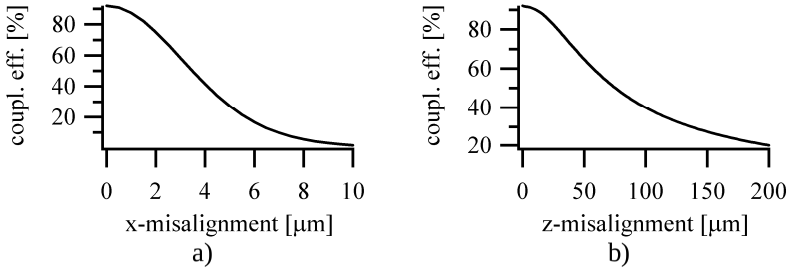

Fig. 6-1: Coupling efficiency as a function of a) the lateral and b) longitudinal misalignment. Obviously the coupling efficiency is much more sensitive to lateral shifts.

6.2. Active fiber alignment

As mentioned above the critical parts of fiber pigtailing regarding the final coupling loss are the alignment of the fiber and the subsequent fixing of the fiber.
For the fixation we concentrated on bonding the fiber with adhesive. The contact area between a bare fiber and the facet of the waveguide chip is not sufficient to hold the fiber in place. Therefore, the waveguide chip and the fiber are attached to a common substrate (Fig. 6-2). In this approach the fiber is first attached to the waveguide facet and afterwards fixed on the substrate with a larger drop of adhesive that withstands higher pull forces. The disadvantage of such a structure is that different materials (substrate, chip, fiber, adhesive) with different thermal expansion are attached to each other. This can lead to stress and misalignment when the temperature changes.
Another more suitable approach is the use of fiber blocks with one or multiple fibers fixed in a silica block. For devices with multiple outputs like splitters, these fiber arrays with 1-16 fibers have the advantage that only one alignment process has to be done for all outputs. The contact

area between the waveguide chip and the fiber block is now large enough to create a stable bond with UV curable adhesive. By adding a lid on top of the waveguide structure, the geometry around the waveguide core becomes symmetrical. The symmetry should reduce the shift due to thermal expansion and therefore stabilize the insertion loss in environmental tests.
A drawback of this procedure is the need of flat chip facets. As the here considered waveguide chips are cleaved, the facets of the waveguides and the particularly of the silicon substrate are sometimes not completely flat as they do not always perfectly break along the crystal plane. Additionally the crystal plane that build the edge of the cleaved chip has an angle of 83° instead of 90° to the waveguide surface. An optimal longitudinal alignment is thus not possible. However, the tolerance for the longitudinal alignment is relatively large and a small gap of some microns does hardly influence the coupling efficiency.
The angular alignment is automatically given by the facets of the fiber block and the waveguide chip. As the waveguide chip is cleaved along the crystal axis of the silicon wafer, it is important that the waveguides are structured perpendicular to the cleaving axis. If this is fulfilled a good angular alignment between waveguide and fiber is guaranteed. Fig. 6-3 shows a fiber pigtailed straight waveguide with fiber blocks and fused silica lids.
An important parameter for a reliable bond and an efficient coupling between the fiber block and the waveguide chip is the choice of the adhesive. The desired characteristics are

- a low shrinkage during the curing process
- UV curable
- stable in environmental tests
- low absorption at telecom wavelengths
- index matching with fiber and waveguide
- low thermal expansion coefficient
- good adhesion on different kind of materials

Today, adhesives with these characteristics are available:

- Refractive index: 1.50 - 1.55
- Thermal expansion: 63 x 10^{-6} /°C (below T_g)
- Degradation temperature: ≥ 300 °C
- Glass transition temperature: T_g > 100°C
- Moisture resistance: 0.0146% weight gain

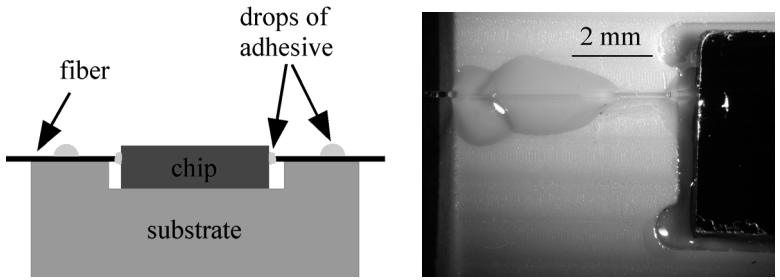

Fig. 6-2: a) Fibers and chip are fixed on a common substrate. b) Waveguide chip on a plastic (PEEK, polyetheretherketon) substrate with attached fiber.

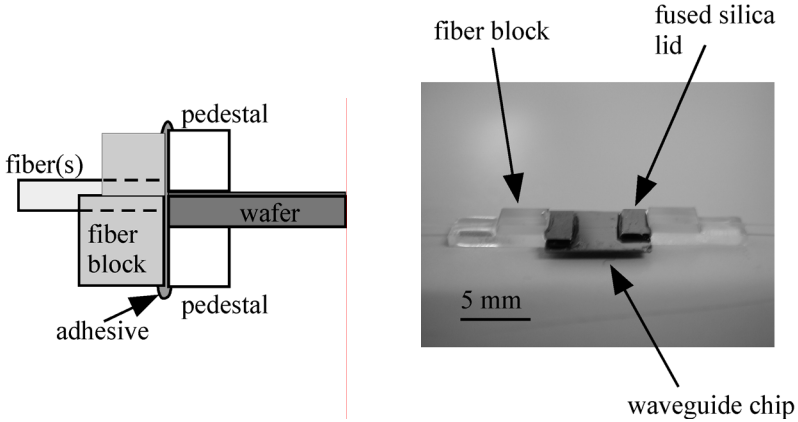

Fig. 6-3: a) Schematic of a fiber array bonded to a waveguide chip. b)Fiber pigtailed waveguide chip with a straight waveguide, two fused silica lids and fiber blocks.

The active alignment of the fiber blocks was done with a xyz-stage with a resolution of 0.1μm. The procedure of fiber pigtailing a waveguide chip includes the following steps:

(i) Fixation of fused silica lids on the waveguide chip with UV curable adhesive
(ii) Dispensation of a small amount of UV-curable adhesive on the facet of the fiber block
(iii) Alignment of the fiber block for minimal insertion loss: If the mounted fiber block can still be moved slightly, the angular alignment is automatically done when the fiber block and the chip are in contact. The light at the output of the device is focused on a detector with a lens. The minimized insertion loss should be close to

$$IL = 0.5\frac{\mathrm{dB}}{\mathrm{cm}} \times length\ of\ device\left[\mathrm{cm}\right] + 0.4\,\mathrm{dB}$$

(propagation loss + coupling loss of one fiber-waveguide transition)
(iv) UV-cure of adhesive: In this step the insertion loss sometimes increases slightly by up to 0.2 dB due to a shift of the fiber caused by stress (mainly shrinkage) in the curing adhesive. To minimize this shift it is important that

- only a small amount of adhesive is dispensed
- the fiber is slightly pushed against the waveguide chip to have a minimized gap between the fiber and waveguide
- the UV-exposure is symmetric with respect to the axis along the fiber.

(v) Repetition of step 2 to 4 with second fiber block at the output of the waveguide chip. The insertion loss should now be close to

$$IL = 0.5\frac{\mathrm{dB}}{\mathrm{cm}} \times length\ of\ device\left[\mathrm{cm}\right] + 2*0.4\,\mathrm{dB}$$

(propagation loss + coupling loss of two fiber-waveguide transitions)

With this procedure a 1cm long straight waveguide was pigtailed. The minimum achievable insertion loss for this structure would be 1.3dB. The achieved insertion loss was 2.0dB, which corresponds to a coupling loss of 0.75dB per facet. The 0.35dB coupling loss additional to the minimal achievable coupling loss is a result of misalignments due to

- the topology of the chip facet
- an angular misalignment of the waveguides with respect to the crystal axis of the silicon substrate
- a shift introduced in the curing process.

Nevertheless, the achieved insertion loss of 2.0dB over a 1cm long device is a promising result. As an example, the tolerated excess loss of a 1x4 splitter is 1.6dB. This device also has a length of approximately 1cm. By using a more stable and automated alignment stage and by optimizing the coupling loss with tapered waveguides, the coupling loss would slightly decrease and an insertion loss of 1.6dB would be achievable.

6.3. Passive fiber alignment

Another approach to align fibers to the inputs and outputs of a waveguide chip is based on the use of a substrate with alignment structures that predefine the position of the chip and the fibers (Fig. 6-4). This approach provides a faster and less expensive fiber pigtailing. However, it is more difficult to achieve the demanded accuracy.

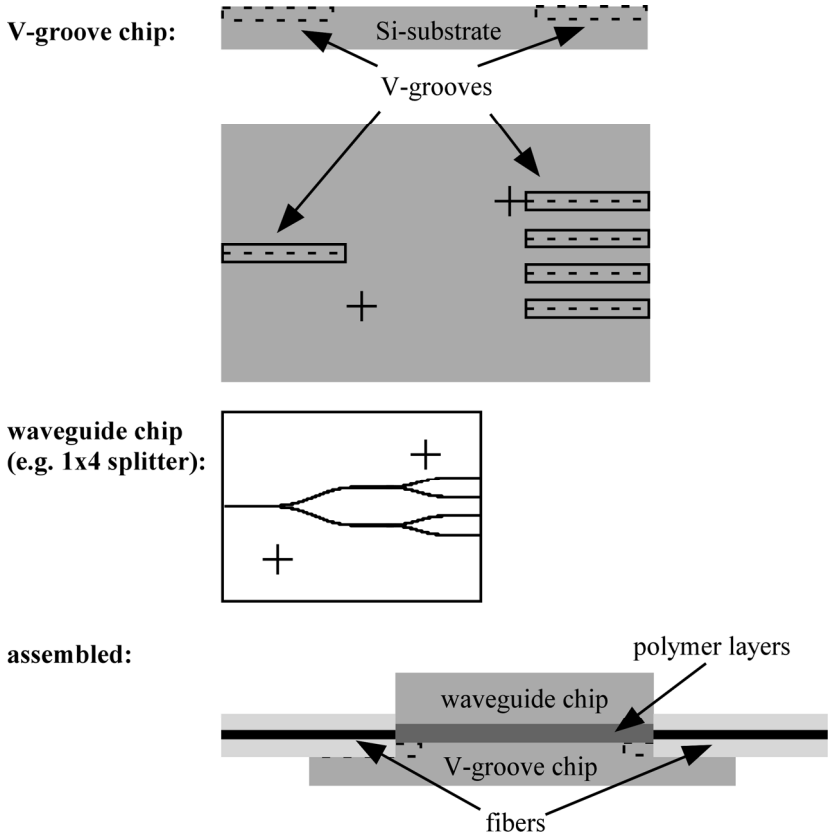

Fig. 6-4: Flip-chip process with passive fiber alignment.

For the passive alignment of the fibers, V-grooves are etched with KOH (potassium hydroxide) into a silicon substrate. The sidewalls of the V-grooves make an angle of 54.75° with the substrate surface. Therefore, the width of the V-groove at the top gives the final depth of the structure and also the vertical position of the fiber core. The fibers are glued into the V-

grooves with a UV-curable adhesive. To ensure a well defined position of the fiber, a top lid presses the fiber slightly into the groove (Fig. 6-5). Measurements with a profilometer showed that the vertical position of the fiber is varying by less than 1µm with this technique. The precision of the fiber alignment is thus finally given by the accuracy of the V-groove fabrication.

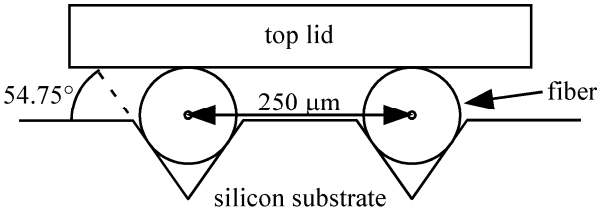

Fig. 6-5: Schematic view of fibers placed in V-grooves.

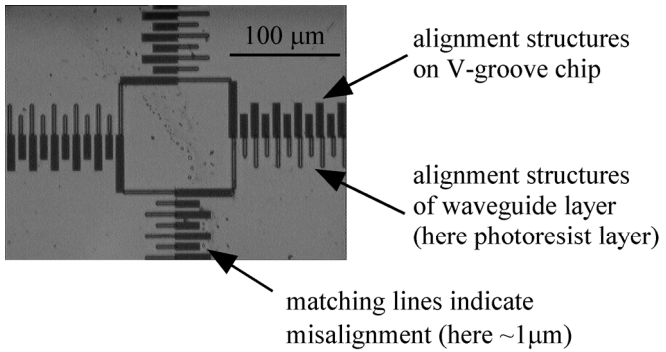

Fig. 6-6: Alignment marks after flip-chip bonding a glass chip onto a V-groove chip. The waveguide structures on the glass chip consist of a photoresist layer. The Vernier has a pitch difference of 0.2µm. The alignment accuracy is within 1.5µm.

As the vertical position of the fiber core is more or less on the level of the substrate surface, the waveguide chip has to be flip-chiped onto the substrate. The positioning of the waveguide chip is done with alignment marks. In the active fiber alignment process described in chapter 6.2, the critical step is the alignment of the fiber blocks. In the passive alignment approach, the critical step is now shifted to the flip-chip bonding of the waveguide chip. Once the PLC chip is positioned, the fibers are automati-

cally aligned in the fiber grooves. The advantage is that the alignment is done with alignment marks in an appropriate flip-chip machine and no optical signal has to be maximized during the process. Additionally only one alignment procedure has to be done as the position of the fibers is predefined. In the active alignment process each fiber or at least each fiber block as to be aligned subsequently.

The position of the waveguide structures with respect to the V-groove substrate can be checked after the flip-chip bonding. Fig. 6-6 shows the alignment marks of the substrate and the photoresist structures. The Verniers patterns used as alignment marks have a pitch difference of 0.2µm. The flip-chip machine offers an accuracy of 1µm which is more or less achieved with these structures.

For first tests, the waveguide structures where written in a photoresist layer on a glass substrate. The glass substrate enabled us to see the alignment marks after the flip-chip process and control the position of the chip after the bonding process.

For a precise alignment of the waveguide chip on the substrate, it is crucial to clearly see the alignment structures. As the UV-patterned waveguides, fabricated with the ZenPhotonics polymers, are written in proximity mode, the fine and closely spaced alignment structures are not sufficiently resolved. Additionally, the waveguide structures are embedded in a cladding with a small refractive index contrast. The flip-chip procedure could therefore not be repeated with the waveguide chips as the alignment structures could not clearly be seen. The necessary improvements can be achieved, if the top cladding layer is removed on top of the alignment structures and if the shape of the waveguide structures is more rectangular.

7. Environmental tests

Polymer optical waveguides have been studied for many years. For the most part these studies concentrated on the optical performance of the waveguides which includes optical loss, polarization dependence and thermo-optic behavior. A rarely considered issue was the stability of the polymer materials in harsher environmental conditions. Only in the last years, when the optical performance of polymer PLCs came to a marketable level, the environmental stability of polymer materials became important. In this chapter an overview of the standard environmental tests and some results achieved with the fabricated waveguide chips will be given.

7.1. Telcordia specifications

A well known standard for stability testing of optical components is given in the generic requirements of Telcordia (former Belcore). Telcordia is an outgrowth of AT&T's Bell Laboratories and is dedicated to developing testing, which helps to assure the practical lifetime of certain manufactured devices.
The requirements formulated in GR-1221-CORE (Generic Reliability Assurance Requirements for Passive Optical Components, 1999) and GR-1209-CORE (Generic Requirements for Passive Optical Components, 2001) relates to long term (25 year) performance of passive optical components. For polymer materials the tests concerning temperature and moisture resistance are particularly critical. An overlook over these tests claimed in GR-1221-CORE is given in Table 7-1. GR-1209-CORE claims similar tests with slightly different parameters. During these tests the performance of the optical components should always stay within the specification of the device.
Going through the Telcordia environmental tests is a long process. Therefore, only similar tests have been done with the here fabricated waveguide structures. These tests already show the potential and weak points of the devices.

Title	Description	Duration
Thermal shock	0°C to 100°C (in liquids) in less than 15s	15 cycles
High temperature storage (dry heat)	Storage at 85°C with ≤ 40% relative humidity (RH)	2000 hours
High temperature storage (damp heat)	Storage at 85°C and 85% RH	2000 hours
Low temperature storage	Storage at -40°C	2000 hours
Temperature cycles	-40°C to 70°C	100 cycles (ca. 14 days)
Cyclic moisture resistance	- 25°C to 75°C with 85-95% RH - One -40°C cycle per 5 sub-cycles	5 complete cycles (ca. 150 hours)

Table 7-1: Summery of the environmental tests claimed in GR-1221-CORE concerning temperature and moisture resistance. The performance of the optical device should always stay within the specification during these tests.

7.2. Environmental tests with waveguide chip

First tests were done with the bare waveguide chip. With these tests it is not possible to permanently monitor the optical performance of the structures under different conditions. Nevertheless, by characterizing the waveguides after the tests, a degradation of the polymer material would be observed. In addition, important knowledge about the adhesion of the polymer on the substrate is gained. The tests were carried out with straight waveguides fabricated with RPO polymers and ZenPhotonics polymers (compare chapter 4.1).
A first idea on the stability of the polymer layers was a "boiling water test", where the waveguide chips were put into boiling water. Both polymers withstood this high temperature and the polymer layers did not peel off from the substrate. Good stability was also observed in high tempera-

ture tests. The waveguide chips were baked at 200°C for 100 hours. No change in the propagation loss was observed in neither of the polymers.
A slightly different picture was observed when exposing the chips to heat *and* humidity. In a 95/95 test (95°C and 95% relative humidity (RH)), an intensification of the 85/85 test of Telcordia, the fluorinated acrylate of ZenPhotonics was more resistant than the polysiloxanes of RPO. This indicates that the fluorine in the acrylate polymer provides the better hydrophobic property then polysiloxane. After 100 hours in a 95/95 environment, the insertion loss of the polysiloxane waveguide increased by 30% although the polymer layer did not show any degradation by visual inspection. The loss increase is therefore due to moisture uptake. For the acrylate an increase in the insertion loss of 10% was measured. A closer inspection showed that the polymer layer started to peel off at the edge which increases the coupling loss. Therefore, it can be expected that the optical properties of the material did not degrade and the increased insertion loss correlates with the coupling loss. The problem of the dissolution at the edge of the cleaved waveguide chips can easily be solved by protecting it, e.g. with an adhesive. When attaching a fiber to the waveguide as described in chapter 6, this protection is given automatically.
Based on these results no further tests were done with polysiloxanes. The work focused on waveguides fabricated with fluorinated acrylates.

7.3. Environmental tests with fiber pigtailed chip

More rigorous measurements are possible with fiber pigtailed waveguide chips. The measurements shown below were carried out with 1cm long straight waveguides fiber pigtailed with two fiber blocks. During the tests in the environmental chamber the attached fibers pass through a feedthrough to the laser and photo detector and enable a constant monitoring during the test. The drawback of such a measurement is that a possible degradation of the sample is difficult to allocate. Not only the waveguide material but also the adhesive are exposed to the specific environmental conditions. The most critical point of the sample is no longer the waveguide itself but the coupling region from the fibers to the waveguide.
Good stability was observed in an 85/85 test. The insertion loss varied in a range of only ±5% (Fig. 7-1). As the measured signal only fluctuates and not constantly decreases, it can be concluded that neither the waveguide material nor the adhesive degraded during the test. A certain variation of

the measured signal may be due to a varying output power from the laser. Additionally, stress may be released or induced during the test in the adhesive which leads to a small shift of the fiber.

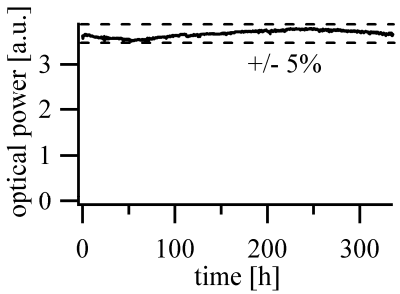

Fig. 7-1: 85/85 test over 14 days with fiber pigtailed straight waveguide.

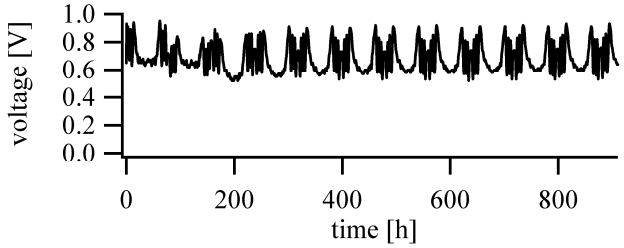

Fig. 7-2: Temperature cycles: Transition between 70°C and -40°C in 3.5 hours. The dwell time at the extremes is 30 minutes.

Much more critical regarding a constant device performance are temperature cycles. In this test the temperature changes between 70°C and -40°C within 3.5 hours. The dwell time at the extremes was 30 minutes. 42 cycles were carried out in 14 days. The signal variations (Fig. 7-2) obtained during heating or cooling periods indicate that the fiber is shifted with respect to the waveguide core due to thermal expansion of the materials. The symmetric constellation around the fiber and the waveguide cores should actually minimize this shift. However, the signal variations of 30% are very large. It is interesting to see that during a single heating or cooling period the signal fluctuates and does not constantly decrease or increase. For the moment, we do not understand what exactly induces the signal change. However, the positive conclusion from this measurement is that the signal always recovers to the same level after a cycle. This indi-

cates that the polymer waveguide and the adhesive withstand the temperature cycles.

The two measurements show that materials itself have a good stability and potentially withstand Telcordia tests. The more difficult part will be to find the coupling geometry that provides a constant performance during changing environmental conditions.

The fiber pigtailed chip will finally be packaged. The package may be a standard hermitic package or a cheaper quasi-hermetic encapsulation. Typically the trade-off of different packages is between the cost and the environmental stability. A sealed hermetic package provides a good mechanical and chemical protection for the waveguide chip, but it makes the whole device more expensive. If the pigtailed chip itself provides already a good environmental stability, a more simple package is sufficient and costs can be reduced.

8. Additional technology and device studies for planar lightwave circuits

In the frame of this work two topics related to the subjects presented so far were investigated. A key subject of this work was to develop an efficient technology for the fabrication of polymer waveguide structures. In this chapter a novel method for defining waveguide structures using photo-aligning liquid crystal polymers was developed with the result of a proof of principle. Light at a wavelength of 1550nm was guided through a multimode waveguide with core dimensions of 3µm x 10µm.
Another interesting topic in the field of integrated optics is wavelength filtering. In wavelength division multiplexed (WDM) transmission systems wavelength filters of small foot print and with a sharp box-like filter response are needed. Interesting candidates for the realization of such functions are micro-ring structures. A drawback of these structures is the tight fabrication tolerance. It will be shown, that with the micro-ring design discussed below these tolerances are enlarged. The design is also compatible with the earlier discussed polymer waveguide technology.

8.1. Waveguide fabrication with liquid crystal polymers

In this chapter another fast waveguide fabrication process based on UV printing through a mask is discussed [56][57]. For this process we used the polymer materials Staralign™ 2110 and Opalva™ 2130 [58]. Staralign is a linear photo-polymerizable (LPP) polymer based on the generic molecule poly(vinyl-4-methoxycinnamate) [56]. When exposed to polarized UV-light, the polymer chains of Staralign align themselves along the direction of the light polarization. Opalva is a liquid crystal polymer, optimized for liquid crystal displays and related technologies in combination with an LPP polymer. When spin-coated on top of a Staralign layer, the polymer chains of Opalva are aligned along the direction of the Staralign polymer chains underneath.

8.1.1. Waveguide fabrication

The fabrication process for the here presented waveguides includes the following two steps:

(i) First we spin-coat a layer with the Staralign material with a thickness of a few hundred nanometers. We then expose this layer to polarized UV-light. During the UV-exposure the polymer chains are aligned along the direction of the polarization of the UV light. For defining our waveguide structures we need two UV-exposures, each one with an intensity of 70mW/cm^2 for 6min. During the first exposure we expose through a mask and align the polymers in the future core region of the waveguides. For the second exposure we remove the mask and rotate the polarization of the UV-light by 90 degrees. Consequently the polymers in the cladding region are aligned perpendicularly with respect to the orientation in the core region (Fig. 8-1).

(ii) In a second step a layer consisting of the Opalva material is spin-coated with a thickness of 3µm. Opalva is a liquid crystal polymer with a transition from the nematic to the isotropic phase at 54°C. It is designed to align its polymer chains parallel to the polymer chains of the Staralign material in the layer underneath. For this alignment process the sample is heated to 50°C, slightly below the phase transition temperature. With a final unpolarized UV-exposure the orientation of the polymer chains in the Opalva-layer is fixed.

With this procedure we defined waveguide structures with widths down to 2µm (Fig. 8-1b). The processing time is below 1 hour.

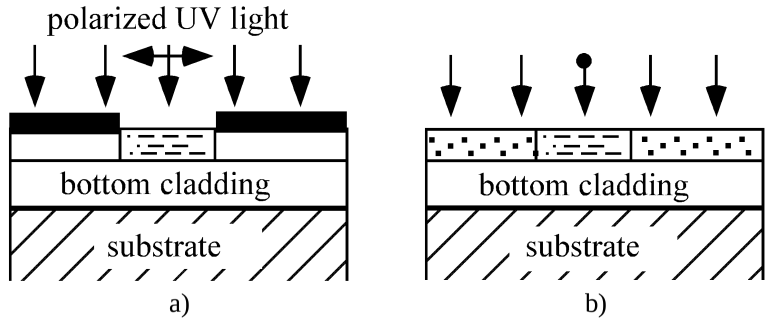

Fig. 8-1: Fabrication process of the alignment layer for the optical waveguides: a) A first UV-exposure through a mask aligns the polymer chains in the core region. b) After rotating the polarization of the UV-light and removing the mask, the polymer chains in the cladding are aligned.

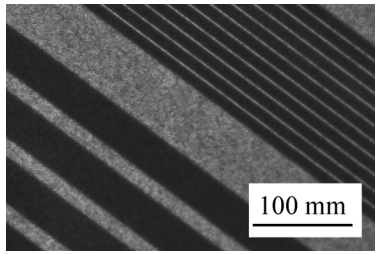

Fig. 8-2: Waveguide structures with width from 25μm (lower left) down to 2μm (upper right). The picture is taken with a polarization microscope (dark regions correspond to the cladding, light regions to the waveguide cores).

8.1.2. Refractive index measurement

The refractive index of the polymer seen by the propagating light depends on the orientation of the polymer chains. For TE polarization the polymer chains in the core region are aligned parallel to the electrical field of the propagating light (compare Fig. 8-3). Therefore the refractive index is high. In the cladding region the polymer chains are oriented in the direction of the light propagation. Therefore the light sees a smaller refractive index.

For measuring the refractive index in the different regions we aligned a layer of polymer chains all in the same direction. The layer was sandwiched between two 25nm thick gold layers resulting in an optical resonator. In a spectrometer (Perkin Elmer Lambda 19) we measured the location of the resonator peaks for both polarizations parallel and perpendicular to the polymer chains, respectively (Fig. 8-4a). With a matrix method for thin film filters [59] we deduced the refractive index at the wavelength of each peak and obtained the dispersion curve for both polarizations (Fig. 8-4b).We define n_3 to be the refractive index for the polarization parallel to the polymer chains and n_1 to be the refractive index for the polarization perpendicular to the polymer chains. Using these refractive indices at the peak wavelengths we can fit the Sellmeier Coefficients A, B, C (Table 8-1) in the Sellmeier equation (modified from [60])

$$n_i(\lambda) = \left(A_i + \frac{B_i \lambda^2}{\lambda^2 - C_i} \right)^{1/2} . \qquad (8\text{-}1)$$

With the obtained Sellmeier coefficients the refractive index can be calculated for any wavelength (Table 8-1). The accuracy of the deduced refractive index is 0.01. At a wavelength of 1550nm the refractive index is n_3 = 1.62 and n_1 = 1.55. This difference of the refractive index in the core and the cladding region of Δn = 0.07 is sufficient to guide light efficiently as the refractive index is also higher than the one of the bottom cladding (ZenPhotonics polymer) that is 1.45.

We also obtained the same results for the refractive indices with a second measurement. In this measurement the wavelength was kept constant at 1550nm and 638nm, respectively, and the sample was rotated. Again, we observed resonant peaks at certain angles from which we deduce the refractive index Fig. 8-5. The results were the same to within 0.01 of the first measurement technique.

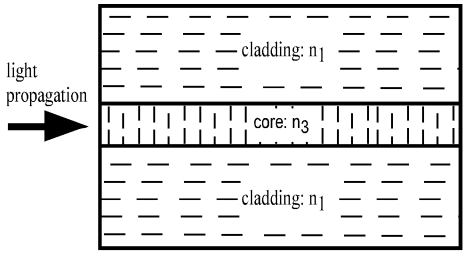

Fig. 8-3: The refractive index seen by the propagating light in the waveguide is different in the core region and the cladding regions due to the different alignment of the polymer chains.

	n_1	n_3
A	2.332	2.496
B	0.073	0.126
C [μm²]	0.127	0.130

	n_1	n_3
632nm	1.562	1.637
850nm	1.556	1.627
1300nm	1.553	1.622
1550nm	1.552	1.621

Table 8-1: Sellmeier coefficients obtained from the curve in Fig. 8-4 (wavelength in μm) and deduced refractive index at frequently used wavelength (accuracy: 0.01).

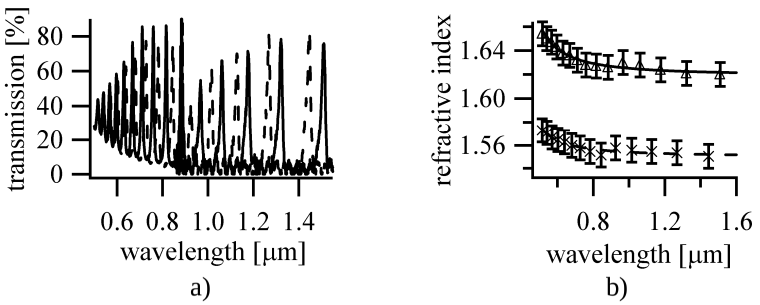

Fig. 8-4: a) Transmission spectra of waveguide polymer between two gold layers for p- and s-polarization (dashed line: n_1). b) Refractive indices deduced from the transmission spectra with a fit of the Sellmeier function (dashed line: n_1).

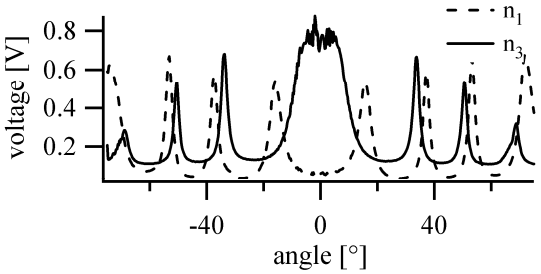

Fig. 8-5: Resonant peaks for the polarizations seeing the refractive index n_1 and n_3.

8.1.3. Waveguide characterization

The waveguides were characterized at the telecom wavelength of 1550nm with TE polarized light. Fig. 8-6 shows that light is guided through a waveguide of 10μm x 3μm in cross section and 1.2cm in length.
As the height of the waveguides is relatively small the coupling efficiency is low. This explains the high radiation on the left side of Fig. 8-6a. The fact that we clearly observe the guided light with a sensitive infrared camera from the top implies that there is also significant scattering from the waveguide. The reason for this can be observed in images from a polarization microscope similar to Fig. 8-2. At the edge of the core region the change of the polymer chain orientation is not always sharp. This means that either the polymer chains do not have a well defined orientation or the

orientation from the cladding region is sometimes slightly extended into the core region and vice versa. Consequently there are also fluctuations in the refractive index which leads to surface scattering. Additionally, there could be fluctuations in the orientation of the liquid crystal polymer in the waveguide that cause additional volume scattering.

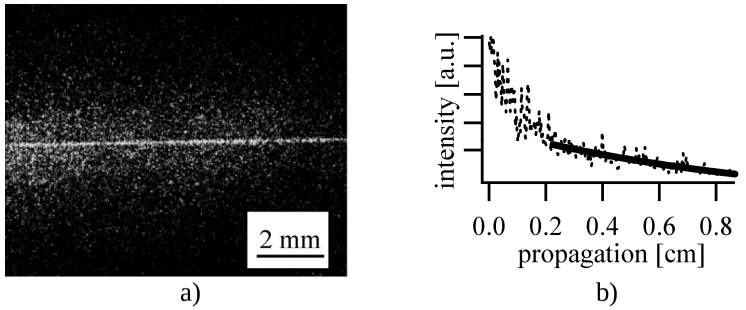

Fig. 8-6: a) Infrared picture of waveguide guiding light at 1550nm. Light is propagating from the left to the right. b) Decrease of the scattered intensity as a function of the propagation distance. The data are fitted with an exponential curve (solid line).

We measured the propagation loss by observing the intensity radiated from the waveguide with an IR camera (Fig. 8-6b). As the coupling is not optimized, in the first 2mm of the waveguide the radiation is mainly due to light not coupling into the waveguide mode. Afterwards, the decrease of the detected radiation is only due to propagation losses in the waveguide. This decrease was fitted with an exponential curve. The resulting loss at the wavelength of 1550nm is 4.0 ±0.3 dB/cm. An estimation on the surface scattering loss at the edge of the waveguide [61] shows that scattering causes at least half of the propagation loss.
The coupling efficiency could be improved by increasing the layer thickness of the guiding layer. For achieving a smaller propagation loss the exposure time in the alignment process of the Staralign-layer and the self-alignment procedure in the Opalva-layer need to be optimized in order to reduce refractive index fluctuations. Additionally the material is not designed for the use in the near infrared so that material absorption is higher than in other optical polymers for integrated optics. Consequently, optimizations in the process and the material could lead to tolerable propagation losses around 1 dB/cm.

If one rotates the polarization of the propagating light to TM polarization, the electric field oscillates perpendicular to the polymer chains in the core as well as in the cladding region. Therefore, the refractive index in the core is then very close to the one in the cladding and the light is not guided anymore.
Usually, one tries to obtain optical waveguides which are independent of polarization. With our material system (Staralign/Opalva) the waveguides are highly polarization sensitive, which allows the generation of new functionalities. As an example, by aligning the polymers differently in adjacent waveguides a polarization splitter could be devised. Or by slowly changing the orientation of the polymer chains the polarization state of the propagating light could be adiabatically rotated. This can lead to devices with a well defined output polarization which lowers the constraints on the polarization sensitivity for subsequent devices.

8.2. Microring structure for wavelength filtering

8.2.1. Motivation

Microrings (Fig. 8-7) have been suggested for different kinds of wavelength selective elements, such as add-drop filters or dispersion compensating devices [62]-[66]. For the realization of such optical functions, structures with an optical feedback are needed, which leads to a resonant device response. The main advantages of resonators based on microrings are the small size and the capability for large-scale integration on small footprint.
For many applications, rings with diameters ranging from 5 to 20μm are needed. Therefore, materials are used that provide a high-index contrast between the core and the surrounding material. With this high-index contrast, rings with diameters down to 3.4μm have been realized [64]. For single mode propagation in these high-index contrast waveguides, core dimensions of less than 1μm are usually needed. As standard optical fibers have core diameters of 9μm, direct coupling is inefficient and leads to a high signal loss unless the waveguides are tapered in the coupling region [67].
Additionally, the performance of a device, which is based on microrings, depends sensitively on the coupling between the straight bus-waveguide and the ring-waveguide. For a better control of the separation between the

two waveguides, vertical coupling with the ring on top of the bus waveguides has been proposed and demonstrated (see e.g. [68]). This design often implies wafer bonding, where the lateral precision in a mass production process is only within about 1μm. Consequently, an exact control of the coupling efficiency is also difficult to achieve.

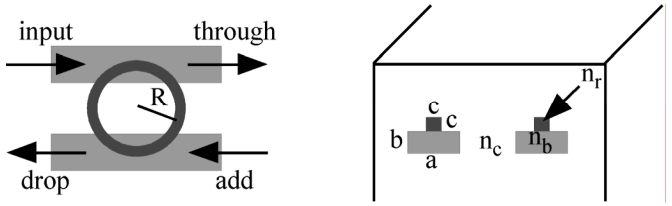

Fig. 8-7: Top view and cross-section of the proposed structure. The light is incident at the input port. Following the resonance condition in the microring the incident light is transmitted to the through port or transferred to the drop port. The dimensions are chosen as a = 4μm, b = 1.5μm, c = 0.7μm, n_r = 2.06, n_b = 1.535, n_c = 1.505 and R = 20μm. The vertical gap between ring and bus waveguide is set to zero.

Below, a microring structure is discussed that provides a good coupling efficiency with a standard single-mode fiber and eases also restrictions on the precision in the fabrication process of the microring itself.

8.2.2. Fabrication tolerant design of a microring structure

The considered structure is based on the combination of two waveguide types with different refractive indices in the core (compare Fig. 8-7). A low-index contrast bus-waveguide, i.e. the earlier discussed polymer waveguides, allows efficient coupling with an external fiber. A high-index contrast ring-waveguide ensures the feasibility of rings with small radii and a low bend loss.
As our chosen waveguide geometry results in different propagation constants a phase mismatch is introduced along the coupling region between the waves propagating in the two adjacent guides. Therefore, special attention is paid to the coupling between the two waveguides.

Design and structure dimensions

For the design of the microring structure we considered three important aspects:

(i) The coupling efficiency between the bus-waveguide and an external fiber
(ii) The sensitivity of the filter performance to fabrication variations
(iii) The phase mismatch in the coupling region of the ring and the bus waveguide

The proposed structure is shown in Fig. 8-7. The indicated dimensions give a good example for the considered material system. For the bus waveguide a sol-gel material was considered that can be used in replication technology. Obviously, the sol-gel material could be replaced by polymers. As high index material for the ring waveguide Ta_2O_5 was chosen.
The optimization aspect (i) implies that the core dimensions of the bus-waveguide have to be as large as possible while still fulfilling the single mode condition. The rectangular shape of the bus waveguide leads to a broad mode profile in the interaction region with the ring waveguide. This complies with aspect (ii) as will be shown later.
Aspect (iii) implies that the difference in the effective indices of the modes in the two waveguide types has to be as small as possible in order to achieve efficient coupling. This requirement is even more difficult to fulfill as the effective index of the mode in the ring waveguide is increasing when reducing the ring radius.
For minimizing the difference between the effective indices of the modes in the two different waveguide types we use the fact that the effective index of a mode in a waveguide increases with increasing waveguide dimensions and decreases with decreasing waveguide dimensions. Therefore, we have to maximize the dimensions of the bus waveguide (low-index contrast), which perfectly matches with the requirements from the paragraphs above. The ring waveguide (high-index contrast) is minimized to dimensions that are still compatible with the chosen waveguide technology (replication, UV-printing). With the waveguide dimensions shown in Fig. 8-7, Δn_{eff} becomes 0.18 at the wavelength $\lambda = 1.55\mu m$.
A low effective index in the ring waveguide is desired for minimizing the phase mismatch in the coupling region. However, the bend loss increases for smaller effective indices. With the dimensions given in Fig. 8-7 the bend loss in the ring is 1dB/cm. This bend loss is acceptable as the ring dimensions are very small. But it sets a limit to a further size reduction of the ring waveguide.

For the coupling between two different waveguides with a phase mismatch in the coupling region, an effective interaction length L_{eff} can be defined as [70]

$$L_{eff} = \left| \int_{-R}^{R} \exp\left(\frac{-\alpha_{bus} \cdot y^2}{2R} \right) \exp\left(-ik_0 \Delta n_{eff}\, y\right) dy \right| \qquad (8\text{-}2)$$

where α_{bus} is the decay constant of the bus mode in the cladding, R is the radius of the ring and y the direction along the bus waveguide. The smaller L_{eff} is the higher the coupling strength between the waveguide has to be. As shown in Fig. 8-8 L_{eff} becomes small in our structure. Therefore, we set the gap between the ring and the bus waveguide to zero to achieve a high coupling strength for compensation.

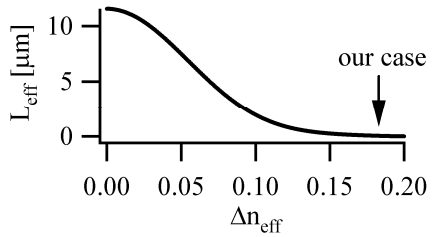

Fig. 8-8: Effective interaction length as a function of the difference of the effective indices of the modes in the bus and the ring waveguide Δn_{eff}.

The coupling efficiency between an external fiber and a channel waveguide similar to the bus waveguide of this structure has been discussed before. With the chosen dimensions the coupling efficiency is 70% what could even be improved with tapered sections. However, already a coupling efficiency of 70% is an improvement of 10dB compared to direct coupling between the fiber and high index waveguides of the dimension of the ring waveguide (cross section: 0.7µm x 0.7µm).

Fabrication Tolerances

As the coupling coefficient depends exponentially on the separation of the two modes [64], the exact positioning of the ring relative to the bus is very important. For a good control on the gap between the ring and the bus waveguides a vertical coupling design is often used where the ring is

placed on top of the two bus-waveguides. With this design the vertical separation between the ring and the bus can be well controlled with the thickness of an intermediate layer. But the lateral positioning precision of the ring relative to the bus-waveguides is given by the precision of the implied wafer-bonding process or mask aligning process. This precision is of the order of +/- 0.5 μm. In Fig. 8-9 one can see the relative change of the coupling coefficient with respect to this precision when using a small bus waveguide (equivalent to our ring waveguide) or using our proposed bus waveguide. With the large bus waveguide this change is reduced from 46% to only 6%. For enhancing the positive effect of a large bus waveguide, we have chosen a rectangular waveguide cross section (Fig. 8-7), which leads to a flattened mode profile in the coupling region.

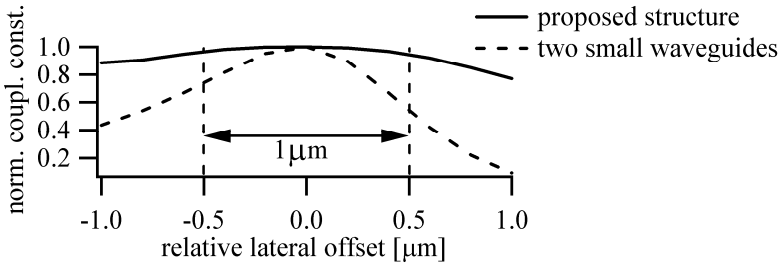

Fig. 8-9: Normalized coupling constant as a function of the deviation from the ideal position. The dashed line shows the coupling between two small waveguides, where the bus has the same dimensions and refractive index as the proposed ring-waveguide. The solid line depicts the coupling in the structure shown in Fig. 8-7.

Asymmetric Coupling and Filter Response

The coupling region between the bus- and the ring-waveguide was simulated with the finite-difference time-domain (FDTD)-method as well as with coupled mode theory. The conventional coupled mode theory is an approximation for weak coupling. As mentioned above, we have a high coupling strength between the ring- and the bus-waveguides, which makes the conventional coupled mode theory inappropriate. Additionally, a simple power conservation argument leads to the fact, that the coupling coefficients κ_{12} and κ_{21} between two waveguides must be complex conjugate of each other. That this is generally not true for two non-identical waveguides as is shown in an adapted coupled mode theory [36]. A short discussion of this theory was given in chapter 2.3.3.

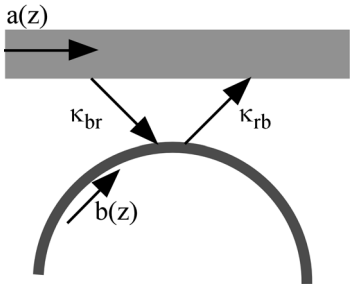

Fig. 8-10: Schematic diagram of the coupling region between the bus and the ring waveguide. a(z) and b(z) are the amplitude of the mode in the bus and ring waveguide, respectively.

Due to the phase mismatch in the coupling region, the coupling efficiency between the ring and the bus waveguide is very low. To overcome this problem, the two waveguides have to be brought very close together for achieving a good mode overlap. With the configuration in Fig. 8-7 and κ_{rb}^2 and κ_{br}^2 the power fraction coupled from the ring to the bus and the bus to the ring respectively (Fig. 8-10), we derived values of $\kappa_{rb}^2 = 0.006$ and $\kappa_{br}^2 = 0.023$ from our simulations. These coupling efficiencies are rather small, but still sufficient for applications with microring resonators. Other presented micro ring structures provide coupling coefficients in the range of $\kappa^2 = 0.03 - 0.20$ (e.g.[70]). Smaller coupling coefficients lead to a higher finesse of the filter response (see below). But for a good resonant enhancement of the light intensity in the ring it is then necessary that the optical loss in the ring is small.

Filter Response

In Fig. 8-11 the filter response of the structure depicted in Fig. 8-7 is shown. The amplitude filter response for the drop port is given by the equation below which is well known for Fabry Perot resonators:

$$A_{through} = \left(b_b + \frac{a_{br} b_r a_{rb} \gamma z^{-1}}{1 - b_r b_r \gamma z^{-1}} \right) A_{input}$$
$$A_{drop} = \frac{a_{br} a_{rb} \sqrt{\gamma z^{-1}}}{1 - b_r b_r \gamma z^{-1}} A_{input} \qquad (8\text{-}3)$$

a_{br} and a_{rb} are the amplitudes coupled from the bus to the ring and from the ring to the bus respectively. b_b and b_r are the transmitted amplitude in the bus and the ring respectively, after passing the coupling region. γ describes the round trip loss and $z^{-1} = e^{-i\Omega}$ (Ω = normalized frequency = ω - ω_0 with ω_0 the resonant frequency) [26].
In Fig. 8-11 the filter response is compared to a structure with symmetrical coupling. As can be easily seen, the here discussed structure has a higher finesse than a structure with identical bus and ring waveguides.

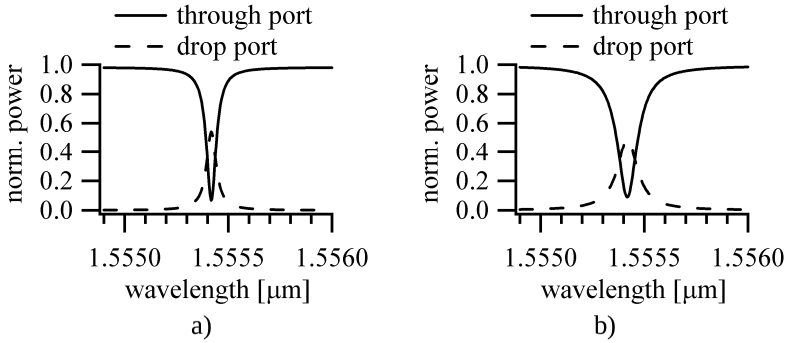

Fig. 8-11: a) Filter response for asymmetric coupling with $\kappa_{br}^2 = 0.023$ and $\kappa_{rb}^2 = 0.006$. b) Response of the same micro ring with symmetric coupling to the bus waveguide ($\kappa^2 = 0.023$).

Conclusion

The discussed design of a microring structure based on two different waveguide types concentrated on practical improvements for the implementation of microring structures in integrated devices. The asymmetric coupling between the two waveguides allows additional applications that require large intensities in the ring waveguide (e.g. sensors, nonlinear optics). Although the coupling efficiency is certainly reduced by the asymmetry, it is still strong enough for various applications such as e.g. optical frequency filtering.
We showed that the coupling efficiency between the bus-waveguide and an external fiber is improved by more than 10 dB without additional designs such as tapered coupling regions. Also the relative change of the coupling efficiency between the bus and the ring waveguide within the fabrication precision of the wafer bonding process is reduced from more than 46% to only 6%.

9. Conclusion and outlook

9.1. Conclusion

The performance of polymer based integrated optical devices has considerably improved over the last years. In certain applications like passive devices or thermo-optic devices they can compete with devices based on other materials and even show some favourable advantages. The present work includes the device development from the design to the pigtailed device. Although polymer waveguides have already been developed for a long time, a consequent device development regarding optical performance, stability of the material and the potential cost advantage of polymers and its processing techniques is still rarely seen.
A first focus lied on the development of an efficient fabrication method for polymer PLCs. The most attractive technique was found to be direct UV-printing of spin-coated polymer layers, where the processing time for waveguide structures is below one hour.
An important step towards a reliable fabrication of waveguides with good performance was the evaluation of different polymer materials. It turned out that fluorinated acrylates were best suited. The fluorination lowers the absorption at telecom wavelengths due to the excitation of vibrational overtones of C-H bonds. Additionally, it reduces the uptake of moistures in hot and humid atmospheres. Consequently, waveguides with a low propagation loss (0.4 dB/cm) and good environmental stability were produced.
First devices were designed and characterised for a comparison to the performance of PLCs based on other materials, e.g. silica waveguides. The insertion loss of passive power splitters almost reached the generally specified values. Estimations on an improvement of the insertion loss show that the desired specifications are within reach. However, it also must be stated that the propagation loss of the waveguides is still a limiting factor in the competition with silica waveguide.
An essential advantage of polymers is certainly the high thermo-optic coefficient that was measured with a grating coupling technique. Profiting from this material property low power thermo-optic switches were devised. The switches showed a low insertion loss, a satisfying extinction ratio with a power consumption of only 40mW. The switching speed of less than 2ms is sufficient for routing applications.
A critical part of the fabrication of integrated devices is the fiber pigtailing of the waveguide chip. With active fiber alignment and a subsequent fixation with UV curable adhesive a relatively low coupling loss was achieved. However, this procedure is quite time consuming and temperature cycles showed that it is difficult to achieve a constant coupling efficiency in changing environmental conditions. However, it was shown that the materials itself could withstand high temperatures also in combination with a high relative humidity. A more efficient passive alignment process was initialized, where the waveguide chip and the fibers are aligned on a common substrate and the fibers are aligned in V-grooves structures was initialized. This process could lead to an efficient pigtailing process that would complement the fast fabrication technique of the PLCs.

9.2. Outlook

There are mainly three issues on which further development should focus on:

- material development
- simple and precise alignment method for fiber pigtailing the waveguide chips
- efficient and reliable packaging

An essential improvement in the fabrication process of polymer PLCs is still possible with a further development on the material side. A further reduced optical loss would improve the performance of the waveguides. An even more critical point is the material property during the UV exposure for the structuring of the waveguides. If a material can be dried with a softbake, the polymer layer could be brought into contact with the mask without sticking. This would lead to better defined waveguide shapes and a much more reliable process. The reproducibility of the waveguide fabrication would also enable a more consequent optimization of designs and process parameters.
The fabrication of polymer PLCs has been brought to a relatively high level. But there is still much ahead for an efficient packaging of the obtained waveguide chips. The idea of using V-grooves as passive alignment

structures for the positioning of fibers makes long fine alignment procedures redundant. Consequently, a similar process should be used for the positioning of the waveguide chip on the common substrate. Well designed alignment structures could enable a precise assembly of chip and fibers without the need of expensive fine alignment stages or flip-chip machines with accuracies in the sub-micrometer region.

Finally, the pigtailed wafer should obtain a simple package. This package should improve the environmental and mechanical stability of the device. Today, expensive hermetic packages are standard. With an improved stability on the chip level simpler packages would be sufficient. A cheaper quasi-hermetic package would then also consistently complete the combination of a potential low cost material, an efficient fabrication of PLCs and a simple passive assembly process for fiber pigtailing the waveguide chip.

10. References

[1] H.P. Weber, W.J. Tomlinson, E.A. Chandross, "*Organic materials for integrated optics*", Optical Quantum Electronics, **7**, 465-473, 1975

[2] B.L. Booth, "*Low Loss Channel Waveguides in Polymers*", J. of Lightwave Technology, **7**, 1445-1453, 1989

[3] L. Eldada, "*Advances in telecom and datacom optical components*", Optical Engineering, **40**, 1165-1178, 2001

[4] M.J. Mahony, "*Semiconductor laser optical amplifiers for use in future fibersystems*", J. of Lightwave Technology, **6**, 531-544, 1988

[5] J.M. Wiesenfeld, B. Glance, J.S. Perino, A.H. Gnauck, „*Wavelength conversion at 10 Gb/s using a semiconductor optical amplifier*", IEEE Photonics Technolgy Letters, **5**, 1300-1303, 1993

[6] Y.C. Yan, A.J. Faber, H. de Waal, P.G. Kik, A. Polman, "*Erbium doped phosphate glass waveguide on silicon with 4.1dB/cm gain at 1..535μm*", Applied Physics Letters, **71**, 2922-2924, 1997

[7] A. Kaneko, T. Goh, H. Yamada, T. Tanaka, I. Ogawa, "*Design and applications of silica-based planar lightwave circuits*", IEEE J. of Selected Topics in Quantum Electronics, **5**, 1227-1236, 1999

[8] L.G. de Peralta, A.A. Bernussi, S. Frisbie, R. Gale, H. Temkin, "*Reflective arrayed waveguide grating multiplexer*", IEEE Photonincs Technology Letters, **15**, 1398-1400, 2003

[9] M.A. Mahdi, F.R.M. Adikan, P. Poopalan, S. Selvakennedy, H. Ahmad, "*High-gain bidirectional Er/sup 3+/-doped fiber amplifier for conventional- and long-wavelength bands*", IEEE Photonincs Technology Letters, **12**, 1468-1470, 2000

[10] M.J. Holmes, D.L. Williams, R.J. Manning, "*Highly Nonlinear Optical Fiber for All Optical Processing Applications*", IEEE Photonics Technology Letters, **7**,1045-1047, 1995

[11] V.R. Almelda, C.A. Barrios, R.R. Panepucci, M. Lipson, "*All-optical control of light on a silicon chip*", Nature, **43**, 1081-1084, 2004

[12] Haisheng Rong, Richard Jones, Ansheng Liu, Oded Cohen, Dani Hak, "*A continuous-wave Raman silicon laser*", Nature, **433**, 725-728, 2005

[13] G. T. Reed, "*The optical age of silicon*", Nature, **427**, 595-596, 2004

[14] T. Hashimoto, Y. Nakasuga, Y. Yamada, H. Terui, M. Yanagisawa, Y. Akahori, Y. Tohmori, K. Kato, Y. Suzuki, "*Multichip optical hybrid integration technique with planar lightwave circuit platform*", **16**, 1249-1258, 1998

[15] Atsushi Sakai, Go Hara and Toshihiko Baba, "*Propagation Characteristics of Ultrahigh-Δ Optical Waveguide on Silicon-on-Insulator Substrate*", Japanese J. of Applied Physics, **40**, L383-L385, 2001

[16] X. Duan, Y. Huang, Y. Cui, J. Wang, C.M. Lieber, "Indium phosphide nanowires as building blocks for nanoscale electronic and optoelectronic devices", Nature, **409**, 66-69, 2001

[17] I. Märki, M. Salt, H.P. Herzig, „*Practical and theoretical modal analysis of photonic crystal waveguides*", J. of Applied Physics, **96**, 7-11, 2004

[18] L. Eldada, L.W. Shacklette, "*Advances in Polymer Integrated Optics*", IEEE J. of Selected Topics in Quantum Electronics, **6**, 54-68, 2000

[19] H. Ma, A.K.-Y. Jen, L.R. Dalton, „*Polymer-Based Optical Waveguides: Materials, Processing, and Devices*", Advanced Materials, **14**, 1339-1365, 2002

[20] L. Shacklette, R. Blomquist, J.M. Deng, P.M. Ferm, M.R. Maxfield, J. Mato, H. Zou, "*Ultra-Low-Loss Acrylate Polymers for Planar Light Circuits*", Advanced Functional Materials, **13**, 453-462, 2003

[21] A. Yeniay, R. Gao, K. Takayama, R. Gao, F. Garito, "*Ultra-Low-Loss Polymer Waveguides*", J. of Lightwave Technology, **22**, 154-158, 2004

[22] L. Eldada, "Polymer integrated optics: promise vs. practicality", Proceedings SPIE, 2002

[23] S. Park, J.J. Ju, J.Y. Do, S.K. Park, J.T. Ahn, S.-I. Kim, M.-H. Lee, "*16-Arrayed Electrooptic Polymer Modulator*", IEEE Photonics Technology Letters, **16**, 1834-1836, 2004

[24] Y.K. Olsson, G. Chen, R. Rapaport, D.T. Fuchs, V.C. Sundar, J.S. Steckel, M.G. Bawendi, A. Aharoni, U. Banin, "*Fabrication and optical properties of polymeric waveguides containing nanocrystalline quantum dots*", Applied Physics Letters, **85**, 4469-4471, 2004

[25] B.G. Yacobi, S. Martin, K. Davis, A. Hudson, and M. Hubert, "*Adhesive bonding in microelectronics and photonics*", J. of Applied Physics, **91**, 6227-6262, 2002

[26] C.K. Madsen, J.H. Zhao, „*Optical filter design and analysis: A signal processing approach*", John Wiley & Sons Inc., 1999

[27] E.A. Marcatili, „*Dielectric Rectangular Waveguide and Directional Coupler for Integrated Optics*“, Bell System Technical J., **48**, 2071-2102, 1969
[28] G.B. Hocker, W.K. Burns, “*Mode Dispersion in Diffused Channel Waveguides by the Effective Index Method*”, Applied Optics, **16**, 113-118, 1977
[29] E.C.M. Pennings, J. Van Schoonhoven, J.W.M. Van Uffelen, M.K. Smit, “*Reduced Bending and Scattering Losses in New Optical ‘Double-Ridge’ Waveguide*”, Electronics Letters, **25**, 746-748, 1989
[30] S. Suzuki, M. Yanagisawa, Y. Hibino, K. Oda, “*High-Density Integrated Planar Lightwave Circuits Using SiO2-GeO2 Waveguides with a High Refractive Index Difference*”, J. of Lightwave Technology, **12**, 790-796, 1994
[31] D. Marcuse, “*Bending Losses of the Asymmetric Slab Waveguide*”, Bell System Technical. J., **50**, 1551-1563, 1971
[32] W. Berglund, A. Gopinath, “*WKB Analysis of Bend Losses in Optical Waveguides*”, J. of Lightwave Technology, **18**, 1161-1166, 2000
[33] M. Heiblum, J.H. Harris, “*Analysis of curved optical waveguides by conformal transformation*”, IEEE J. Quantum Electronics, **QE-11**, 75-83, 1975
[34] V. Van, P.P. Absil, J.V. Hryniewicz, P.-T. Ho, “*Propagation Loss in Single-Mode GaAs-AlGaAs Microring Resonators: Measurement and Model*”, J. of Lightwave Technology, **19**, 1734-1739,2001
[35] M. Saruwatari, K. Nawata, “*Semiconductor laser to single-mode fiber coupler*”, Applied Optics, **18**, 1847-1856, 1979
[36] S.-L. Chuang, “*A Coupled Mode Formulation by Reciprocity and a Variational Principle*”, J. of Lightwave Technology, **LT-5**, 5-15, 1987
[37] A. Hardy, W. Streifer, “*Coupled mode solutions of multiwaveguide systems*”, IEEE J. of Quantum Electronics, **LT-4**, 90-99, 1986
[38] H.A. Haus, W.P. Huang, S. Kawakami, N.A. Whitaker, „*Coupled-mode theroy of optical waveguides*“, J. Lightwave Technology, **LT-5**, 16-23, 1987
[39] K. Kawano, T. Kitoh, “*Introduction to Optical Waveguide Analysis*”, John Wiley & Sons, Inc., 2001
[40] Manual of Femlab, www.femlab.de
[41] G.R. Hadley, “*Wide-angle beam propagation using Padé approximant operators*”, Optics Letters, **17**, 1426-1428, 1992

[42] K.S. Yee, “*Numerical solution of initial boundary value problems involving Maxwell’s equations in isotropic media*”, IEEE Transactions on Antenna Propagation, **AP-14**, 302-307, 1966
[43] R.A. Norwood, “*Optical polymers: Critical requirements for optical access applications*”, Proceedings of SPIE, Denver, **5517**, 124-133, 2004
[44] Hong Ma, Alex K.-Y. Jen and Larry R. Dalton, „*Polymer-based optical waveguides: Materials, Processing and Devices*“, Advanced Materials, **14**, 1339-1365, 2002
[45] M. Diemeer, P. De Dobbelaere, R. Flipse, „*Polymeric Thermo-Optic Digital Optical Switches*”, in Integrated Circuits and Components, E.J. Murhpy (Editor), Marcel Dekker Inc., 1999
[46] J. Brandrup, E.H. Immergut, E.A. Grulke, „*Polymer Handbook*“, John Wiley & Sons, 1999
[47] T. Tamir, S.T. Pent, „*Analysis and Design of Grating Couplers*“, Applied Physics, Vol. 14, 235-254, 1977
[48] Telcordia Technologies, “*Generic Requirements for Passive Optical Components (GR-1209-CORE)*”, 2001
[49] E.C. M. Pennings, R.J. Deri, A. Scherer, R. Bhat, T.R. Hayes, N.C. Andreadakis, M.K. Smit, L.B. Soldano, R.J. Hawkins, “*Ultracompact, low-loss directional couplers on InP based on self-imaging by multimode interference*”, Applied Physics Letters, **59**, 1926-1928, 1991
[50] Y.-O. Noh, J.-M. Kim, M.-S. Yang, H.-J. Choi, H.-J. Lee, Y.-H. Won, S.-G. Han, “*Thermooptic 2x2 Asymmetric Digital Optical Switches With Zero-Voltage Operation State*”, IEEE Photonics Technology Letters, **16**, 446-448, 2004
[51] K.-H. Kim, M.-S. Kwon, S.-Y. Shin, D.-S. Choi, „*Vertical Digital Thermooptic Switch in Polymer*“, IEEE Photonics Technology Letters, **16**, 783-785, 2004
[52] T. Kowalczyk, R. Blum, “*Polymer Variable Optical Attenuator Arrays: Pathway from Material Platform to Qualified Telecom Product*”, Proceedings of SPIE, Denver, **5517**, 50-61, 2004
[53] S.M. Garner, S. Caracci, “*Variable Optical Attenuator for Large-Scale Integration*”, IEEE Photonics Technology Letters, **14**, 1560-1563, 2002
[54] S.-S. Lee, Y.-S. Jin, Y.-S. Son, „*Variable Optical Attenuator Based on a Cutoff Modulator with Tapered Waveguides in Polymers*“, J. of Lightwave Technology, **17**, 2556-2561, 1999

[55] G. Aeppli, "*Fiber pigtailing and packaging of integrated polymer devices*", Diploma thesis, Swiss federal institute of Technology (ETH), Zürich, 2004
[56] M. Schadt, K. Schmitt, V. Kozinkov, V. Chigrinov, „*Surface-induced parallel alignment of liquid crystals by linearly polymerized photopolymers*", Jpn. J. Applied Physics, **31,** 2155-2164, 1992
[57] M. Schadt, "*Liquid crystal materials and liquid crystal displays*", in Annual Revision of Material Sciences, E.N. Kaufmann, ed., Ch. J. Summers, guest. ed., 305-375,1997
[58] The polymers have been developed and are distributed by Rolic Technologies Ltd. (Allschwil, Switzerland).
[59] J. A. Dobrowolski, "*Optical Properties of Films and Coatings*", in Handbook of Optics, Volume 1, Michael Bass (editor), McGraw-Hill, New York, 42.3, 1995
[60] M. Born, E. Wolf, *Principles of Optics* (Cambridge University Press), 1999
[61] V. Van, P.P. Absil, J.V. Hryniewicz, P.-T. Ho, "*Propagation Loss in Single-Mode GaAs-AlGaAs Microring Resonators: Measurement and Model*", J. Lightwave Technology, **19**, 1734-1739, 2001
[62] F. Horst, R. Germann, U. Bapst, D. Wiesmann, B.J. Offrein, G.L. Bona, „*Compact tunable FIR dispersion compensator in SiON technology*", IEEE Photonics technology letters, **15**, 1570-1572, 2003
[63] R. Grover, V. Van, T.A. Ibrahim, P.P. Absil, L.C. Calhoun, F.G. Johnson, J.V. Hrynievicz, P.-T. Ho, "*Parallel-Cascaded Semiconductor Mircroring Resonators for High-Order and Wide-FSR Fileters*" J. of Lightwave Technology, **20**, 900-905, 2002
[64] B.E. Little, S.T. Chu, H.A. Haus, J. Foresi, J.-P. Laine, "*Mircroring Resonator Channel Dropping Filters*", J. of Lightwave Technology, **15**, 998-1005, 1997.
[65] S. Suzuki, Y. Hatakeyama, Y. Kokubun, S.-T. Chu, "*Precise control of wavelength channel spacing of microring resonator add-drop filter array*" J. of Lightwave Technology, **20**, 745-750, 2002
[66] V. Van, T.A. Ibrahim, P.P. Absil, F.G. Johnson, R. Grover, P.-T. Ho, "*Optical Signal Processing Using Nonlinear Semiconductor Microring Resonators*", IEEE J. of Selected Topics in Quantum Electronics, **8**, 705-713, 2002
[67] W.E. Svendsen, H.T. Philipp, M. Svalgaard, H. Mertens, K.N. Andersen, „*High Index Ring Resonator Coupled to UV-Written Waveguide*", Proceedings of ECOC-2002, Volume 2, paper 4.2.4, 2002

[68] P.P. Absil, J.V. Hryniewicz, B.E. Little, F.G. Johnson, K.J. Ritter, P.-T. Cho, "*Vertically Coupled Microring Resonators Using Polymer Wafer Bonding*", IEEE Photonics Technology Letters, **13**, 49-51, 2001.
[69] D. Klunder, "*Photon Physics in Integrated Optics Microresonators*", PhD Thesis, University Twente, Netherlands, 2002
[70] D.J.W. Klunder, F.S. Tan, T. van der Veen, H.F. Bulthuis, G. Sengo, B. Docter, H.J.W.M. Hoekstra, A. Driessen, "*Experimental and Numerical Study of SiON Microresonators with Air and Polymer Cladding*", J. of Lightwave Technology, **21**, 1099-1110, 2003

List of abbreviations and variables

APSS	Apollo Photonics solution suite (software tool)
BPM	beam propagation method
CE	coupling efficiency
DOS	digital optical switch
FDTD	finite difference time domain
FEM	finite element method
IL	insertion loss
LPP	linear photo-polymerizable
MMI	multimode interferometer
MZI	Mach-Zehnder interferometer
PLC	planar lightwave circuit
PON	passive optical network
RF	radio frequency
RH	relative humidity
RIE	reactive ion etching
TE	transverse electric (polarization)
TEM	transverse electro-magnetic (polarization)
TM	transverse magnetic (polarization)
TO	thermo-optic
VOA	variable optical attenuator
WDM	wavelength division multiplexing

β	propagation constant
λ	wavelength / thermal conductivity in chapter 4.3.2
n_{cl}	refractive index of waveguide cladding
n_{co}	refractive index of waveguide core
n_{eff}	effective index of waveguide mode
T_g	glass transition temperature

Publications and Conference contributions

Publications

- A. Stump, J. Kunde, U. Gubler, A.C. Pliska-Leduff, C. Bosshard, „A study on a microring structure for practical devices“, Optical and Quantum Electronics, Vol. 35, 1205-1213, 2003
- A. Stump, U. Gubler, C. Bosshard, “Optical Waveguides Structured with Photo-Aligning Polymers”, Optics Letters, Vol. 30, 1333-1335, 2005

Conference contributions

- A. Stump, J. Kunde, U. Gubler, A.-C. Pliska-Leduff, C. Bosshard, „A microring structure for practical devices”, Optical Waveguide Theory and Numerical Modelling (OWTNM), Prague, 2003
- A. Stump, U. Gubler, C. Bosshard, “Polymer Optical Waveguides Structured by UV-exposure”, EOS Topical meeting: Optics in Computing, Engelberg, 2004
- A. Stump, U. Gubler, C. Bosshard, “Polymer optical waveguides: from the design to the fiber-pigtailed device”, Annual meeting of Polymer Gruppe der Schweiz (PGS), Zürich, 2004
- A. Stump, U. Gubler, C. Bosshard, “Photo-aligning polymers for a fast waveguide fabrication”, European Conference on Integrated Optics (ECIO), Grenoble, 2005

Acknowledgements

I would like to thank everybody who supported me during this work. I always felt like being at a good place for doing my PhD thesis. Not only the scientific support, but also discussions and the good sense of humour of the whole team in Alpnach have always essentially contributed to my motivation.
Special thanks I want to express to Ulrich Gubler who has initially launched this project. The close collaboration did not only assure good progress in this work but has also always been a great pleasure. Then I would like to thank Christian Bosshard for giving me the opportunity to do my PhD thesis in his group and supporting me as PhD student. I always enjoyed working in Christians “Optics”-group together with Jens Kunde, Anne-Claire Pliska and Sylvain Grossmann. A special thank also to Jens Kunde for the supervision in my first months of this thesis in the micro-ring project (and also for the long bike tours in Obwalden).

This thesis would also not have been possible without the collaboration with the University of Neuchâtel. I would like to thank Hans-Peter Herzig for being supervisor of my thesis. I always appreciated the informal and stimulating discussions. Finally I want to thank René Dändliker, Georg Guekos and Daniel Erni for being part of the committee.

Curriculum vitae

name	Andrin Stump
born	June 26, 1976 in Teufen (Switzerland)
1991-1995	Kantonsschule in Trogen (Type B)
1996-2001	Studies in Physics at Swiss Federal Institute of Technology (ETH) in Zürich
1999-2000	Studies in Physics at University “Claude Bernard” in Lyon (France)
March 2001	Graduation with diploma in experimental physics at ETH
2001-2002	Ph.D. student in the group of Professor Heinz Jäckel at the Institute for Electronics (ETH) working on all optical switches
2002-2005	Ph.D. student at CSEM Alpnach in the group of Dr. Christian Bosshard in collaboration with Professor Hans-Peter Herzig from the University of Neuchâtel working on the here presented thesis